ADSORPTION-PHOTOCATALYTIC DEGRADATION OF CHICKEN PROCESSING WASTEWATER USING POWDERED ACTIVATED CARBON-SUPPORTED GRAPHITIC CARBON NITRIDE

LEONG KEN LAP

A project report submitted in partial fulfilment of the requirements for the award of Bachelor of Engineering (Honours) Chemical Engineering

Lee Kong Chian Faculty of Engineering and Science
Universiti Tunku Abdul Rahman

April 2020

DECLARATION

I hereby declare that this project report is based on my original work except for citations and quotations which have been duly acknowledged. I also declare that it has not been previously and concurrently submitted for any other degree or award at UTAR or other institutions.

Signature : leong

Name : LEONG KEN LAP

ID No. : 1601488

Date : 21 APRIL 2020

APPROVAL FOR SUBMISSION

I certify that this project report entitled **"ADSORPTION-PHOTOCATALYTIC DEGRADATION OF CHICKEN PROCESSING WASTEWATER USING POWDERED ACTIVATED CARBON-SUPPORTED GRAPHITIC CARBON NITRIDE"** was prepared by **LEONG KEN LAP** has met the required standard for submission in partial fulfilment of the requirements for the award of Bachelor of Engineering (Honours) Chemical Engineering at Universiti Tunku Abdul Rahman.

Approved by,

Signature : Sim.

Supervisor : DR. SIM LAN CHING

Date : 24 April 2020

ACKNOWLEDGEMENTS

I would like to show my appreciation to everyone who had contributed and supported in the succeed completion of this entire project. Foremost, I would like to express my sincere gratitude to my research supervisor, Dr. Sim Lan Ching for her invaluable advice, guidance and her enormous patience throughout the development of the research. Her guidance and suggestion helped me in all the time of research and thesis preparation.

In addition, I would also like to thank my loving parents and fellow friends for helping me survive all the stress throughout this project. To my best buddy, Sew Yen Hau, I would like to show my grateful for always listening and giving me words of encouragement which pushing me farther than I could ever go.

Finally, I would like to give special thanks to the post-graduate student, Chai Yi Ding, for sharing her invaluable knowledge and opinion in this study. Thanks a ton to all people who helping me in accomplishment of this final year project.

ABSTRACT

Due to the expansion of agricultural sector, a massive volume of chicken processing wastewater has been produced and the conventional technologies are ineffective to remove organic and inorganic compounds. Thus, this project will solely investigate the performance for the adsorption-photocatalytic degradation of chicken processing wastewater using powdered activated carbon (PAC) supported graphitic carbon nitride (g-C_3N_4). Different weight percentage of g-C_3N_4 (20 wt%, 40 wt% and 60 wt%) were successfully supported onto the AC surface. 20 wt% g-C_3N_4/PAC composite, 40 wt% g-C_3N_4/PAC composite and 60 wt% g-C_3N_4/PAC composite were prepared. The synthesized catalysts were characterized using Brunauer-Emmett-Teller (BET), Fourier Transform Infrared (FTIR), X-Ray Diffraction (XRD), Scanning Electron Microscope (SEM) and Electron Dispersive X-ray (EDX). Through BET analysis, the specific surface area of 20 wt% g-C_3N_4/PAC composite, 40 wt% g-C_3N_4/PAC composite and 60 wt% g-C_3N_4/PAC composite were larger than that of pure g-C_3N_4 and this was attributed to the presence of AC that provided a larger surface area. The nitrogen element was identified in g-C_3N_4/PAC composites by EDX and the FTIR spectra show that the g-C_3N_4/PAC composites had the characteristic functional group of g-C_3N_4 which are aromatic C-N and C=N bonds. It was noticeable that the incorporation of AC did not improve the performance in orthophosphate and ammonia nitrogen removal in the dark adsorption. Overall, AC achieved the highest COD removal efficiency (79.00 %) in the dark adsorption. Meanwhile, the pure g-C_3N_4 achieved the highest orthophosphate (49.10 %) and ammonia nitrogen removal efficiency (100 %) in the dark adsorption. 20 wt% g-C_3N_4/PAC composite showed the highest COD removal efficiency (47.00 %) by photodegradation under the irradiation of LED light. The pure g-C_3N_4 showed the highest orthophosphate (49.00 %) removal efficiency by photodegradation under the irradiation of LED light; whereas, the 60 wt% g-C_3N_4/PAC composite showed the highest ammonia nitrogen removal efficiency (52.90 %) by photodegradation under the irradiation of LED light.

TABLE OF CONTENTS

DECLARATION **i**

APPROVAL FOR SUBMISSION **ii**

ACKNOWLEDGEMENTS **iv**

ABSTRACT **v**

TABLE OF CONTENTS **vi**

LIST OF TABLES **ix**

LIST OF FIGURES **x**

LIST OF SYMBOLS / ABBREVIATIONS **xiv**

LIST OF APPENDICES **xvi**

CHAPTER

1 INTRODUCTION **1**
- 1.1 Background 1
- 1.2 Problem Statement 2
- 1.3 Aim and Objective 4
- 1.4 Scope of Study 4

2 LITERATURE REVIEW **5**
- 2.1 Chicken Processing Wastewater 5
  - 2.1.1 Chicken Processing Wastewater Treatment Process 23
- 2.2 Adsorption 10
- 2.3 Heterogeneous Photocatalysis 11
  - 2.3.1 Mechanism of Heterogeneous Photocatalysis 28
  - 2.3.2 Benefits and Drawbacks of Heterogeneous Photocatalysis 31
- 2.4 Activated Carbon (AC) 16
  - 2.4.1 Application of AC 17
  - 2.4.2 Mechanism of AC in Degradation of

Pollutant 34
2.4.3 Benefits and Drawbacks of AC 19
2.5 Graphitic Carbon Nitride (g-C_3N_4) 20
2.5.1 Synthesis Method of g-C_3N_4 21
2.5.2 Application of g-C_3N_4 26
2.5.3 Benefits and Drawbacks of g-C_3N_4 26
2.6 Photocatalytic Application of Photocatalyst Supported on AC 43
3 METHODOLOGY 33
3.1 Experimental Flow Chart 33
3.2 Materials and Chemicals 34
3.3 Synthesis of Pure g-C_3N_4 34
3.4 Preparation of g-C_3N_4/PAC Composites 35
3.5 Characterization of g-C_3N_4/PAC Composites 35
3.6 Adsorption-Photocatalytic Degradation of the Chicken Processing Wastewater 52
3.7 Separation of Catalyst 37
3.8 Chemical Oxygen Demand (COD) Test 38
3.9 Orthophosphate Test 39
3.10 Ammonia Nitrogen Test 39
4 RESULTS AND DISCUSSION 41
4.1 Brunauer-Emmett-Teller (BET) Analysis 41
4.2 Fourier Transform Infrared (FTIR) Spectroscopy 44
4.3 X-ray Diffraction (XRD) 47
4.4 Scanning Electron Microscopy (SEM) 48
4.5 Energy Dispersive X-ray (EDX) 50
4.6 Adsorption-Photocatalytic Degradation of Chicken Processing Wastewater 67
4.6.1 COD Removal 55
4.6.2 Orthophosphate Removal 57
4.6.3 Ammonia Nitrogen Removal 60
5 CONCLUSIONS AND RECOMMENDATIONS 63
5.1 Conclusions 63
5.2 Recommendations for future work 64

REFERENCES **65**
APPENDICES **79**

LIST OF TABLES

Table 2.1: Design Effluent Values. 6

Table 2.2: Drawbacks of Conventional Technologies. 8

Table 2.3: Different Types of AOPs in COD Removal of Wastewater. 9

Table 2.4: Advantages and Disadvantages of Heterogeneous Photocatalysis. 16

Table 2.5: Advantages and Disadvantages of AC 20

Table 2.6: Characteristics of g-C_3N_4 Synthesized by Thermal Condensation. 23

Table 2.7: Advantages and Disadvantages of g-C_3N_4. 26

Table 2.8: Removal Efficiency of Organic Pollutant by Different Photocatalysts. 29

Table 4.1: BET Specific Surface Area (S_{BET}), Pore Volume (V_{tot}) and Pore Size (D_{pore}) of the Synthesized Catalyst. 42

Table 4.2: Elemental Composition of the Synthesized Catalysts. 51

Table 4.3: Performance of various catalyst in chicken processing wastewater treatment. 52

LIST OF FIGURES

Figure 2.1: Chicken Processing Wastewater Treatment Process. 8

Figure 2.2: Schematic Diagram of Adsorption and Desorption Process. 10

Figure 2.3: (A) Chemical Adsorption and (B) Physical Adsorption. 11

Figure 2.4: Scheme of a Photocatalytic Process. 14

Figure 2.5: Adsorption Mechanisms on Adsorbent Surface. 18

Figure 2.6: Energy Band Gaps of Different Semiconductors 21

Figure 2.7: Synthesis Process of g-C_3N_4 by Thermal Condensation of Different Precursors such as Melamine, Cyanamide, Dicyandiamide, Urea and Thiourea. 22

Figure 2.8: Proposed Mechanism of Adsorption and Decomposition of Bisphenol A. on Modified Photocatalysts. 28

Figure 3.1: Methodology Flow of the Project. 33

Figure 3.2: Synthesis Method of Pure g-C_3N_4. 34

Figure 3.3: Adsorption-Photocatalytic Degradation of Chicken Processing Wastewater. 37

Figure 3.4: Separation of Catalyst by Centrifuge. 37

Figure 3.5: COD Test of Chicken Processing Wastewater. 38

Figure 3.6: Orthophosphate Test of Chicken Processing Wastewater. 39

Figure 3.7: Ammonia Nitrogen Test of Chicken Processing Wastewater. 40

Figure 4.1: N_2 Adsorption-Desorption Isotherms for AC and g-C_3N_4/PAC Composites. 43

Figure 4.2: N_2 Adsorption-Desorption Isotherms for pure g-C_3N_4. 43

Figure 4.3: FTIR spectra of AC, pure g-C_3N_4 and g-C_3N_4/PAC Composites. 45

Figure 4.4: FTIR spectra of Spent AC, Spent g-C_3N_4 and Spent g-C_3N_4/PAC Composites. 46

Figure 4.5: XRD Pattern of AC, Pure g-C_3N_4 and g-C_3N_4/PAC Composites. 48

Figure 4.6: SEM Image of (a) Pure g-C_3N_4 (500X) (b) Pure g-C_3N_4 (2000X) (c) Pure g-C_3N_4 (10000X) (d) AC (2000X) (e) AC (8000X) (f) AC (30000X) (g) 20 wt% g-C_3N_4/PAC (2000X) (h) 20 wt% g-C_3N_4/PAC (6500X) (i) 20 wt% g-C_3N_4/PAC (8000X) (j) 40 wt% g-C_3N_4/PAC (2000X) (k) 40 wt% g-C_3N_4/PAC (6500X) (l) 40 wt% g-C_3N_4/PAC (8000X) (m) 60 wt% g-C_3N_4/PAC (2000X) (n) 60 wt% g-C_3N_4/PAC (6500X) (o) 60 wt% g-C_3N_4/PAC (8000X) 50

Figure 4.7: COD Removal in the Dark Adsorption. 56

Figure 4.8: COD Removal by Photocatalytic Degradation Under Irradiation of LED Light. 56

Figure 4.9: Comparison Chart of COD Removal Efficiency by Adsorption and Photocatalytic Degradation. 57

Figure 4.10: Orthophosphate Removal in the Dark Adsorption. 59

Figure 4.11: Orthophosphate Removal by Photocatalytic Degradation Under Irradiation of LED Light. 59

Figure 4.12: Comparison Chart of Orthophosphate Removal Efficiency by Adsorption and Photocatalytic Degradation. 60

Figure 4.13: Ammonia Nitrogen Removal in the Dark Adsorption. 61

Figure 4.14: Ammonia Nitrogen Removal by Photocatalytic Degradation Under Irradiation of LED Light. 62

Figure 4.15: Comparison Chart of Ammonia Nitrogen Removal Efficiency by Adsorption and Photocatalytic Degradation. 62

Figure A-1: BET Summary Report of Pure g-C_3N_4. 79

Figure A-2: N_2 Adsorption Isotherm of Pure g-C_3N_4. 80

Figure A-3: BET Summary Report of AC. 81

Figure A-4: N_2 Adsorption Isotherm of AC. 82

Figure A-5: BET Summary Report of 20 wt% g-C_3N_4/PAC Composite. 83

Figure A-6: N_2 Adsorption Isotherm of 20 wt% g-C_3N_4/PAC Composite. 84

Figure A-7: BET Summary Report of 40 wt% g-C_3N_4/PAC Composite. 85

Figure A-8: N_2 Adsorption Isotherm of 40 wt% g-C_3N_4/PAC Composite. 86

Figure A-9: BET Summary Report of 60 wt% g-C_3N_4/PAC Composite. 87

Figure A-10: N_2 Adsorption Isotherm of 60 wt% g-C_3N_4/PAC Composite. 88

Figure B-1: FTIR Spectrum of Pure g-C_3N_4. 89

Figure B-2: FTIR Spectrum of AC. 90

Figure B-3: FTIR Spectrum of 20 wt% g-C_3N_4/PAC Composite. 91

Figure B-4: FTIR Spectrum of 40 wt% g-C_3N_4/PAC Composite. 92

Figure B-5: FTIR Spectrum of 60 wt% g-C_3N_4/PAC Composite. 93

Figure B-6: FTIR Spectrum of Spent g-C_3N_4. 94

Figure B-7: FTIR Spectrum of Spent AC. 95

Figure B-8: FTIR Spectrum of Spent 20 wt% g-C_3N_4/PAC Composite. 96

Figure B-9: FTIR Spectrum of Spent 40 wt% g-C_3N_4/PAC Composite. 97

Figure B-10: FTIR Spectrum of Spent 60 wt% g-C_3N_4/PAC Composite. 98

Figure C-1: EDX Analysis of Pure g-C_3N_4. 99

Figure C-2: EDX Analysis of AC. 99

Figure C-3: EDX Analysis of 20 wt% g-C_3N_4/PAC Composite. 100

Figure C-4: EDX Analysis of 40 wt% g-C_3N_4/PAC Composite. 100

Figure C-5: EDX Analysis of 60 wt% g-C_3N_4/PAC Composite. 101

LIST OF SYMBOLS / ABBREVIATIONS

$^\bullet O_2^-$	superoxide radical
$^\bullet OH$	hydroxyl radical
AC	activated carbon
Ag	silver
AgCl	silver chloride
AOPs	advanced oxidation processes
$BaTiO_3$	barium titanate
BET	Brunauer-Emmett-Teller
BOD	biochemical oxygen demand
C	final concentration
C_0	initial concentration
CB	conduction band
CFCs	chlorofluorocarbons
CO_2	carbon dioxide
COD	chemical oxygen demand
CVD	chemical vapour deposition
DAF	dissolved air flotation
e^-	electron hole
E_{bg}	energy band gap
EDX	Energy Dispersive X-ray Analysis
Er^{3+}	erbium ion
eV	electron voltage
Fe_2O_3	iron (III) oxide
Fe_3O_4	ferroso ferric oxide
FTIR	Fourier-Transform Infrared Spectroscopy
$g\text{-}C_3N_4$	graphitic carbon nitride
h	hours
h^+	hole
H_2O	water
IR	infrared ray
LED	light-emitting diode
min	minutes

N_2	nitrogen
^oC	degree Celsius
OH^-	hydroxide ion
PAC	powder activated carbon
PVD	physical vapour deposition
$R^\bullet$	carboxyl radical
SEM	Scanning Electron Microscope
SnO_2	tin (IV) oxide
SrO_2	strontium peroxide
TFS	total fixed solid
TiO_2	titanium oxide
TS	total solid
TSS	total suspended solid
TVS	total volatile solid
UV	ultraviolet
VB	valence band
VOC	volatile organic chloride
WO_3	tungsten (VI) oxide
XRD	X-ray Diffraction
ZnO	zinc oxide
ZrO_2	zirconium dioxide

LIST OF APPENDICES

APPENDIX A: BET Report 79

APPENDIX B: FTIR Report 89

APPENDIX C: EDX Report 99

CHAPTER 1

INTRODUCTION

1.1 Background

According to The Department of Health (2010), water is one of the indispensable resources for every living creature in the earth. In short, all the living things cease to survive without water. Thus, it could be disastrous if the water is being polluted.

However, a massive volume of wastewater has been produced due to the expansion of agricultural sector and industrialization and poultry industry is one of the emerging divisions of the agricultural sector. The increasing demand of chicken for human consumption contributes to the rapid growth of poultry industry. The characteristics of wastewater that discharged from poultry farms include of high biological oxygen demand (BOD), high total solids content (TS) and complex mixture of fats, proteins and fibres, together with feathers, bedding and blood (Rajakumar et al., 2011).

Discharge of untreated or unwell treated chicken processing wastewater from chicken slaughterhouse to sewer will cause the contamination of both groundwater and surface water. Moreover, the chicken processing wastewater is rich in nitrogen and it can be converted to nitrate easily which might induce the occurrence of algae bloom and threaten aquatic life (Rajasulochana and Preethy, 2016). Water is also unsafe to drink if there is a high level of nitrate content as it will cause methemoglobionemia (blue baby syndrome) and can be fatal. Hence, the effect of chicken processing wastewater that brings to human must not be neglected.

In order to operate a poultry industry in the compliance with environmental regulations and acts, the chicken processing wastewater is often well treated using conventional technologies before it is disposed off. For instance, conventional techniques include of physical, biological and chemical treatment processes. Physical treatment involves the screening of feathers using filtration method to remove BOD_5 (Young, 2014; Imam, 1984).

Meanwhile, chicken processing wastewater can be managed via chemical treatment such as dissolved air flotation (DAF) and flocculation.

Biological treatment such as trickling filter is also one of the most common wastewater treatment processes in Malaysia while the chicken processing wastewater is treated by microorganisms in a controlled environment. These microorganisms can convert the biodegradable particles and some of the inorganic substances into other by-products. These by-products are then settled and removed in the clarifiers. The high rate biotreatment systems such as activated sludge tank are able to remove about 85 % of the BOD_5 and suspended solids that have been settled down in the primary settling tank (Jover-Smet, Martin-Pascual and Trapote, 2017). However, these conventional technologies are not effective to remove refractory pollutants.

Thus, heterogeneous photocatalysis has been prolonged in order to remove the gas phase or aqueous phase of organic and inorganic species. Photocatalysis is a redox reaction that driven by light and it often requires solid state catalysts. Researchers held that, the photochemistry based energy conversion process will take over the current fossil energy based conversion as it is more environmental friendly and cost effectively.

Basically, photocatalysts will absorb the ultraviolet (UV) ray or visible light and self-create a positive-hole. In the mean time, the electrons will be generated. Besides, the redox reaction between the positive holes and electron holes will lead to the formation of hydroxyl radicals and superoxide ions. Afterwards, the hydroxyl radicals and superoxide ions behave like strong oxidants which can further decompose the organic pollutants though photocatalytic reaction (Bensebaa, 2012).

1.2 Problem Statement

Chicken is one of the primary sources of meat protein and so, the slaughterhouses are expanded rapidly in Malaysia due to the increasing demand of chickens for consumption. Poultry farms are usually generate substantial amount of chicken processing wastewater regardless of the scale and size of the poultry farm. Hence, conventional wastewater treatment technologies are developed in order to treat the chicken processing wastewater before it is being discharged.

These conventional technologies used to treat chicken processing wastewater included physical, chemical and biological treatment process. However, conventional treatment for chicken processing wastewater is not very effective as some of the biological resistant organic compounds do not induce oxygen depletion in receiving water. Conventional treatment is also found to be inconvenient as it requires a large operational area and extra chemical processes to remove the undesired sludge produced (Brandao, de Oliveira and Benachour, 2016). In order to completely degrade the highly refractory chicken processing wastewater, scientists have implemented the advanced oxidation processes (AOPs).

The n-type semiconductors such as titanium dioxide (TiO_2), strontium peroxide (SrO_2), tungsten trioxide (WO_3) and tin (IV) oxide (SnO_2) can be employed in photocatalytic oxidation processes. Chicken processing wastewater can be photodegraded by employing these catalysts under irradiation of a light source and electron-hole pairs will be created which allow the contaminants to be oxidized by $OH^\bullet$ (hydroxide radical) generated. Commonly, AOPs become an effective method of chicken processing wastewater treatment due to its strong oxidizing power, no secondary pollution will be generated and mild reaction conditions (Kanakaraju, Glass and Oelgemoller, 2014). However, there are some drawbacks for photocatalysts such as high calcinations temperature required and the extremely high energy band gap only can be overcome by the strong UV light (Sakka, 2013).

Therefore, the shortages of the heterogeneous photocatalysis raise the concern on the performance of adsorption-photocatalytic degradation of the chicken processing wastewater using activated carbon-supported graphitic carbon nitride. By using $g\text{-}C_3N_4/PAC$ composites to degrade chicken processing wastewater, AC provides a larger specific surface area to $g\text{-}C_3N_4$ which improves the adsorption capacity of the synthesized catalysts. The contaminants will initially adsorb onto the surface of the composites, follows by photodegradation under the irradiation of a source of light (Laysandra, et al., 2017). The main advantage of this mechanism (adsorption plus photocatalysis) is that PAC can provide a larger immobilize surface area for g-C_3N_4 which increases the efficiency of degradation of the chicken processing wastewater.

1.3 Aim and Objective

This entire project is aimed to examine the overall performance and effectiveness of the synthesized photocatalysts on the degradation of chicken processing wastewater under irradiation of LED light. To facilitate the main purpose of this study, the main objectives are distinguished and summarized as following:

(i) To prepare the PAC and g-C_3N_4 composites using wet impregnation method.
(ii) To examine the physicochemical properties of the synthesized photocatalyst using BET, FTIR, XRD, SEM and EDX analysis.
(iii) To evaluate adsorption-photocatalytic performance for the degradation of the chicken processing wastewater under LED light irradiation.

1.4 Scope of Study

Through this project, g-C_3N_4 composite will be prepared using pyrolysis of urea powder. In order to discover a better adsorption-photocatalytic performance on the degradation of the chicken processing wastewater, the weight percentage of g-C_3N_4 (20 wt%, 40 wt% and 60 wt%) will be varied incorporated with PAC.

Moreover, this project is mainly to examine the method of synthesis, characteristics and performance of synthesized photocatalyst. The adsorption activity for the chicken processing wastewater will be stirred magnetically in the dark condition for 26 h to ensure adsorption-desorption equilibrium is achieved, followed by photodegradation under the irradiation of LED light for 3 h. Meanwhile, the physicochemical properties of g-C_3N_4/PAC were examined using Brunauer-Emmett-Teller (BET), Fourier-Transform Infrared Spectroscopy (FTIR), X-ray Diffraction (XRD), Scanning Electron Microscope (SEM) and Energy Dispersive X-ray Analysis (EDX).

CHAPTER 2

LITERATURE REVIEW

2.1 Chicken Processing Wastewater

Recently, the demand for chicken increased dramatically due to the ease of access at low price. Consequently, poultry industries expanded rapidly in either large or small scale. Mostly, poultry slaughterhouses are located near the drainage system where the chicken processing wastewater can be discharged to a body of water easily. This untreated chicken processing wastewater is always characterized with high COD, BOD, TSS, TVS, TFS, blood and nutrient (nitrogen and phosphorus) (Rajakumar et al., 2011).

Consequently, the highly nutrient content in the chicken processing wastewater will eventually cause algae bloom when it is being discharged to a river. Algae are then decomposed into inorganic matter by microorganisms and this decomposition process consumes oxygen. When the oxygen demand becomes competent, aquatic life in the water bodies will be threatened and may then lead to environmental degradation. Furthermore, people will get sick easily when the epidermal diseases are outbreak of pathogenic bacteria from animal faeces (Rice, Caldwell and Humenik, 2006).

The sustainability of clean water is urged to protect the youngsters free from harmful wastewater and thus, Malaysia government has implemented the Environmental Quality Act (EQA) since 1974 to control the quality of the discharged effluent. EQA 1974 exercised its rights to ensure that the required effluent standards are complied by every sewage treatment plant included poultry farm (National Water Services Commission, 2019). Meanwhile, the designed effluent quality in compliance with EQA 1974 is given in Table 2.1.

Table 2.1: Design Effluent Values (National Water Services Commission, 2019).

Parameter	**Effluent Discharge to Rivers/Stream**				**Effluent Discharge to Stagnant Water Bodies**			
	Standard A		**Standard B**		**Standard A**		**Standard B**	
	Absolute	**Design**	**Absolute**	**Design**	**Absolute**	**Design**	**Absolute**	**Design**
BOD_5	20	10	50	20	20	10	50	20
SS	50	20	100	40	50	20	100	40
COD	120	60	200	100	120	60	200	100
Ammoniacal nitrogen (AMN)	10	5	20	10	5	2	5	2
Nitrate Nitrogen	20	10	50	20	10	5	10	5
Total Phosphorus	N/A	N/A	N/A	N/A	5	2	10	5
Oil and Grease (O&G)	5	2	10	5	5	2	10	5

Standard A is specified for discharge upstream of any raw water intake.

Standard B is specified for discharge downstream of any raw water intake.

2.1.1 Chicken Processing Wastewater Treatment Process

Chicken processing wastewater is usually treated using conventional technologies before it is disposed off. Generally, conventional chicken processing wastewater treatment process can be treated via physical, chemical and biological treatment process. For instance, the feathers can be removed by physical treatment using screening method (Young, 2014; Imam, 1984). The suspended debris and grit will then remove by a grit chamber, while a primary clarifier is used to remove any large particles that settle out by gravity. After that, almost 85 % of BOD_5 can be reduced with an aeration tank. However, there will be a generation of undesired activated sludge and this activated sludge is needed to be removed using a secondary clarifier. Meanwhile, recycling of part of the activated sludge to the aeration tank is needed to maintain the sufficient microbial activity. Lastly, the wastewater is dosed with the disinfectant such as fluoride and the treated wastewater is discharged to surface water. Figure 2.1 illustrates the overall conventional chicken processing wastewater treatment process.

However, conventional technologies have some drawbacks such as clogging may occur upon the screens and frequent cleaning is required. Grit chamber is also ineffective to remove tiny particles and pathogenic bacteria and viruses. Moreover, large amount of undesired sludge will be generated by activated sludge process and extra treatment is needed for the sludge generated. It is also requires skilled operators to maintain the activated sludge process. Meanwhile, coagulation precipitation has a comparative higher operational cost as it needs chemicals such as sodium hydroxide and limestone to cause the colloid to be precipitated and then can be removed in a sedimentation tank. Undesired waste stream will also generate by chemical precipitation and it requires additional treatment for these waste streams. Table 2.2 summarizes the drawbacks of conventional technologies.

Table 2.2: Drawbacks of Conventional Technologies.

Conventional Methods	**Drawbacks**	**References**
Screening	1. Frequent cleaning of the screens is required to prevent clogging.	Young, 2014; Imam, 1984
Grit chamber	1. Ineffective in removal of tiny particles and pathogens.	
Activated sludge	1. Generate large amount of undesired sludge. 2. Requires skilled operators to maintain the activated sludge process.	Mittal, 2011
Coagulation precipitation	1. Chemicals such as sodium hydroxide and limestone are needed which result in high operational cost. 2. Undesired waste stream may generate which requires additional treatment.	Sammer, 2014

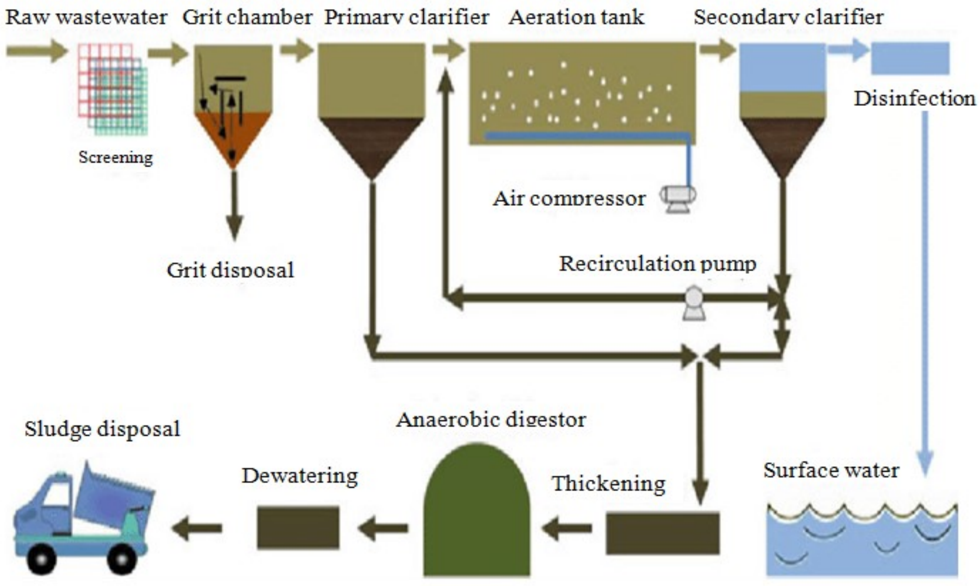

Figure 2.1: Chicken Processing Wastewater Treatment Process (Nash, 2013).

Into the bargain, refractory organic compounds are difficult to be removed by conventional method. These compounds may drag down or even stop the microorganism's activity during biological treatment. In the consideration of ineffectiveness of conventional wastewater treatment methods, advanced oxidation processes (AOPs) are developed to overcome the restraint of conventional methods (Deng and Zhao, 2015). In addition, various types of AOP treatments with their COD removal efficiency are tabulated in Table 2.3.

Table 2.3: Different Types of AOPs in COD Removal of Wastewater.

AOP types	**COD Removal Efficiency (%)**	**Mechanisms**	**Reference**
O_3	6 - 88	Direct O_3 oxidation	Deng, 2009
O_3/H_2O_2	18 - 78	Direct O_3 oxidation H_2O_2 oxidation	
O_3/UV	31 - 83	UV photolysis	
Fenton reaction	35 - 90	Iron coagulation Iron sludge-induced adsorption	
UV/TiO_2	20 - 90	UV photolysis	Bayarri et al., 2005
UV/H_2O_2	100	UV photolysis H_2O_2 oxidation	Liu, Kanjo and Mizutani, 2009
Photo-Fenton reaction	31 - 95	Iron coagulation Iron sludge-induced adsorption UV photolysis	Sing and Tang, 2013

2.2 Adsorption

Adsorption is a phenomenon when a gaseous or liquid phase adsorbate (molecule or ion) sticks upon a solid adsorbent surface. In contrast to absorption process, adsorption is termed as surface process which the adsorbate does not diffuse into the adsorbent's structure (Artioli, 2008).

Adsorption can be distinguished as physical adsorption and chemical adsorption (Sing, Rouquerol and Rouquerol, 1998). Physical adsorption involves the weak van der Waals forces and electrostatic interactions. Meanwhile, the strong chemical bonds such as covalent bonds held the adsorbate onto the surface of the adsorbent in a chemical adsorption (Donohue and Aranovich, 1998). Moreover, physical adsorption is always faster than chemical adsorption because only a monomolecular layer is involved in a chemical adsorption but physical adsorption often involves in thick and multilayer on the adsorbent's surface (Dabrowski, 2001). Thus, a larger surface area is provided by physical adsorption process when the layers are overlapping. Figure 2.2 illustrate the adsorption and desorption process on the surface of an adsorbent. Meanwhile, Figure 2.3 illustrates the differences between physisorption and chemisorption.

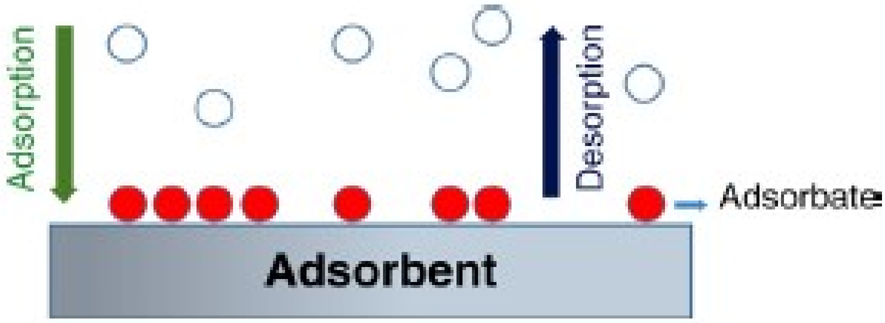

Figure 2.2: Schematic Diagram of Adsorption and Desorption Process (Limousin et al., 2007).

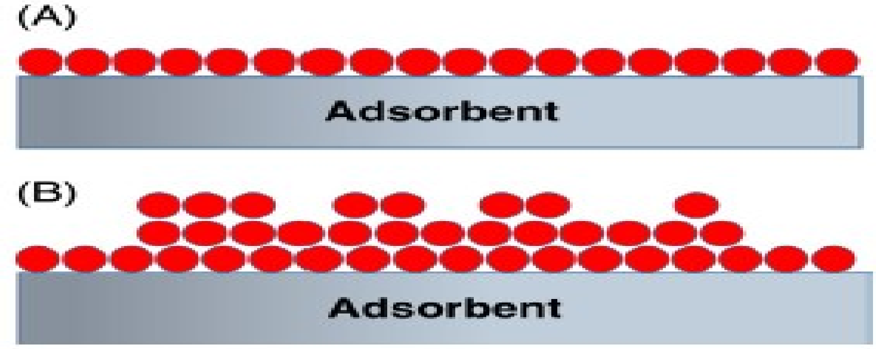

Figure 2.3: (A) Chemical Adsorption and (B) Physical Adsorption (Limousin et al., 2007).

Adsorption process has been used widely in industrial application such as drinking water deterioration (Karoly and Suzuki, 1992), removal of volatile organic chloride (VOC) compounds (Sakoda, Kawazoe and Suzuki, 1987), recovery of chlorofluorocarbons (CFCs) and wastewater treatment (Suzuki and Ha, 1984).

2.3 Heterogeneous Photocatalysis

Since 1912, the idea of driving organic synthesis using solar energy has been proposed by the Italian photochemist, Giacomo Luigi Ciamician. Nevertheless, the term photocatalysis is only accepted in the 1970's after the discovery of water splitting on a titanium dioxide (TiO_2) electrode by Fujishima and Honda (Fujishima and Honda, 1972). Heterogeneous photocatalysis occurs when a solid phase semiconductor such as TiO_2, zinc oxide (ZnO), iron (III) oxide (Fe_2O_3), tungsten trioxide (WO_3), tin (IV) oxide (SnO_2) and zirconium dioxide (ZrO_2) is irradiated under a source of light (Chou, Hwang and Sun, 2013; Boer, 1990). Moreover, the effectiveness of heterogeneous photocatalysis in removal of refractory pollutants has been studied by many researchers and now this technology is being commercialized in different fields such as hydrogen production by water splitting (Holladay et al., 2009), wastewater treatment (Ibhadon and Fitzpatrick, 2013), metal deposition (Serpone and Pelizzetti, 1989) and photoreduction of carbon dioxide (Aurian-Blajeni, Halmann and Manassenm 1980).

2.3.1 Mechanism of Heterogeneous Photocatalysis

Heterogeneous photocatalysis is a robust process where the redox reactions are driven by the solar photons to produce chemicals (Colmenares and Luque, 2013). Meanwhile, photocatalysis can be done in the company of light as energy sources such as ultraviolet, visible light, sunlight or infrared irradiation. Heterogeneous photocatalysis can remove the ambient concentration of either organic or inorganic species by which the photocatalyst is made up by solid phase semiconductors and the targeted species can be of gases or aqueous phase (Ibhadon and Fitzpatrick, 2013).

Furthermore, a chain of oxidative and reductive processes occurred upon the photocatalysts surface at same instant. The photocatalytic process will occur on the conduction band (CB); however, there is an energy band gap (E_{bg}) in between CB and valance band (VB). Conduction band is an unoccupied energy band whereas VB is a lowest occupied energy band. In order to initiate the photocatalytic process, E_{bg} must be overcome by exposing the photocatalyst under a source of light irradiation (Fox and Dulay, 1993; Lewis, 1993). The electrons from VB are then photo-excited and promoted to CB whenever the photon energy received is to be equal or greater than E_{bg} from the light source is illuminated on the photocatalyst surface. Consequently, this leaves behind a hole (h^+) in an unfilled VB and an electron hole (e^-) is created in CB as shown in equation (2.1) (Chong et al., 2010). However, energy may be dissipated as heat during the recombination of electron hole which as shown in equation (2.2) (Chong et al., 2010).

Photon Activation:

$$\text{photocatalyst} + \text{hv} \rightarrow e^- + h^+ \tag{2.1}$$

Recombination of electron-hole pairs:

$$e^- + h^+ \rightarrow \text{heat} \tag{2.2}$$

In the mean time, oxygen that has been adsorbed to the surface of photocatalyst will undergo the attack from free electron. As a result, equation (2.3) shows the formation of superoxide radical ion ($^{\bullet}O_2^-$) (Chong et al., 2010).

Oxygen Adsorption:

$$(O_2)_{ads} + e^- \rightarrow {}^{\bullet}O_2^- \tag{2.3}$$

Additionally, superoxide radical ion will further protonize to form HOO^- radical (equation 2.4 – 2.5) (Chong et al., 2010). Meanwhile, HOO^- radical can eventually behave like oxygen and having the similar scavenging properties with oxygen; hence, the photohole lifetime can be prolonged (equation 2.6 - 2.7) (Chong et al., 2010).

Water Ionization:

$$H_2O \rightarrow OH^- + H^+ \tag{2.4}$$

Superoxide Protonization:

$$ {}^{\bullet}O_2^- + H^+ \rightarrow HOO^- \tag{2.5}$$

$$HOO^- + e^- \rightarrow HO_2^- \tag{2.6}$$

$$HOO^- + H^+ \rightarrow H_2O_2 \tag{2.7}$$

Redox reaction then takes place on the photo-excited photocatalyst surface. Pollutant may now be oxidized to carboxyl radical ($R^{\bullet}$) and rendered unharmful indirectly via the combination with ${}^{\bullet}OH$ in the presence of water molecule (equation 2.8 - 2.10) (Chong et al., 2010).

$$H_2O + h^+ \rightarrow {}^{\bullet}OH + H^+ \tag{2.8}$$

$$R\text{-}H + {}^{\bullet}OH \rightarrow R^{\bullet} + H_2O \tag{2.9}$$

$$R^{\bullet} + h^+ \rightarrow CO_2 + H_2O + \text{mineral acid} \tag{2.10}$$

Overall, the photocatalytic process can be interpreted into the following steps (Chong et al., 2010; Ibhadon and Fitzpatrick, 2013; Herrmann, 1999):

(i) Mass transfer of pollutant from bulk liquid to the photocatalyst surface.

(ii) Pollutant is adsorbed onto the surface of photon excited photocatalyst.

(iii) Redox reaction takes place on the surface of photocatalyst where the $^{\bullet}OH$ radicals and H_2O_2 will be generated.

(iv) Final product is desorbed from the photocatalyst surface.

(v) Mass transfer of the final product into bulk liquid phase.

Figure 2.4 illustrates the mechanism of the overall photocatalytic process on the surface of titanium dioxide (TiO_2) (Ibhadon, 2008). An electron is being excited from ground state under irradiation of a source of light in which the light energy must be high enough to overcome the band gap energy. A hole is created at the VB and $^{\bullet}O_2^-$ are then formed under the attack from free electron generated (Anandan, Ikuma and Niwa, 2010). Meanwhile, the water molecule is oxidized and lead to the formation of $^{\bullet}OH$. Hydroxyl radical are then attack the organic pollutant which has been adsorbed onto the surface of TiO_2 and form $R^{\bullet}$ radical. Carboxyl radical will be oxidized in a hole and render the organic pollutant unharmful (Fujishima, Zhang and Tryk, 2008).

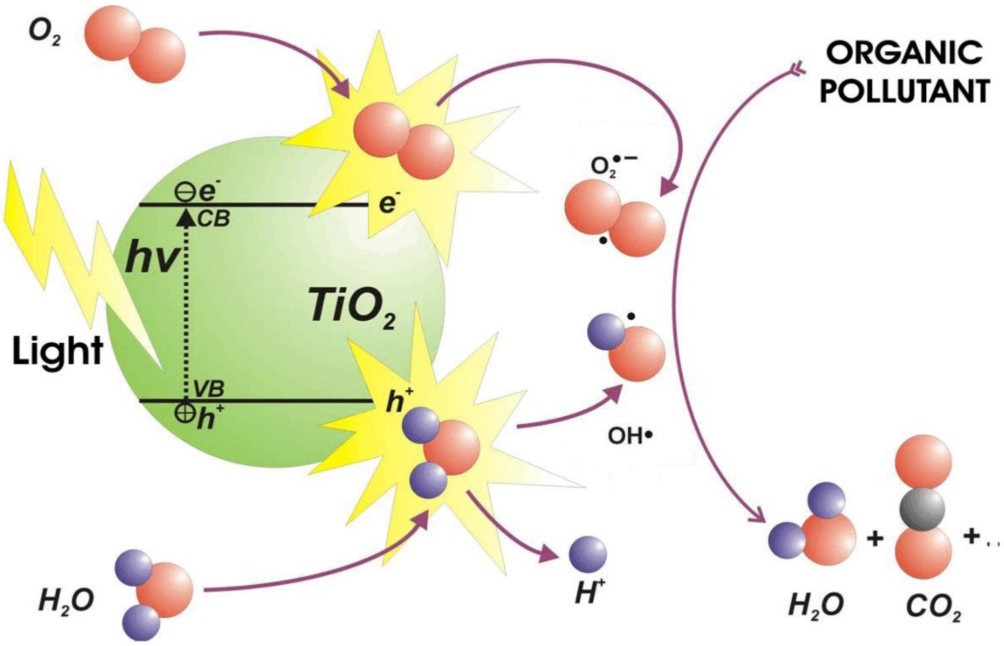

Figure 2.4: Scheme of a Photocatalytic Process (Ibhadon, 2008).

2.3.2 Benefits and Drawbacks of Heterogeneous Photocatalysis

Due to the ineffectiveness of conventional method, heterogeneous photocatalysis brought the attention of researchers due to its convenience factors. One of the benefits of photocatalysis is any organic, inorganic and microbial pollutants can be degraded almost completely under ambient temperature and pressure. Moreover, photocatalysis will not generate the undesired sludge as compared to conventional method such as coagulation precipitation (Sena, Moreira and Jose, 2008); so there is no need of post treatment of sludge and no secondary pollution will be generated (Dong et al., 2015). Furthermore, it is very convenient to some of the tropical countries such as Malaysia as the natural sunlight can be utilized as the energy source for photocatalysis. Countries with different seasons can use artificial light as the energy source as well. Although UV light is a harmful energy source, but it grants an advantage in which it own 24 h of accessibility.

Photocatalyst is non toxic, low cost and reusable (Hakobyan et al., 2019). Photocatalyst is supported on polymers, activated carbon and glasses to increase its active sites for interfacial reaction and prevent the agglomeration of photocatalysts in a suspension (Low et al., 2017; Malato et al., 2016; Srikanth et al., 2017; Li et al., 2010).

Nevertheless, photocatalytic process is associated with the energy band gap of the semiconductor. Some of the common used semiconductors such as titanium dioxide (TiO_2) and zinc oxide (ZnO) posses a large energy band gap which can only be energized by UV light. Usage of artificial UV light will be an expensive cost and not environmental friendly for the photocatalytic process. Moreover, UV light is harmful and protective aids are required during the handling of UV light. Besides, it is difficult for the separation of micro or nano-sized photocatalysts from the treated solution. As a result, a considerable amount of photocatalysts may loss during the separation and recovery process. Additionally, photocatalytic process consumes a long residence time to ensure the pollutants have been completely degraded (Hu et al., 2014).

In short, the advantages and disadvantages of heterogeneous photocatalysis have been listed out in Table 2.4.

Table 2.4: Advantages and Disadvantages of Heterogeneous Photocatalysis.

Advantages	Disadvantages
1. Complete degradation of pollutants.	1. Some of the semiconductors possess a large energy band gap which is energy intensive.
2. Operated under ambient condition.	2. Artificial UV light is a harmful energy source and expensive.
3. No sludge generation and thus, post-treatment of sludge is not needed.	3. Difficulty in separation and recovery of photocatalysts from treated solution.
4. Natural sunlight can be obtained as free energy source in tropical countries.	4. Time consuming due to long residence time.
5. Photocatalysts are cheap, non-toxic and can be reused.	
6. Photocatalysts can be supported on inert materials to increase its active sites for interfacial reaction.	

2.4 Activated Carbon (AC)

Activated carbon (AC) is a form of purified carbon with high adsorption capacity and is enclosed by complex structure that composed of carbon atoms (Bansal, Donnet and Stoeckli, 1988). Activated carbon is produced using lignocellulosic, wood and coal as raw materials (Koehlert, 2017). In the preparation of AC, there are two approaches in general which are physical activation and chemical activation.

Physical activation of AC consists of carbonization and activation processes. For instance, the precursor such as oil palm biomass is first undergo pyrolysis process at temperature of 450 ^{o}C in the absent of air. After carbonization of the precursors, it is then exposed to an oxidation agent (steam, carbon dioxide and air) at temperature of 600 – 800 ^{o}C (Daud, Ali and Sulaiman, 2000).

Activated carbon can be produced chemically as well. Materials with highly carbon content are impregnated with acids or bases such as phosphoric acid (Guo and Lua, 2002; Tiryaki et al., 2014) or potassium hydroxide (Foo and Hameed, 2011). Carbonization of impregnated carbonaceous materials is then occurred at the temperature of 300 - 500 ^{o}C, followed by the chemical activation of carbonaceous materials at the temperature of 800 ^{o}C with the exposure to nitrogen atmosphere (Zhang et al., 2017). In the comparison of preparation methods for AC, chemical activation has the advantages of lower activation temperature and shorter residence time is required (Kim et al., 2017).

Activated carbon has porous structure and its adsorption capacity is determined by its pore volume, pore size and interior surface (Kim et al., 2017). The pore structure of AC may vary in both size and shape due to the impurities of carbonaceous materials and carbonization process. In general, most of the ACs owns an average of pore diameter of 2.5 nm (Hameed, Tan and Ahmad, 2009). The adsorption property of AC is influenced by the chemical bond of heteroatoms that mainly composed of oxygen and hydrogen. In short, the chemical structure of AC depends on the arrangement of electron clouds within the pore structure. The deviation in the arrangement of electron will lead to the creation of unpaired electrons and unsaturated valence bond. Thus, the chemical bonding within AC has the significant effect on the adsorption characteristics as well (Bansal, Donnet and Stoeckli, 1988).

2.4.1 Application of AC

Nowadays, AC has a wide applicability. One of the common applications is to control the gasoline vapour emission in automobile canister (Ioannidou and Zabaniotou, 2007). Moreover, harmful components within tobacco can be adsorbed upon the cigarette filters impregnated with AC. Activated carbon is favourably used as catalyst support because it provides a large internal surface for catalytic reaction. Furthermore, AC can remove the poisonous heavy metal ions in aqueous solution such as cadmium, mercury and chromium which makes them useful in both water and wastewater treatment (Nayak et al., 2017; Kwiatkowski, Kalderis and Diamadopoulos, 2017). The primary role of AC in water treatment is to adsorb dissolved organic molecules and to banish the unpleasant odour, taste and colour (Bansal, Donnet and Stoeckli, 1988).

2.4.2 Mechanism of AC in Degradation of Pollutant

The concentration of the pollutant can be reduced through adsorption process onto AC surface. Adsorption is a physical process where the pollutant will be deposited upon the solid phase AC and chemical reaction will not occur at this stage. When AC is brought into contact with pollutant, the concentration of pollutant will reduce gradually as it accumulates on the surface of AC while van der Waals forces act as the molecular attraction to hold pollutant onto the surface of AC (Kumar, 2012). The larger dissolved organic molecules will be trapped into the macropores of AC whereas the smaller dissolved organic molecule will trapped into the micropores of AC. A sufficient period of contact time is needed to allow adsorption equilibrium between the concentration of AC and pollutant. Once the concentration of the pollutant has been successfully reduced, it will undergo desorption process from AC in which desorption is a process that the pollutant is detached from the surface of AC (Lin et al., 2016). Figure 2.5 shows an overall adsorption mechanism of AC.

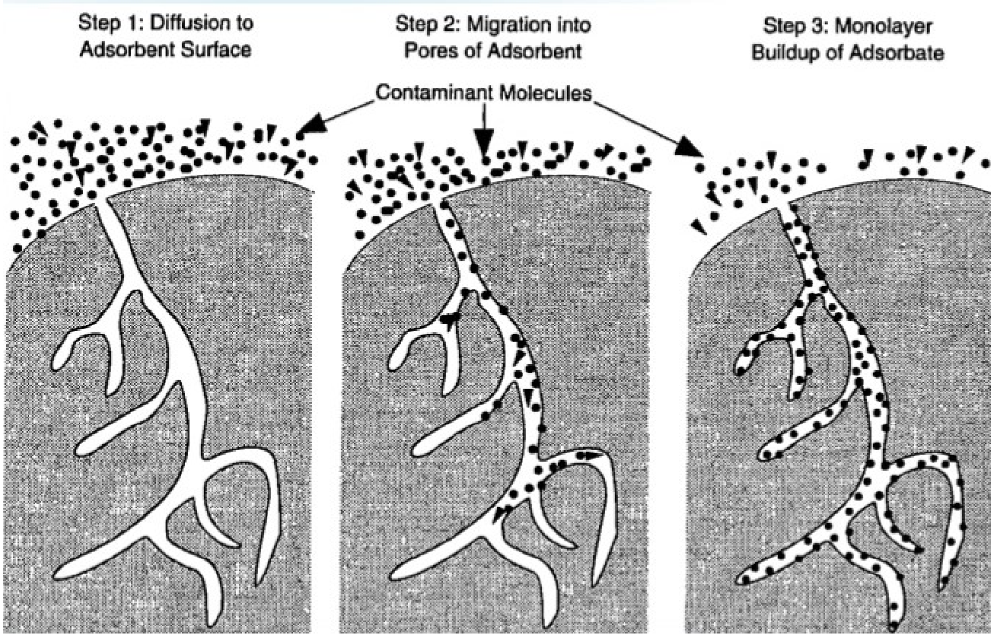

Figure 2.5: Adsorption Mechanisms on Adsorbent Surface (Kumar, 2012).

2.4.3 Benefits and Drawbacks of AC

In general, activated carbon has numerous advantages over other carriers. First of all, AC is inert. Due to the inert nature by AC, the hydrocarbons will not be decomposed and lead to poisoning of the catalyst when the metal ion pollutants are being adsorbed onto the surface of AC. Moreover, AC can provide a comparatively large internal surface for adsorption and thus, AC is more effective to be used for the removal of pollutants. Activated carbon has a strong stability and resistant against attacking in acid and base solutions (Wong et al., 2017). As a comparison to other oxide carriers, AC will not be deformed when the adsorption process occurs at a high temperature and it remains stable up to its activation temperature (>900 ^{o}C) (Reimerink, 1999). However, some other oxide carriers such as silica will undergo the decomposition of the hydroxyl groups in the adsorption process with high temperature. Furthermore, AC is relatively cheap in contrast to other carriers (Reimerink, 1999).

However, AC has some limitations. One of the limitations is AC will become saturated with pollutant and the spent AC is needed to be removed and disposed of. Otherwise, blockages on the pore system of AC may occur and lead to ineffective of pollutant's removal (Ciminello, 2005). Besides, AC cannot be used for the disinfection of pathogenic bacteria and viruses in a water treatment process. As a result, bacteria may continue grow and become epidemic (Reimerink, 1999).

In short, Table 2.5 summarizes the overall advantages and disadvantages of AC.

Table 2.5: Advantages and Disadvantages of AC

Advantages	Disadvantages
➢ Activated carbon is inert, hydrocarbons will not decompose as the adsorption process involves of metal ions.	➢ Removal of the spent AC is required once the AC is saturated with pollutants.
➢ Effectively in degradation of pollutant due to a large internal surface provided by AC for adsorption process.	➢ Ineffective to remove pathogenic bacteria and viruses.
➢ Strong stability and resistant against acid and base solutions.	.
➢ Can be bought at cheap cost.	

2.5 Graphitic Carbon Nitride (g-C_3N_4)

In modern technology development, researchers implemented photocatalysis in order to receive the maximum solar energy output. Generally, solar energy is dominated by three regions of electromagnetic spectrum which are UV (~5 %), visible light (~45 %) and IR (~50 %) (Jestin, 2012). Nevertheless, most photocatalysts require a large energy band gap for photocatalysis. For instance, TiO_2 is only active under UV irradiation (<385 nm) attributed to its extremely wide band gaps (3.0 – 3.2 eV) which can be energy intensive (Kumar, Karthikeyan and Lee, 2018). Thus, g-C_3N_4 is brought into the attention of the researchers. Graphitic carbon nitride is a metal-free and polymeric semiconductor which is able to absorb visible light due to its narrower band gap (~2.7 eV) (Kumar, Karthikeyan and Lee, 2018). Figure 2.6 illustrates the band gaps required by different types of semiconductor. Moreover, g-C_3N_4 is also characterized by high thermal (>500 ^oC) and chemical stability to oxidation (Santosh et al., 2013). It is known as the most stable allotrope at ambient conditions. Graphitic carbon nitride comprises of mostly carbon and nitrogen atoms which forms a layer of hexagonal carbon rings structure. The stacking layer is held by weak van der Waals force (Kumar, Karthikeyan and Lee, 2018).

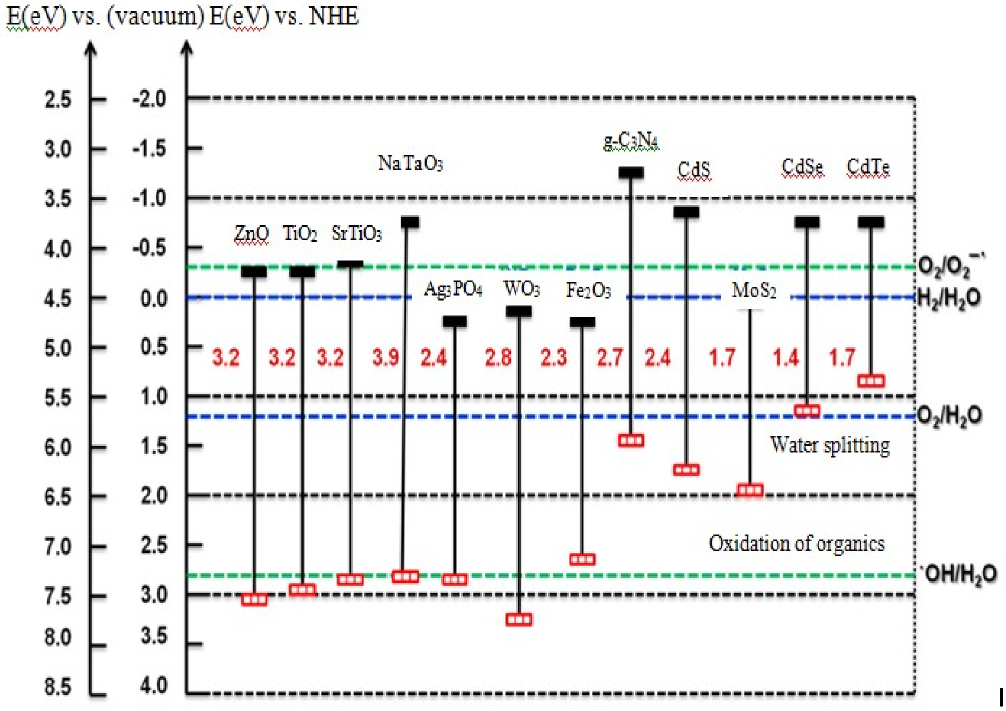

Figure 2.6: Energy Band Gaps of Different Semiconductors (Kumar, Karthikeyan and Lee, 2018).

2.5.1 Synthesis Method of g-C_3N_4

Graphitic carbon nitride can be synthesized by pyrolysis using urea (Liu et al., 2011), cyanamide (Yu et al., 2014), dicyandiamide (Yu, Li and Zhang, 2014), melamine (Li et al., 2009) and thiourea (Dong et al., 2012) as a precursor. The structure of g-C_3N_4 depends on the synthesis method such as thermal condensation (Zhang et al., 2013), physical vapour deposition (PVD) (Gago et al., 2001), chemical vapour deposition (CVD) (Wang et al., 2014), solid state reaction (Lu et al., 2017) and solvothermal method (Lu et al., 2017). Although g-C_3N_4 can be synthesized at different conditions, but it is unstable above 600 ^{o}C and it will produces nitrogen and cyano fragment when the temperature goes beyond 700 ^{o}C (Wang et al., 2017). Graphitic carbon nitride will not be fully formed below 500 ^{o}C (Mo et al., 2015). Table 2.6 summarizes the characteristics of g-C_3N_4 synthesized at different conditions. Meanwhile, Figure 2.7 illustrates the synthesis process of g-C_3N_4 by thermal condensation of different precursors such as melamine, cyanamide, dicyandiamide, urea and thiourea.

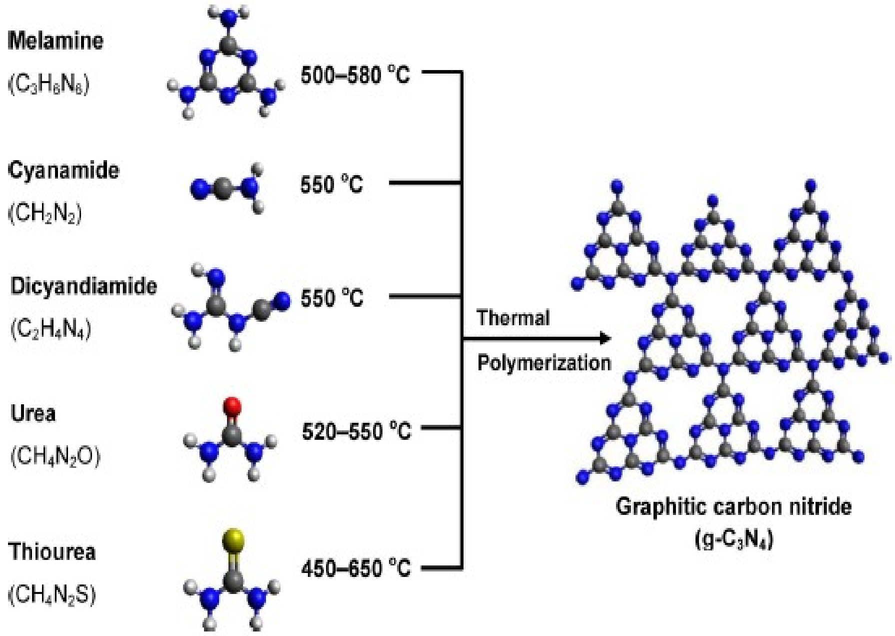

Figure 2.7: Synthesis Process of g-C_3N_4 by Thermal Condensation of Different Precursors such as Melamine (Yan, Li and Zou, 2009), Cyanamide (Wang et al., 2009), Dicyandiamide (Bai et al., 2014), Urea (Zhang et al., 2012; Ong et al., 2015) and Thiourea (Zhang et al., 2012).

Table 2.6: Characteristics of g-C_3N_4 Synthesized by Thermal Condensation.

Precursor	**Condition**	**Band Gaps (eV)**	**BET Specific Surface Area (m^2/g)**	**Reference**
Cyanamide	550 ^oC at 4 h, air	2.70	10.0	Wang et al., 2009
Dicyandiamide	550 ^oC at 2 h, air	2.75	10.0	Zhang et al., 2012
	550 ^oC at 3 h, air	2.66	12.3	
	600 ^oC at 4 h, air	2.75	12.8	Martin et al., 2014
	550 ^oC at 4 h, H_2 atmosphere	2.00	20.91	Tay et al., 2015
	550 ^oC at 4 h, air, subsequently 540 ^oC at 2 h, H_2 atmosphere	2.03	N/A	Niu et al., 2014
	550 ^oC at 4 h, air, subsequently 550 ^oC at 2 h, H_2 atmosphere	2.84	124.0	Li et al., 2015
	550 ^oC at 4 h, N_2 atmosphere, subsequently 510 ^oC at 1 h, NH_3 atmosphere	2.59	196.0	Liang et al., 2015
	500 ^oC at 4 h, air, subsequently 620 ^oC at 2 h, Ar atmosphere	1.90	N/A	Kang et al., 2015
Melamine	450 ^oC at 2 h, air	N/A	N/A	Mo et al., 2015
	500 ^oC at 2 h, air	2.83	7.1	

Table 2.6: (Continued).

Precursor	**Condition**	**Band Gaps (eV)**	**BET Specific Surface Area (m^2/g)**	**Reference**
Melamine	550 °C at 2 h, air	2.78	8.6	Mo et al., 2015
	600 °C at 2 h, air	2.71	11.7	
	650 °C at 2 h, air	2.74	46.8	
	600 °C at 4 h, Ar atmosphere	2.69	8.6	Yan, Chen and Xu, 2012
	520 °C at 2 h, N_2 atmosphere	2.74	17.4	
Urea	550 °C at 0 h, air	2.72	31.0	Dong et al., 2013
	550 °C at 1 h, air	2.68	62.0	
	550 °C at 2 h, air	2.72	75.0	
	550 °C at 3 h, air	2.78	288.0	
	450 °C at 2 h, air	2.79	43.0	Zhang et al., 2012
	500 °C at 2 h, air	2.70	49.0	
	550 °C at 2 h, air	2.66	58.0	
	600 °C at 2 h, air	2.67	77.0	

Table 2.6: (Continued).

Precursor	**Condition**	**Band Gaps (eV)**	**BET Specific Surface Area (m^2/g)**	**Reference**
Urea	650 ^oC at 2 h, air	2.69	97.0	Zhang et al., 2012
Thiourea	450 ^oC at 2 h, air	2.71	11.0	
	500 ^oC at 2 h, air	2.70	17.0	
	550 ^oC at 2 h, air	2.58	18.0	
	600 ^oC at 2 h, air	2.62	27.0	
	650 ^oC at 2 h, air	2.76	52.0	

2.5.2 Application of g-C_3N_4

Applications of g-C_3N_4 can be very wide since they are environmental friendly, metal-free and can be purchased at low cost (Umar and Aziz, 2006). These applications included water treatment (Deng et al., 2018), sensing (Zhan et al., 2017), bio-imaging (Zhan et al., 2017), photodynamic therapy (Zhan et al., 2017) and production of hydrogen from water (Cao and Yu, 2014).

2.5.3 Benefits and Drawbacks of g-C_3N_4

In photocatalytic application, energy band gap is the most concern factor which determines the accessibility and the energy usage by the photocatalysis. Graphitic carbon nitride owns the advantage of moderate band gap (2.7 – 2.8 eV) (Kumar, Karthikeyan and Lee, 2018). The moderate band gap owned by g-C_3N_4 enables the photocatalytic process occurs in visible light region which is the majority in solar spectrum. Moreover, g-C_3N_4 has the advantages of low cost, metal-free, easy fabrication, high thermal and chemical stability (Santosh et al., 2013).

Nonetheless, g-C_3N_4 exhibits low photocatalytic efficiency in bulk usage owning to its low surface area which reduces the active sites for interfacial reactions Furthermore, the energy dissipated as heat due to the high recombination rate of electron-hole pairs in g-C_3N_4 (Inagaki et al., 2019). The advantages and disadvantages of g-C_3N_4 are tabulated in Table 2.7.

Table 2.7: Advantages and Disadvantages of g-C_3N_4.

Advantages	Disadvantages
Moderate band gaps (2.7 – 2.8 eV) will allows g-C_3N_4 to be active under irradiation of visible light.	Limited active sites for interfacial reactions.
Low cost.	High rate of electron-hole recombination.
Metal-free and easy fabrication.	
High thermal (>500 ^{o}C) and chemical stability.	

2.6 Photocatalytic Application of Photocatalyst Supported on AC

A wide range of organic pollutants can be degraded via photocatalytic process. Photocatalysis is employed in water treatment for destruction and removal of contaminants, reduction of heavy metals and disinfection (Ollis, 2000).

Activated carbon is ineffective to remove the pathogenic bacteria and viruses because these pathogenic bacteria and viruses are too small to be removed by adsorption onto the pore structure of AC (Reimerink, 1999). Hence, photocatalytic process is suitable for water treatment since it is more effective in the removal of refractory pollutants (Dunlop et al., 2002). However, the specific surface area of photocatalysts like TiO_2, ZnO and g-C_3N_4 is too low for interfacial reactions to be occurred. Aggregation of photocatalysts could be avoided by the uniform distribution of photocatalysts on the surface of AC. Furthermore, the rate of transfer and rate of accumulation of pollutants onto the surface of photocatalysts will be accelerated due to the strong adsorption ability provided by AC. Hence, the overall efficiency of photocatalytic process can be enhanced even in a pollutant-rich environment.

In addition, the proposed mechanism of photocatalyst supported on AC is different from the conventional mechanism which only involves photocatalysis. The pollutants are first being adsorbed onto the AC surface until adsorption-desorption equilibrium is reached. The adsorbed pollutants will then undergo photocatalysis on the active surface of photocatalyst. In contrast to conventional mechanism, the pollutants will be retained on the AC surface by adsorption and these reaction intermediates will undergo subsequent photocatalytic process to complete the degradation and mineralization. Figure 2.8 illustrates the proposed mechanism of photocatalysis for immobilised semiconductors. Meanwhile, Table 2.8 has summarized the degradation efficiency of organic pollutant by different photocatalysts.

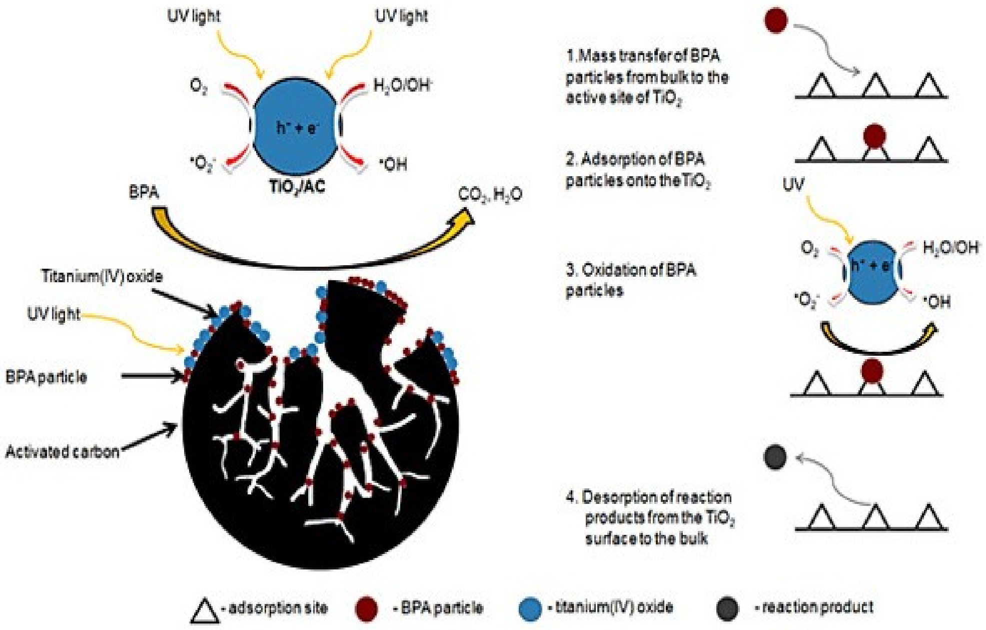

Figure 2.8: Proposed Mechanism of Adsorption and Decomposition of Bisphenol A. on Modified Photocatalysts (Zawadzki, Kudlek and Dudziak, 2018).

Table 2.8: Removal Efficiency of Organic Pollutant by Different Photocatalysts.

Catalyst	**Organic Pollutant**	**Reaction Time (min)**	**Source of Light**	**Removal Efficiency (%)**	**Reference**
Pure Ag/AgCl	Methyl Orange	300	Visible Light	15.1	McEvoy, 2014
0.7 Ag/AgCl: 1 AC				98.1	
1.5 Ag/AgCl: 1 AC				97.9	
2 Ag/AgCl: 1 AC				97.3	
2.5 Ag/AgCl: 1 AC				88.1	
3 Ag/AgCl: 1 AC				77.6	
GAC	TVS in wastewater	240	-	38.3	Asha and Kumar, 2014
	BOD in wastewater			52.3	
	TS in wastewater			46.7	
PAC	TVS in wastewater		-	40.1	
	BOD in wastewater			55.7	
	TS in wastewater			82.0	

Table 2.8: (Continued).

Catalyst	Organic Pollutant	Reaction Time (min)	Source of Light	Removal Efficiency (%)	Reference
Pure TiO_2	TVS in wastewater	240	14 W of UV energy	100	Asha and Kumar, 2014
	BOD in wastewater			82.0	
	TS in wastewater			42.3	
40.52 wt% TiO_2/GAC	TVS in wastewater			100	
	BOD in wastewater			100	
	TS in wastewater			85.0	
	Coliform in wastewater			100	
78.5 wt% TiO_2/PAC	TVS in wastewater			100	
	BOD in wastewater			100	
	TS in wastewater			92.0	
	Coliform in wastewater			100	
2 wt% Fe_3O_4/g-C_3N_4	2,4,6-trichlorophenol	100	Visible Light	96.0	Yang et al., 2016
2 wt% Er^{3+}/g-C_3N_4	Rhodamine B		White LED	100	Xu et al., 2014

Table 2.8: (Continued).

Catalyst	Organic Pollutant	Reaction Time (min)	Source of Light	Removal Efficiency (%)	Reference
10 wt% Ag/g-C_3N_4	Nitrogen Oxide	180	300 W Tungsten Halogen Lamp	54.3	Sun et al., 2015
1 wt% Ag/g-C_3N_4	Methyl Orange		500 W Xe Lamp	100	Ge et al., 2011
12 wt% $BaTiO_3$/g-C_3N_4		360	200 W Xe Lamp	76.0	Xian et al., 2015
25 wt% Ag_3PO_4/g-C_3N_4		15	350 W Xe Lamp	100	Katsumata et al., 2014
ZnO		60	Visible Light	88.5	Jaramillo-Páez et al., 2018
ZnO	Rhodamine B			86.4	
ZnO	Phenol			97.7	

Based on the literature review, there are some drawbacks shown by the pure g-C_3N_4 in which the pure g-C_3N_4 will self-agglomerate to reduce its active site for photocatalytic reaction. Besides, the AC also found to be inefficient in photocatalytic reaction. Moreover, based on the Table 2.8 that has been tabulated, there is also lack of study on the combination of g-C_3N_4 and AC. Thus, this project will investigate the adsorption-photocatalytic performance of g-C_3N_4/PAC composite on the degradation of chicken processing wastewater in which AC is able to provide a larger surface area for g-C_3N_4 for interfacial reaction while the self-aggregation of g-C_3N_4 can be avoided.

CHAPTER 3

METHODOLOGY

3.1 Experimental Flow Chart

The overall flow of the project is summarized in Figure 3.1.

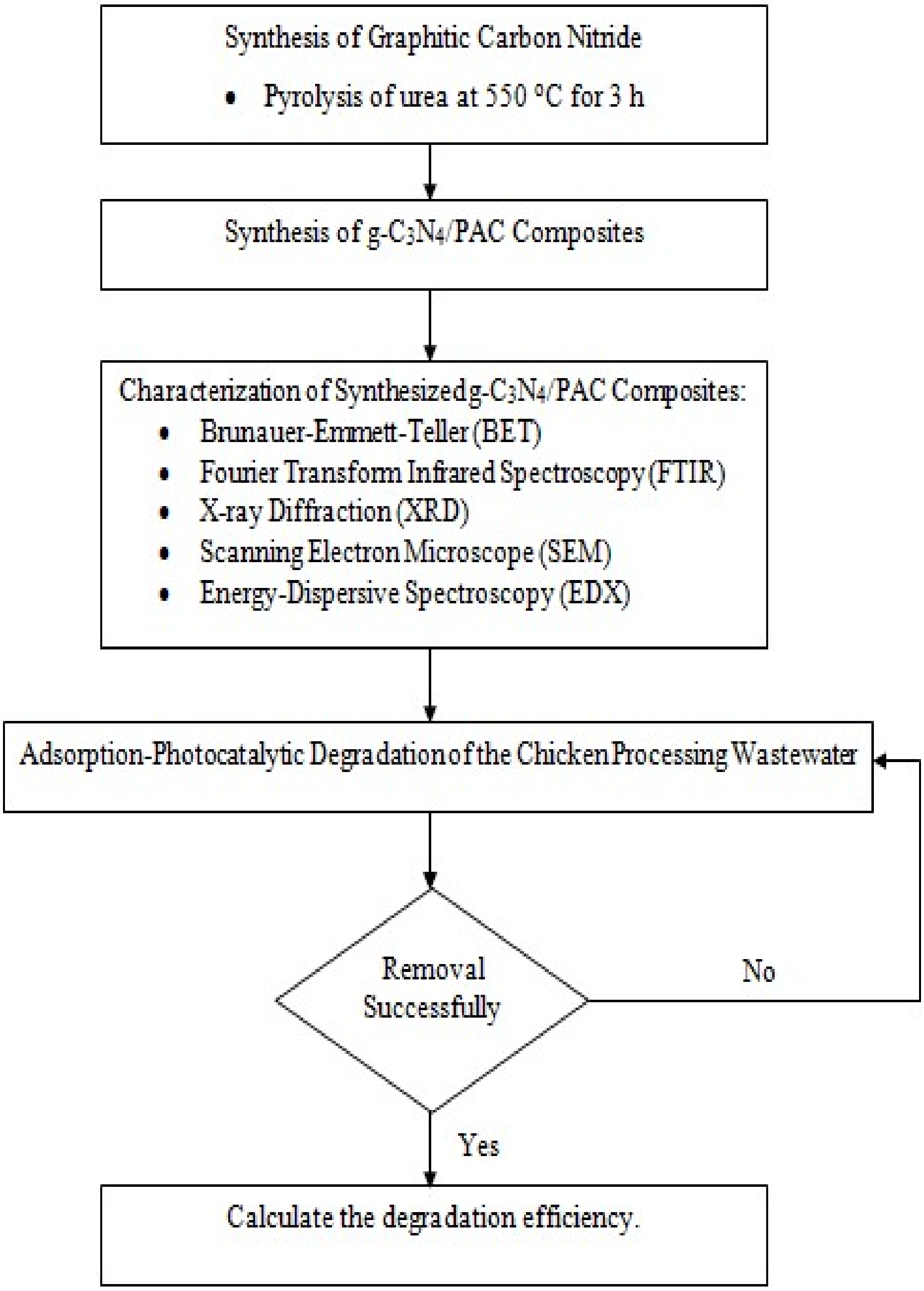

Figure 3.1: Methodology Flow of the Project.

3.2 Materials and Chemicals

Chicken processing wastewater was obtained and collected as model pollutant from Sungai Long's wet market. All the chemical reagents used were of analytical grade and purity. Urea powder (Merck, >99 %) was used as the precursor to synthesize g-C_3N_4 through pyrolysis method. Activated carbon powder (R&M Chemical, >99 %) was used as adsorbent of contaminants in chicken processing wastewater. Low range chemical oxygen demand (COD) digestion reagent vials (HACH) were used to measure the amount of oxygen that would depleted in a body of receiving water by the organisms from chicken processing wastewater. Phosphate reagent powder pillow (HACH) was used to analyze the orthophosphate content in the chicken processing wastewater. Ammonium cyanurate reagent powder pillow (HACH) and ammonium salicylate reagent powder pillow were used to analyze the ammonia nitrogen content in the chicken processing wastewater.

3.3 Synthesis of Pure g-C_3N_4

Urea powder was wrapped with an aluminum foil (to prevent heat loss to the surrounding) and put into an alumina crucible with a cover to avoid urea from over reacting with oxygen. The crucible was then calcinated at 550 ^oC in a muffle furnace for 3 hours. The temperature was increased at a rate of 15 ^oC /min to prevent formation of uneven pore structure due to the rapid bubble velocity effect (Cao et al., 2015). Graphitic carbon nitride was then collected as yellowish product after it is cooled down to room temperature as shown in Figure 3.2.

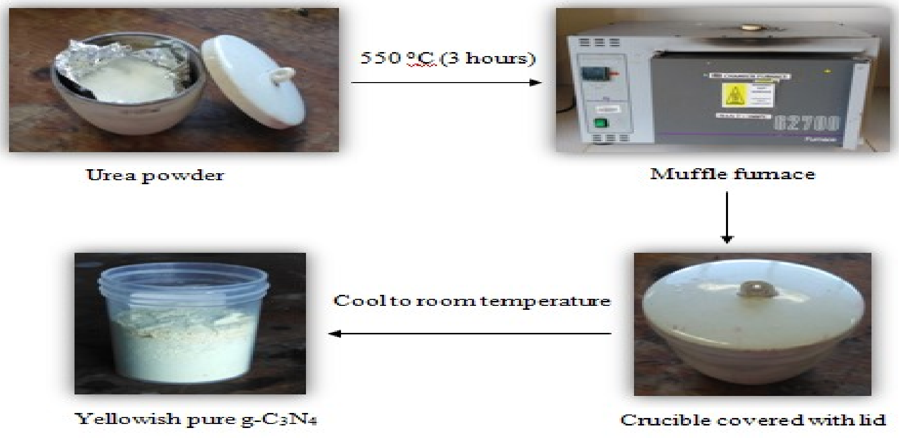

Figure 3.2: Synthesis Method of Pure g-C_3N_4.

3.4 Preparation of g-C_3N_4/PAC Composites

10 g of PAC was dissolved in the 10 mL of distilled water to form PAC solution. In order to prepare 20 wt% g-C_3N_4/PAC composite, 2.50 g of urea powder was mixed into the PAC solution. The suspension was stirred vigorously using a magnetic stirrer for 24 hours under room temperature to achieve homogenous mixing. After that, the suspension was dried in an oven at 80 ^{o}C for overnight. The dried composite was then further calcinated at 550 ^{o}C in a muffle furnace for 3 hours (He et al., 2018). The procedures were repeated by varying the weight percentage of g-C_3N_4 in order to synthesize 40 wt% and 60 wt% of g-C_3N_4/PAC composites accordingly.

3.5 Characterization of g-C_3N_4/PAC Composites

Characterization of synthesized photocatalyst can be done by using different instruments such as Brunauer-Emmett-Teller (BET), Fourier Transform Infrared Spectroscopy (FTIR), X-ray Diffraction (XRD), Scanning Electron Microscope (SEM) and Energy-dispersive X-ray Spectroscopy (EDX). The BET (micromeritics ASAP 2020) specific surface area of the AC and different weight percentage of g-C_3N_4/PAC composites were demonstrated by N_2 adsorption-desorption analysis at -195.791 ^{o}C. The functional group of activated carbon, pure g-C_3N_4 and g-C_3N_4/PAC composites were analyzed using FTIR (Nicolet iS10) spectroscopy with the wavelength in the range of 500 – 4000 cm^{-1}. Besides, the crystallite structure of the AC, pure g-C_3N_4 and g-C_3N_4/PAC composites were analyzed using XRD (Shimadzu XRD-6000) in the range of 10 – 80 ^{o} with the rate of 2 ^{o}/min. Moreover, the surface morphology of the AC, pure g-C_3N_4 and g-C_3N_4/PAC composites were analysed using SEM (Hitachi, S-3400N, Ametek). EDX (Hitachi, S-3400N, Ametek) was used to determine the elemental composition of AC, pure g-C_3N_4 and g-C_3N_4/PAC composites.

3.6 Adsorption-Photocatalytic Degradation of the Chicken Processing Wastewater

The adsorption and photocatalytic performance of the synthesized catalysts were evaluated using chicken processing wastewater as model pollutant.

A 200 mL of chicken processing wastewater was measured and transferred to a beaker. The beaker was added with 1.20 g of 20 wt% g-C_3N_4/PAC. The adsorption activity for the chicken processing wastewater was then stirred magnetically in the dark condition for 26 h to ensure adsorption-desorption equilibrium is achieved (Asha and Kumar, 2014). The treated samples were collected at every 2 h interval.

The beaker was then undergoing LED light irradiation to carry out photocatalytic process for 3 hours in which each samples were collected at every 30 minutes interval (Asha and Kumar, 2014). All the samples collected were analyzed by carry out COD, orthophosphate and ammonia nitrogen test accordingly. The procedures were repeated for 40 wt% g-C_3N_4/PAC and 60 wt% g-C_3N_4/PAC. Figure 3.3 shows the adsorption-photocatalytic degradation of chicken processing wastewater.

Meanwhile, the degradation rate of chicken processing wastewater can be calculated by the following equation:

$$Degradation\, rate\ (\%) = \frac{C_0 - C}{C_0} \times 100\ \%$$

Where,

C_0 = initial concentration of chicken processing wastewater;

C = final concentration of chicken processing wastewater.

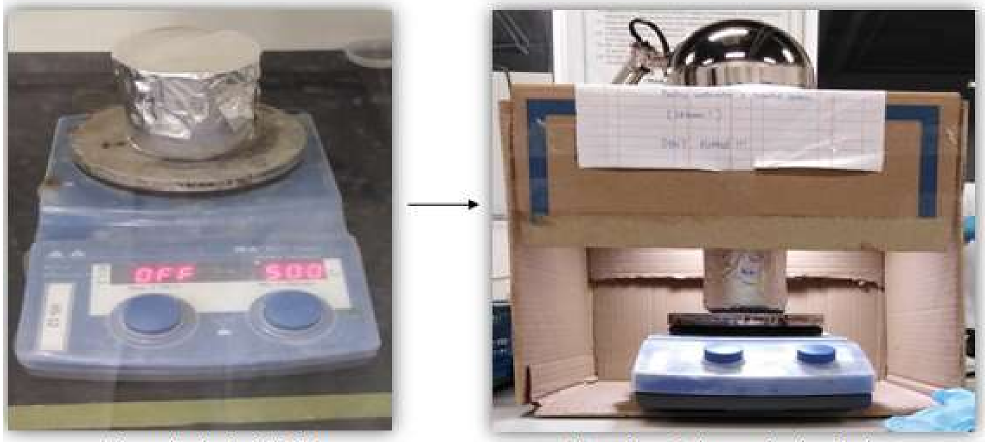

Adsorption in dark (26 h)

Photodegradation under irradiation of LED light (180 min)

Figure 3.3: Adsorption-Photocatalytic Degradation of Chicken Processing Wastewater.

3.7 Separation of Catalyst

A 1.20 mL of treated chicken processing wastewater was transferred from the beaker to a micro centrifuge tube using a micropipette. The catalyst was then separated out from the treated chicken processing wastewater by centrifuge at 12000 rpm for 15 minutes as shown in Figure 3.4. The separated catalysts were then analyzed by FTIR.

Figure 3.4: Separation of Catalyst by Centrifuge.

3.8 Chemical Oxygen Demand (COD) Test

The treated chicken processing wastewater was diluted to a dilution factor of 100 with distilled water. Digester was preheated to 150 °C. Caps from two COD digestion reagent vials were removed. Hold one vial at a 45-degree angle and 2.00 mL of the treated chicken processing wastewater was added into the vial using a micropipette. Hold another vial at a 45-degree angle and 2.00 mL of deionised water was added into the vial using a micropipette. The vials were capped tightly. The vials were inverted gently for several times to for mixing purpose. The vials were inserted into the preheated digester and the protective lid was closed. The vials were heated for 2 h. Digester was then turned off and the vials were allowed to cool down to 120 °C or less. Each vial was inverted several times while it was still warm (HACH, 2014). The vials were cooled down to room temperature as shown in Figure 3.5.

HACH spectrophotometer DR 3900 was used to determine the COD value. Low-range COD programme was selected. The blank vial was inserted into the vials holder and set to “ZERO”. The sample vial was inserted into the vials holder and results were “READ” in mg/L COD.

Figure 3.5: COD Test of Chicken Processing Wastewater.

3.9 Orthophosphate Test

The treated chicken processing wastewater was diluted to a dilution factor of 100 with distilled water. Programme 490 Phosphorus Powder Pillow was selected. A 10 mL of the treated chicken processing wastewater was filled into a sample cell. PhosVer3 phosphate powder pillow was added and a blue colour of solution will be developed (if orthophosphate was presented in the solution). The sample cell was caped and shaked for 20 – 30 seconds (HACH, 2017).

Another sample cell was filled by 10 mL of deionised water. The first sample cell that filled with treated chicken processing wastewater was wiped and cleaned after two minutes reaction time. The blank sample cell was inserted into the cell holder and set to “ZERO”. The sample cell with treated chicken processing wastewater was inserted to the cell holder and the result was “READ” in mg/L PO_4^{3-} (HACH, 2017). Figure 3.6 shows the orthophosphate test of the chicken processing wastewater.

Figure 3.6: Orthophosphate Test of Chicken Processing Wastewater.

3.10 Ammonia Nitrogen Test

The treated chicken processing wastewater was diluted to a dilution factor of 100 with distilled water. Programme 380 Ammonia Nitrogen Salicylate was selected. 10 mL of the treated chicken processing wastewater and 10 mL of deionised water were filled into each sample cell respectively. Ammonia salicylate reagent powder pillow was added to each sample cell. Both sample cells were capped and shaked to dissolved the reagent powder pillow. Ammonia cyanurate reagent powder pillow was then added to each sample cell after three minutes reaction time of ammonia salicylate. Fifteen minutes of reaction time was required for the ammonia cyanurate with chicken processing wastewater. Both sample cell were wiped and cleaned after fifteen minutes reaction time. The blank sample cell was inserted into the cell holder and set to “ZERO”. The sample cell with treated chicken processing wastewater was inserted to the cell holder and the result was “READ” in mg/L NH_3-N (HACH, 2015). Figure 3.7 shows the ammonia nitrogen test of chicken processing wastewater.

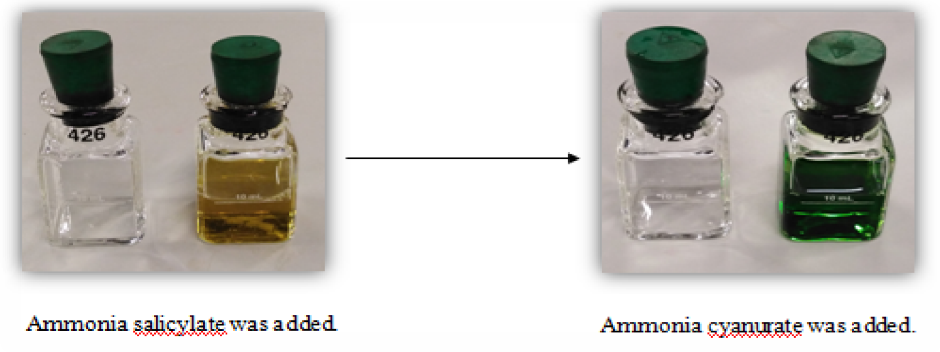

Ammonia salicylate was added

Ammonia cyanurate was added.

Figure 3.7: Ammonia Nitrogen Test of Chicken Processing Wastewater.

CHAPTER 4

RESULTS AND DISCUSSION

4.1 Brunauer-Emmett-Teller (BET) Analysis

Figure 4.1 presents the N_2 adsorption-desorption isotherms of activated carbon and different weight percentage of g-C_3N_4/PAC composites; whereas, Figure 4.2 shows the N_2 adsorption-desorption isotherms of pure g-C_3N_4. Based on Figure 4.1, it shows a rapid increase in adsorption isotherm at a low relative pressure without the formation of plateau. The adsorption isotherm continues the uptake trend at a higher relative pressure even when the relative pressure reaches unity. The steep slope at low relative pressures reveals that the highly porous structure of catalyst was formed with narrow pore size distribution (Rouquerol, Rouquerol and Sing, 1999; Zhang, Yu and Feng, 2006; Warhurst et al., 1997). Furthermore, the shape of adsorption isotherms for AC and g-C_3N_4/PAC composites was fitted to Type II isotherms (Thommes et al., 2015).

Figure 4.2 shows an uptake trend in which the N_2 adsorption isotherm was increased exponentially with increasing relative pressure and the uptake trend continues until the relative pressure approaches to unity. This reveals that the pure g-C_3N_4 was fitted by Type III adsorption isotherm (Thommes et al., 2015).

Meanwhile, Table 4.1 summarizes the BET specific surface area (S_{BET}), total pore volume (V_{tot}), and average pore diameter (D_{pore}) for the synthesized catalysts. It clearly shows that the S_{BET} for different weight percentage of g-C_3N_4/PAC composites was much larger than the bulk g-C_3N_4 and this was attributed to the presence of AC which inhibited the agglomeration of g-C_3N_4 (Chen, Kuo and Lu, 2016). Activated carbon with higher S_{BET} could act as a support catalyst to increase the surface area of g-C_3N_4 (74.7993 m^2/g). Certainly, the enhancement in the S_{BET} will increase active site for adsorption and lead to a greater adsorption capability of the composites for heterogeneous photocatalytic reaction (Chen, Kuo and Lu, 2016). Besides, the D_{pore} for AC and g-C_3N_4/PAC composites were less than 2 nm; thus, AC and the synthesized catalysts were of microporous structure. The D_{pore} for g-C_3N_4 was 25.3242 nm which indicates it was of mesoporous structure.

The value of S_{BET}, V_{tot} and D_{pore} decreased gradually with the increasing weight percentage of g-C_3N_4 in g-C_3N_4/PAC composites. The reduction in S_{BET}, V_{tot} and D_{pore} were attributed to the blockage of the g-C_3N_4 at the microporous structure of AC. The g-C_3N_4 was supported onto the AC surface and thus, the porous structure of the AC decreased. Surprisingly, the D_{pore} for 60 wt% g-C_3N_4/PAC composite were higher than that of 20 wt% g-C_3N_4/PAC composite and 40 wt% g-C_3N_4/PAC composite. This could be attributed to the serious oxidation occurred at 20 wt% g-C_3N_4/PAC composite and 40 wt% g-C_3N_4/PAC composite during pyrolysis process. In other words, the introduction of the surface oxygen group to the 20 wt% g-C_3N_4/PAC composite and 40 wt% g-C_3N_4/PAC composite caused the disordered and blockage of the microporous structure of the composite (Berenguer and Morallon, 2019). The oxidation of 20 wt% g-C_3N_4/PAC composite and 40 wt% g-C_3N_4/PAC composite was further confirmed by EDX analysis as shown in Table 4.2. The complete BET analysis report for the synthesized catalysts is attached in Appendix A.

Table 4.1: BET Specific Surface Area (S_{BET}), Pore Volume (V_{tot}) and Pore Size (D_{pore}) of the Synthesized Catalyst.

Catalyst	**S_{BET} (m^2/g)**	**V_{tot} (cm^3/g)**	**D_{pore} (nm)**
AC	1144.7041	0.5675	1.9831
g-C_3N_4	74.7993	0.4736	25.3242
20 wt% g-C_3N_4/PAC	1124.4379	0.5542	1.9716
40 wt% g-C_3N_4/PAC	995.1877	0.4812	1.9343
60 wt% g-C_3N_4/PAC	996.4360	0.4927	1.9777

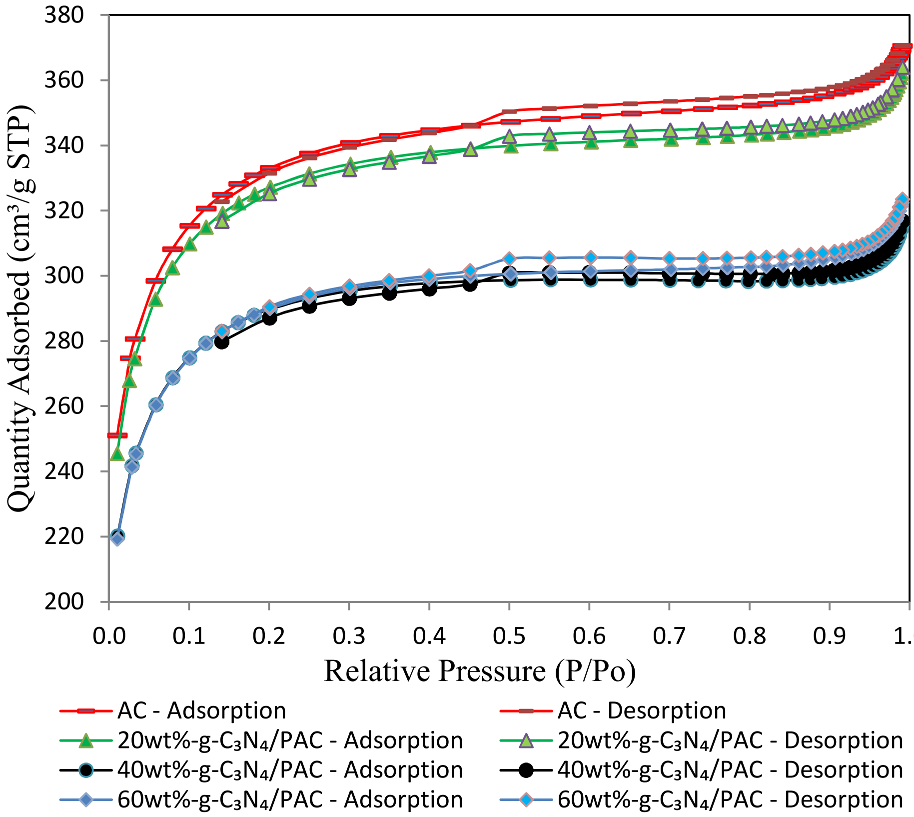

Figure 4.1: N_2 Adsorption-Desorption Isotherms for AC and g-C_3N_4/PAC Composites.

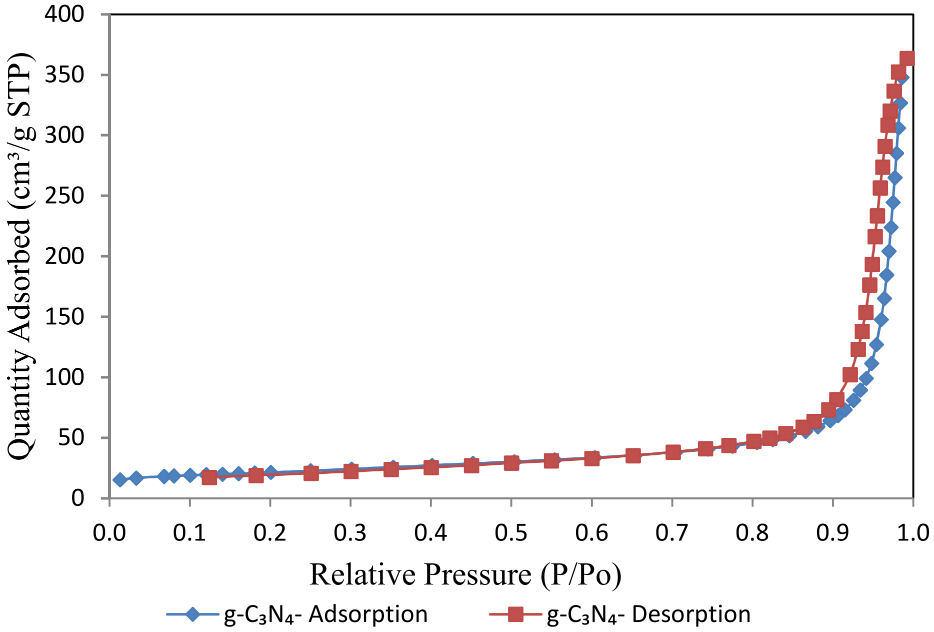

Figure 4.2: N_2 Adsorption-Desorption Isotherms for pure g-C_3N_4.

4.2 Fourier Transform Infrared (FTIR) Spectroscopy

Figure 4.3 and Figure 4.4 show the FTIR plot for the synthesized catalysts and the spent catalysts respectively.

In Figure 4.3, the FTIR spectra of the pure g-C_3N_4 showed a small and sharp peak located at 807 cm^{-1}. The sharp peak was arisen due to the triazine ring breathing vibration or represented as the alkynes C-H bond (Yan, Li and Zou, 2009). Meanwhile, the small peak at 890 cm^{-1} was attributed to the deformation of cross-linked heptazine (Foy at al., 2009; Martin-Ramos et al., 2015; Martin-Ramos et al., 2011). Moreover, the stretches occurred at 1232 cm^{-1}, 1314 cm^{-1}, 1400 cm^{-1}, 1458 cm^{-1} and 1560 cm^{-1} were attributed to the aromatic C-N bonding (Chen at al., 2014; Xiang, Yu and Jaroniec, 2011). The peak at 1629 cm^{-1} was correspondent to the C=N stretching vibration mode (Lv et al., 2017). Besides, FTIR spectra showed the C=O and C=C bonding at around 1629 – 1790 cm^{-1}. The broad peak that centred at 3172 cm^{-1} was counted as the stretching mode of the N-H bond.

Furthermore, the FTIR spectra of the g-C_3N_4/PAC composites shows a similar characteristic band as the pure g-C_3N_4 in which the C-N and C=N bonds were observed at around 1300 – 1560 cm^{-1}. The detection of the characteristic peaks which are C-N and C=N bonds were identified in the g-C_3N_4/PAC composites and thus; the g-C_3N_4 was said to be successfully supported on the AC.

The FTIR spectra of the spent catalysts (Figure 4.4) shows that the characteristic peaks of the g-C_3N_4 and g-C_3N_4/PAC composites remained unchanged after adsorption. However, there is a small peak observed at around 2343 – 23463 cm^{-1} which it represented the presence of O=C=O (carbon dioxide). The presence of CO_2 in the FTIR spectra of the spent catalysts indicated that the organic compounds in the chicken processing wastewater were oxidized and formed CO_2 (Diarmand-Khalilabad et al., 2019). The occurrence of the small peak at around 1040 cm^{-1} was attributed to the presence of the ortho-phosphate group (PO_4^{3-}). This indicates that the orthophosphate in the chicken processing wastewater was successfully adsorbed onto the surface of the catalysts. The complete FTIR analysis report for the synthesized catalysts is attached in Appendix B.

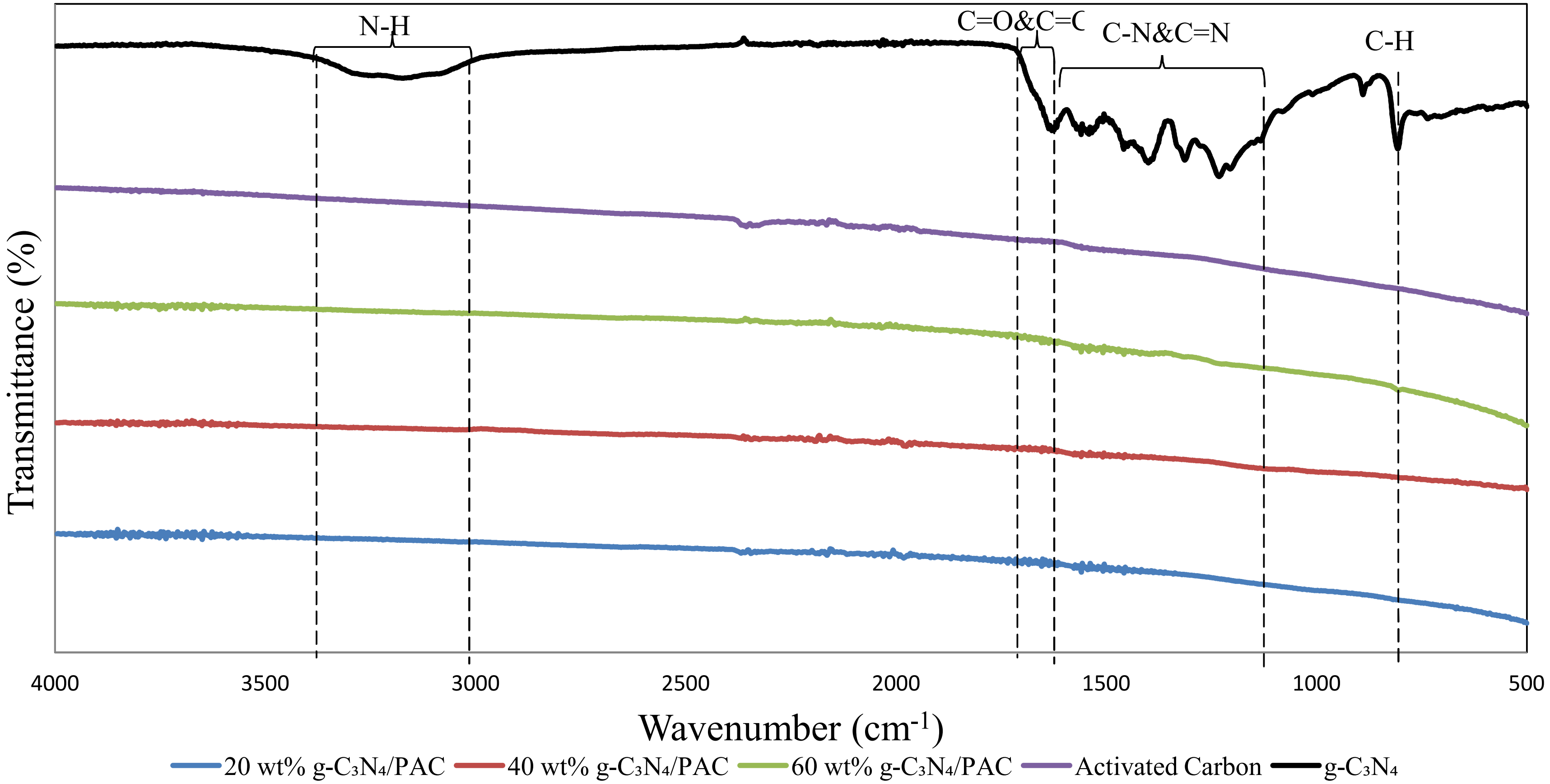

Figure 4.3: FTIR spectra of AC, pure g-C_3N_4 and g-C_3N_4/PAC Composites.

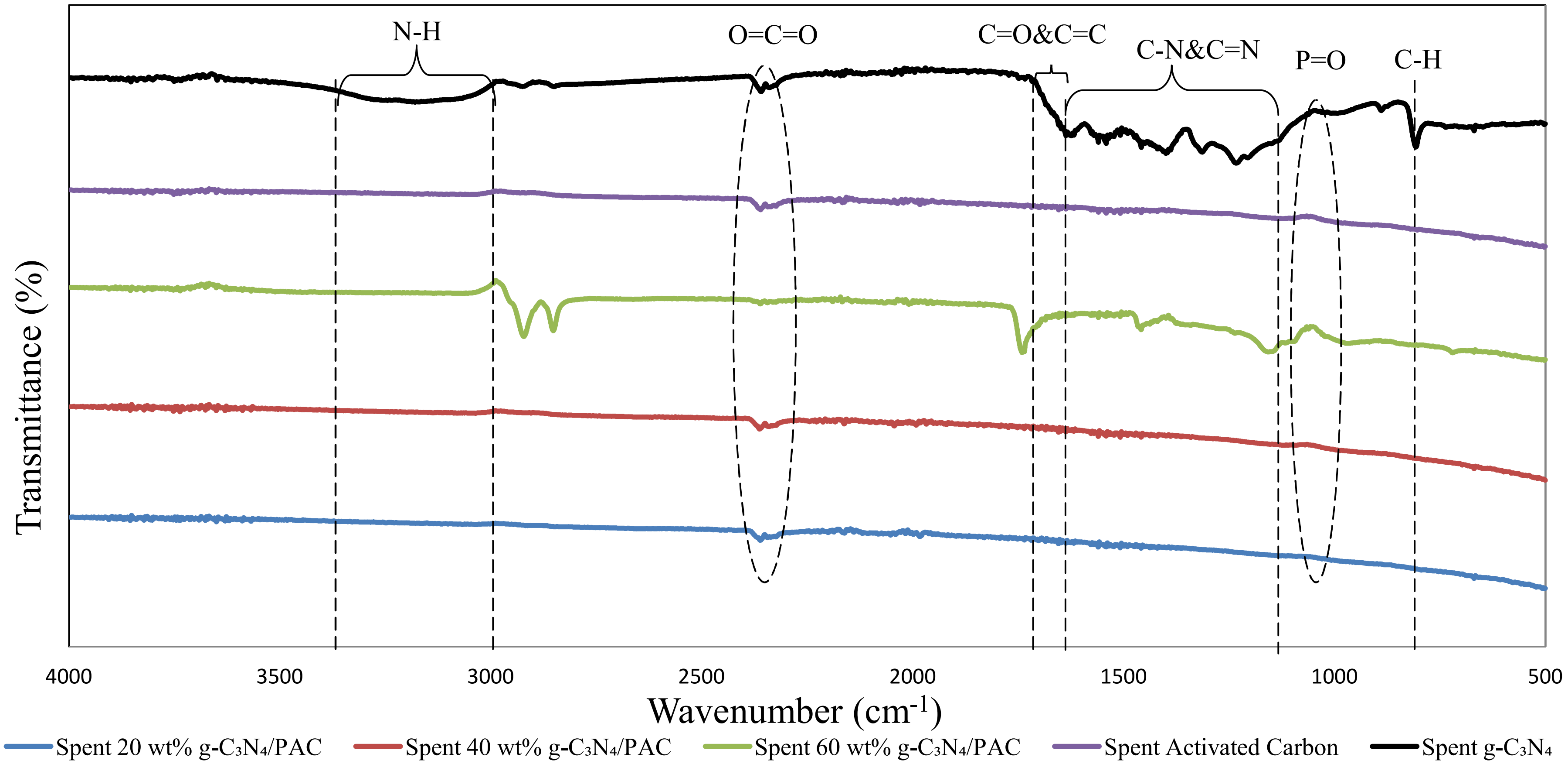

Figure 4.4: FTIR spectra of Spent AC, Spent g-C_3N_4 and Spent g-C_3N_4/PAC Composites.

4.3 X-ray Diffraction (XRD)

The crystallite structure of the AC, pure g-C_3N_4 and g-C_3N_4/PAC composites is shown in Figure 4.5. It was observed that the pure g-C_3N_4 had the characteristic peaks at around 12.9 ^{o} and 27.3 ^{o}. A weak peak at $2\theta = 12.9$ ^{o} with the interplanar spacing of 0.688 nm was attributed to the (1 0 0) plane structural packing motif of tri-s-triazine units. Meanwhile, a strong and sharp peak at $2\theta = 27.3$ ^{o} with the interplanar spacing of 0.326 nm revealed the presence of (0 0 2) lattice plane of the stacking graphitic aromatic (C-N) compounds (Guo et al., 2003; Zhang et al., 2013). The extent of the graphitization could be determined by the sharpness of the (0 0 2) interlayer-stacking peak. It indicates that the carbon nitride was exhibited in a more graphitic nature as compared to the normal polymer-based carbon (Kim, Hwang and Yu, 2007).

There was no change in the major diffraction peak for the g-C_3N_4/PAC composites. However, the minor diffraction peak was shifted from 12.9 ^{o} to around 17.4 ^{o} and it was noticeable that the intensity was slightly reduced for the lower weight percentage of g-C_3N_4/PAC composite. The reduction in peak intensity implied that the reduction of crystallization and polymerization of g-C_3N_4/PAC composite (Fang, et al., 2015).

Moreover, the XRD pattern shows the AC had two characteristic peaks at around $2\theta = 24.9$ ^{o} and 44.1 ^{o}. This reveals the existence of graphitic structure which corresponded to the (0 0 2) and (1 0 0) planes respectively (Rajendran et al., 2015; Omri and Benzina, 2012).

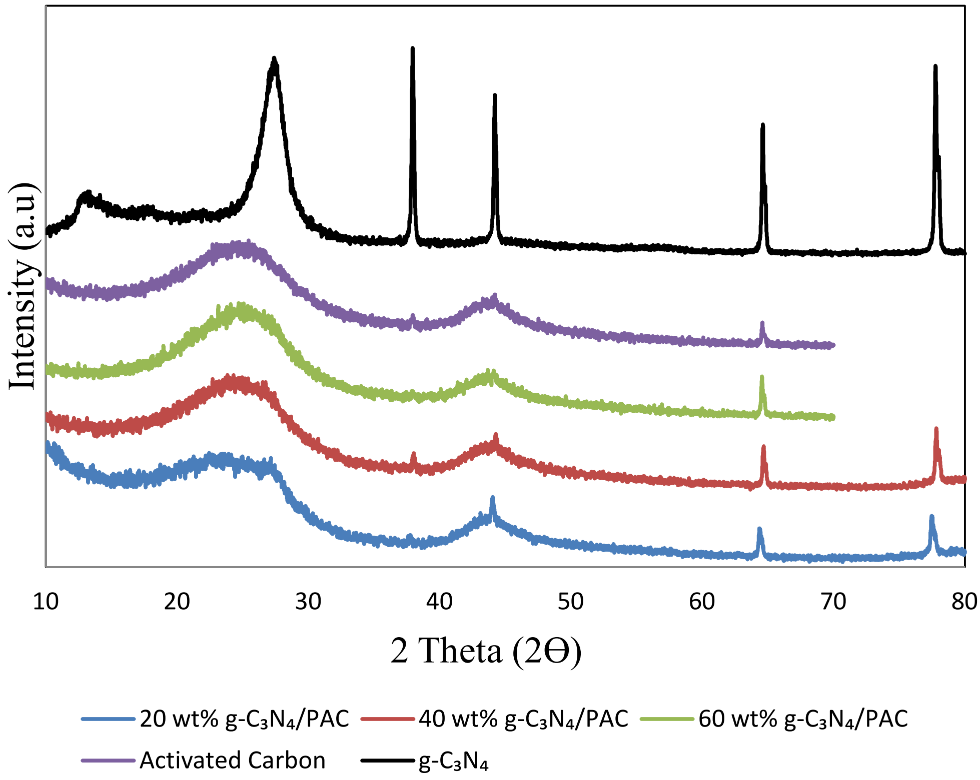

Figure 4.5: XRD Pattern of AC, Pure g-C_3N_4 and g-C_3N_4/PAC Composites.

4.4 Scanning Electron Microscopy (SEM)

Figure 4.6 (a)–(c) show the SEM image of pure g-C_3N_4 in the magnification of 500X, 2000X and 10000X respectively. Based on the Figure 4.6 (a)-(c), it can be seen that the pure g-C_3N_4 particles had a wrinkled surface with an average particle size of 1-3 µm. However, it was agglomerated and displayed in an irregular lamellar structure. Figure 4.6 (a)-(c) also shows that the g-C_3N_4 had a large pore size and this was supported by BET analysis which the D_{pore} of g-C_3N_4 was 25.3242 nm (mesoporous structure).

Figure 4.6 (d)-(f) show the SEM image of AC in the magnification of 2000X, 8000X and 30000X. It can be seen that the AC had a rougher surface texture and a larger particle size was observed from the Figure 4.6 (d)-(f). Activated carbon seems to have a larger surface area as compared to that of g-C_3N_4 and this was supported by BET analysis which AC had a larger S_{BET} (1144.7041 m^2/g) as compared to that of g-C_3N_4 (74.7993 m^2/g). The SEM image of AC in Figure 4.6 (d)-(f) show that it had microporous structure and this was confirmed by BET analysis which it had the pore size of 1.9831 nm.

Figure 4.6 (g)-(o) show the SEM image of different weight percentage of g-C_3N_4/PAC composites in the magnification of 2000X, 6500X and 8000X. In contrast, the surface texture of the g-C_3N_4/PAC composites was rougher as compared to that of pure g-C_3N_4. Besides, the AC acts as support catalyst to provide a larger surface area to g-C_3N_4/PAC composites. This statement was supported by the larger S_{BET} was found on g-C_3N_4/PAC composites as compared to the pure g-C_3N_4 (74.7993 m^2/g). Thus, AC could prevent the self-aggregation of g-C_3N_4 while provided a larger surface area to reduce the particle size distribution of g-C_3N_4 as well.

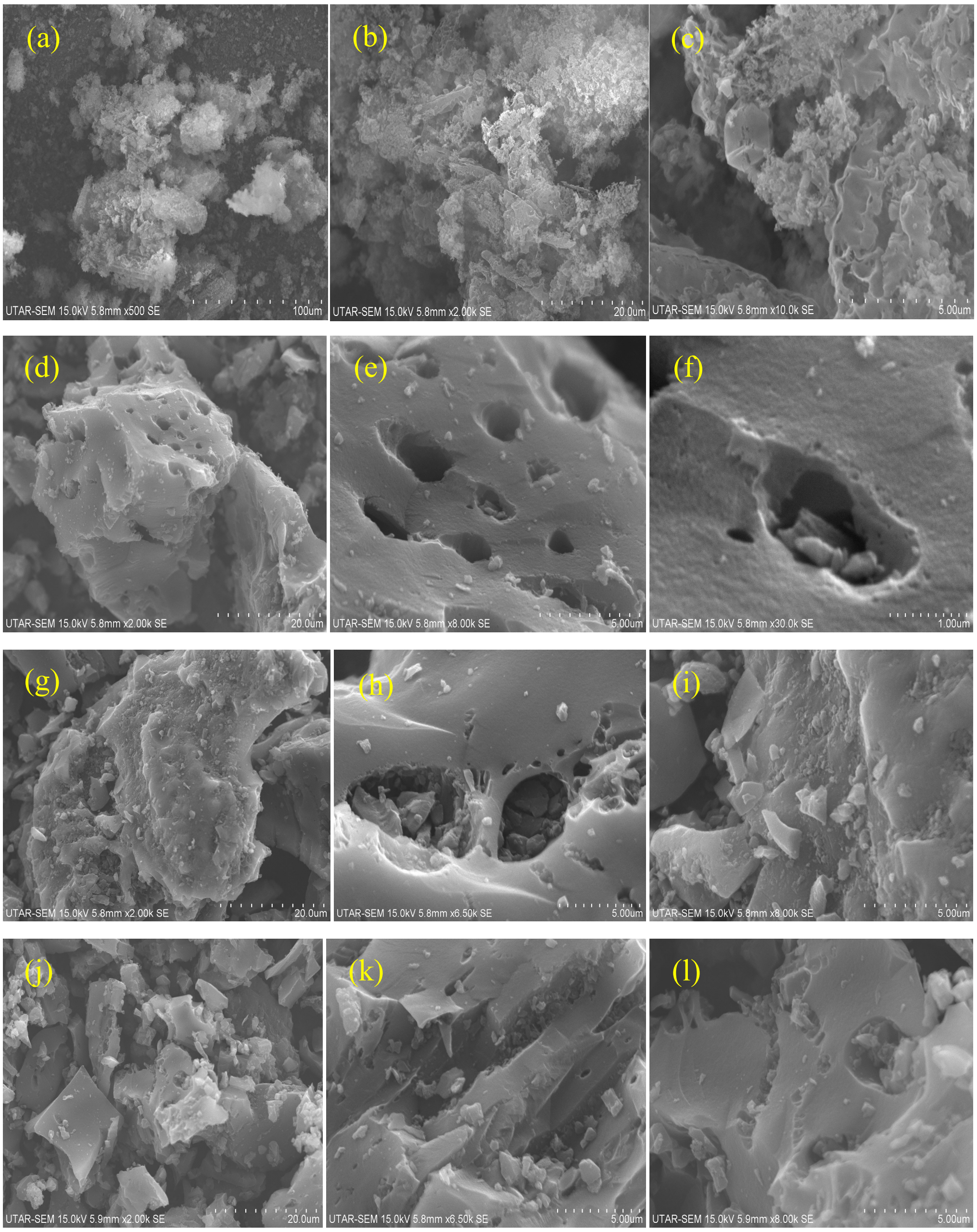

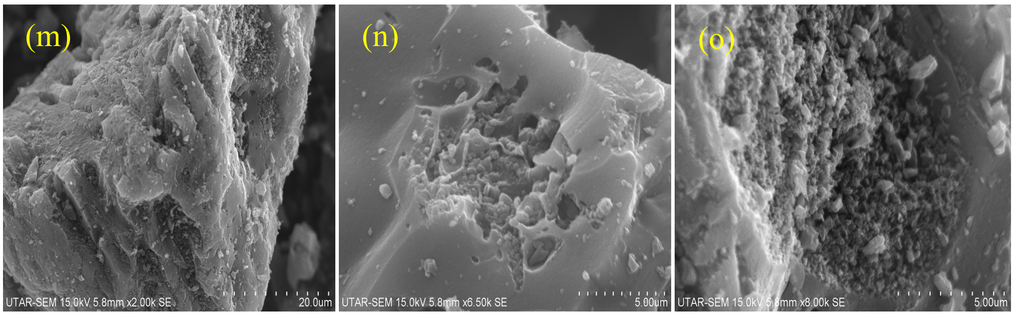

Figure 4.6: SEM Image of (a) Pure g-C_3N_4 (500X) (b) Pure g-C_3N_4 (2000X) (c) Pure g-C_3N_4 (10000X) (d) AC (2000X) (e) AC (8000X) (f) AC (30000X) (g) 20 wt% g-C_3N_4/PAC (2000X) (h) 20 wt% g-C_3N_4/PAC (6500X) (i) 20 wt% g-C_3N_4/PAC (8000X) (j) 40 wt% g-C_3N_4/PAC (2000X) (k) 40 wt% g-C_3N_4/PAC (6500X) (l) 40 wt% g-C_3N_4/PAC (8000X) (m) 60 wt% g-C_3N_4/PAC (2000X) (n) 60 wt% g-C_3N_4/PAC (6500X) (o) 60 wt% g-C_3N_4/PAC (8000X)

4.5 Energy Dispersive X-ray (EDX)

Table 4.2 shows the presence of carbon (C), nitrogen (N) and oxygen (O) element in pure g-C_3N_4. The C and N elements were originated from g-C_3N_4; whereas, there was a detection of O element due to the oxidation of urea during pyrolysis in a muffle furnace. Meanwhile, the same elements which are C, N and O were detected in g-C_3N_4/PAC composites as well. However, there was just a small percentage of N element was detected in the composites due to the low yield rate of urea to g-C_3N_4. The N element increased with the increasing of weight percentage of g-C_3N_4 in the composite. In addition, there was only C and O elements were detected in the AC. The complete EDX analysis report for the synthesized catalysts is attached in Appendix C.

Table 4.2: Elemental Composition of the Synthesized Catalysts.

Catalyst	**Elemental Composition (At. %)**		
	C	**N**	**O**
AC	96.72	-	3.28
Pure g-C_3N_4	62.21	32.70	5.09
20 wt% g-C_3N_4/PAC	91.17	1.01	7.81
40 wt% g-C_3N_4/PAC	90.47	1.25	8.29
60 wt% g-C_3N_4/PAC	95.02	2.35	2.63

4.6 Adsorption-Photocatalytic Degradation of Chicken Processing Wastewater

Table 4.3 shows the performance of the synthesized catalysts for chicken processing wastewater treatment under the dark adsorption and photocatalytic degradadtion. There are three main parameters to be tested in this project which are COD, orthophosphate and ammonia nitrogen.

Table 4.3: Performance of various catalyst in chicken processing wastewater treatment.

Type of Experiment	S_{BET} (m^2/g)	Type of Catalyst	Parameter	Removal Efficiency (%)
Adsorption in dark	1144.7041	AC	COD	79.00
			Orthophosphate	28.30
			Ammonia Nitrogen	50.00
	74.7993	Pure g-C_3N_4	COD	34.50
			Orthophosphate	49.10
			Ammonia Nitrogen	100
	1124.4379	20 wt% g-C_3N_4/PAC	COD	25.30
			Orthophosphate	10.70
			Ammonia Nitrogen	34.60
	995.1877	40 wt% g-C_3N_4/PAC	COD	62.10
			Orthophosphate	27.90
			Ammonia Nitrogen	60.00
	996.4360	60 wt% g-C_3N_4/PAC	COD	66.90
			Orthophosphate	15.40
			Ammonia Nitrogen	29.20

Table 4.3: Continued.

Type of Experiment	Type of Catalyst	Parameter	Removal Efficiency (%)
Photodegradation under irradiation of LED light	AC	COD	11.90
		Orthophosphate	13.90
		Ammonia Nitrogen	40.00
	Pure g-C_3N_4	COD	40.60
		Orthophosphate	49.00
		Ammonia Nitrogen	-
	20 wt% g-C_3N_4/PAC	COD	47.00
		Orthophosphate	12.00
		Ammonia Nitrogen	34.00
	40 wt% g-C_3N_4/PAC	COD	13.40
		Orthophosphate	16.10
		Ammonia Nitrogen	12.50
	60 wt% g-C_3N_4/PAC	COD	31.30
		Orthophosphate	7.60
		Ammonia Nitrogen	52.90

Table 4.3: Continued.

Type of Experiment	Type of Catalyst	Parameter	Removal Efficiency (%)
Photodegradation under irradiation of LED light	Blank	COD	0.10
		Orthophosphate	1.10
		Ammonia Nitrogen	5.30

4.6.1 COD Removal

Figure 4.7 – Figure 4.9 show the COD removal efficiency in the dark adsorption and photodegradation under irradiation of LED light. Table 4.3 shows that AC had the best COD removal efficiency in the dark adsorption. Since, the definition of COD is the measurement of oxygen required to oxidize the soluble organic matter in a solution. Thus, it was claimed that AC can remove up to 79 % of organic compounds in the chicken processing wastewater.

The achievement of the highest COD removal efficiency by AC in the dark adsorption was attributed to its highest specific surface area (1144.7041 m^2/g) which adsorbed more organic compounds onto its surface. The high specific surface area provided by AC enhanced adsorption capacity of COD on g-C_3N_4/PAC composites (Sanou et al., 2015). Overall, the COD removal efficiency of the synthesized catalyst in dark adsorption follows the sequence of AC (79.00 %) > 60 wt% g-C_3N_4/PAC (66.90 %) > 40 wt% g-C_3N_4/PAC (62.10 %) > pure g-C_3N_4 (34.50 %) > 20 wt% g-C_3N_4/PAC (25.30 %).

Both of 60 wt% g-C_3N_4/PAC and 40 wt% g-C_3N_4/PAC had a better COD removal performance than that of pure g-C_3N_4 in dark adsorption because they possess higher specific surface area compared to other catalysts. Thus, more organic compounds can be adsorbed onto the surface of the composites. In comparison with 40 wt% g-C_3N_4/PAC, 60 wt% g-C_3N_4/PAC exhibited a higher COD removal efficiency owing to its larger pore diameter (1.9777 nm) which could adsorb more organic compounds towards its micropores. However, 20 wt% g-C_3N_4/PAC composite showed the lowest COD removal efficiency in the dark adsorption due to the lattice deformation of C_3N_4 (Benesi, 1957).

The COD removal efficiency by photocatalytic degradation follows the trend of 20 wt% g-C_3N_4/PAC (47.00 %) > pure g-C_3N_4 (40.60 %) > 60 wt% g-C_3N_4/PAC (31.30 %) > 40 wt% g-C_3N_4/PAC (13.40 %) > AC (11.90 %) > blank sample (0.10 %). It was noticeable that the pure g-C_3N_4 possesses greater removal efficiency (40.60 %) by photodegradation under irradiation of the LED light than that of AC (11.90 %). This was attributed to the narrow band gap of the pure g-C_3N_4 (2.7 eV) which helped to adsorb more visible light (Kumar, Karthikeyan and Lee, 2018). When the pure g-C_3N_4 is exposed to the LED light, a hole (h^+) and an electron hole (e^-) could be created; a chain of oxidation and reduction processes will then take place on the surface of the photo-excited g-C_3N_4. Moreover, the photocatalytic performance of 60 wt% g-C_3N_4/PAC (31.30 %) and 40 wt% g-C_3N_4/PAC (13.40 %) were poorer than that of 20 wt% g-C_3N_4/PAC (47.00 %) because 60 wt% g-C_3N_4/PAC and 40 wt% g-C_3N_4/PAC composites had lower surface area caused by the blockage of higher loading of g-C_3N_4. This was consistent with BET surface area results.

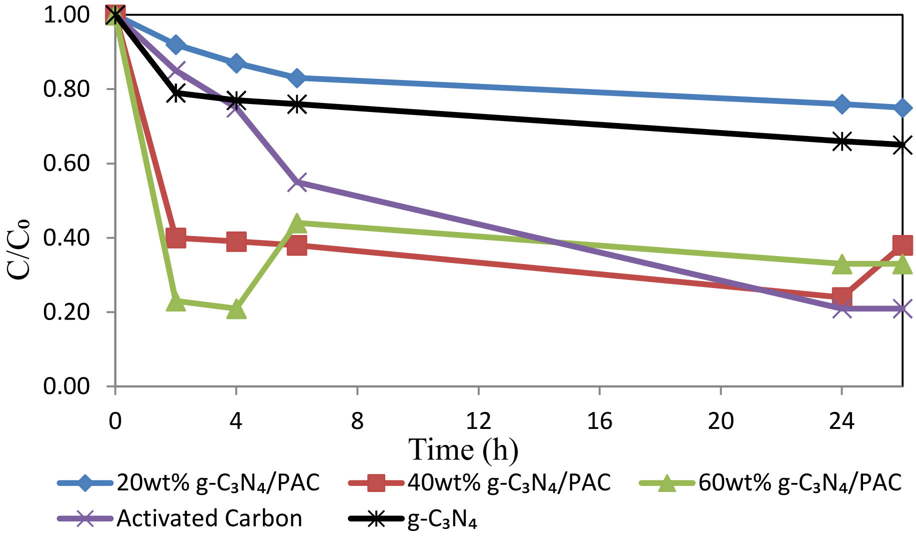

Figure 4.7: COD Removal in the Dark Adsorption.

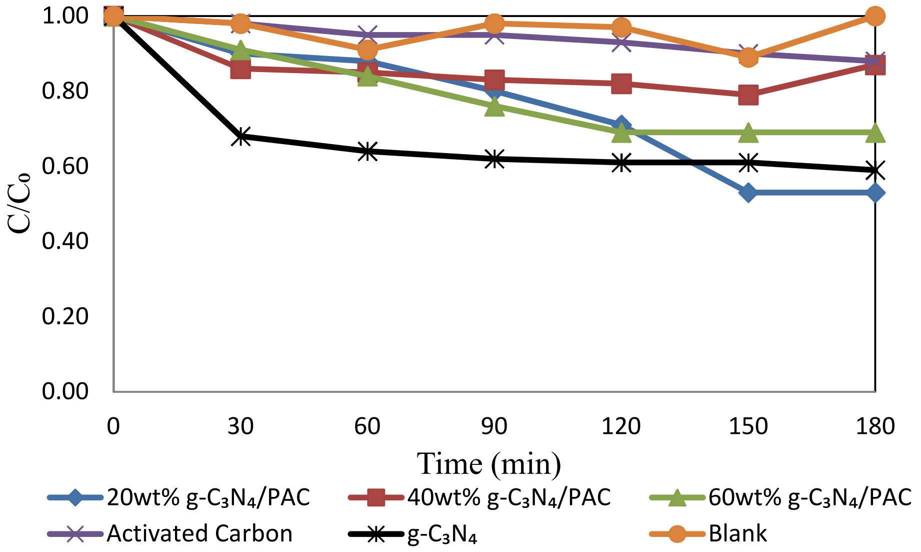

Figure 4.8: COD Removal by Photocatalytic Degradation Under Irradiation of LED Light.

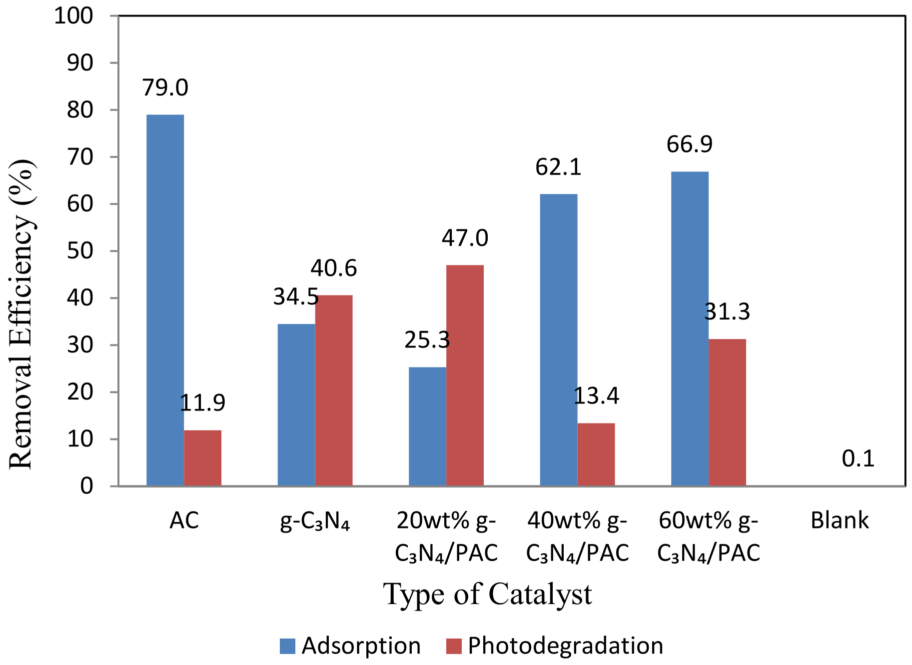

Figure 4.9: Comparison Chart of COD Removal Efficiency by Adsorption and Photocatalytic Degradation.

4.6.2 Orthophosphate Removal

As shown in Figure 4.10 - Figure 4.12, the orthophosphate removal efficiency by dark adsorption follows the sequence of pure g-C_3N_4 (49.10 %) > AC (28.30 %) > 40 wt% g-C_3N_4/PAC (27.90 %) > 60 wt% g-C_3N_4/PAC (15.40 %) > 20 wt% g-C_3N_4/PAC (10.70 %). Meanwhile, the orthophosphate removal efficiency by photocatalytic degradation follows the sequence of pure g-C_3N_4 (49.00 %) > 40 wt% g-C_3N_4/PAC (16.10 %) > AC (13.90 %) > 20 wt% g-C_3N_4/PAC (12.00 %) > 60 wt% g-C_3N_4/PAC (7.60 %) > Blank (1.10 %). These results show that the pure g-C_3N_4 reached the highest orthophosphate removal efficiency in the dark adsorption (49.10 %) and photodegradation (49.00 %) compared to other catalysts. The reason for the pure g-C_3N_4 to achieve the highest orthophosphate removal efficiency was attributed to the electrostatic attraction between the negatively charge orthophosphate ion and the positively charged N-H functional group on the pure g-C_3N_4 surface (Kumar et al., 2019). The existence of the positively charged functional group on the pure g-C_3N_4 surface was supported by the detection of N-H functional group in the FTIR spectrum in Figure 4.3. Moreover, a larger pore size which bigger than 10 nm was required in order to increase the adsorption rate of orthophosphate (Kumar et al., 2019; Zhang, 2019). The D_{pore} of the pure g-C_3N_4 was 25.3242 nm in BET analysis in which it favoured the adsorption of orthophosphate group as its pore size is larger than 10 nm.

Meanwhile, AC can only remove 28.30 % of orthophosphate in the dark adsorption because it had a smaller D_{pore} (1.9831 nm) which was not favourable for the adsorption of orthophosphate onto its microporous structure. Activated carbon is not suitable for the adsorption of orthophosphate and the similar observation was reported as the pore size of AC was too small for the orthophosphate to be adsorbed onto its micropore (Kumar et al., 2019; Zhang, 2019). Besides, the blank sample without the presence of catalyst was self-degraded for 1.10 % of orthophosphate. In other words, the orthophosphate in the chicken processing wastewater will be photodegradaded under the irradiation of LED light without the existence of any catalysts.

It was noticeable that the g-C_3N_4/PAC composites did not show improvement in the dark adsorption of orthophosphate, although the incorporation of AC enhanced the specific surface area of g-C_3N_4. Activated carbon was found to be of zero point charge since there was no functional group detected in the FTIR spectrum and this will further reduced the electrostatic attraction between the negatively charge orthophosphate ion and the positively charged functional group on the g-C_3N_4/PAC composites surface. The more electronegative oxygen surface group was introduced to the g-C_3N_4/PAC composites due to the oxidation during pyrolysis process and this was confirmed by EDX analysis. Thus, this will create electrostatic repulsion between the negatively charge orthophosphate ion and the electronegative oxygen surface group (Dorland, 2020). The average pore size of the g-C_3N_4/PAC composites were smaller than 2 nm which are of microporous structure and thus, the pore size of the g-C_3N_4/PAC composites were not large enough to allow the adsorption of orthophosphate group and lead to the failure in the enhancement of photocatalytic performance.

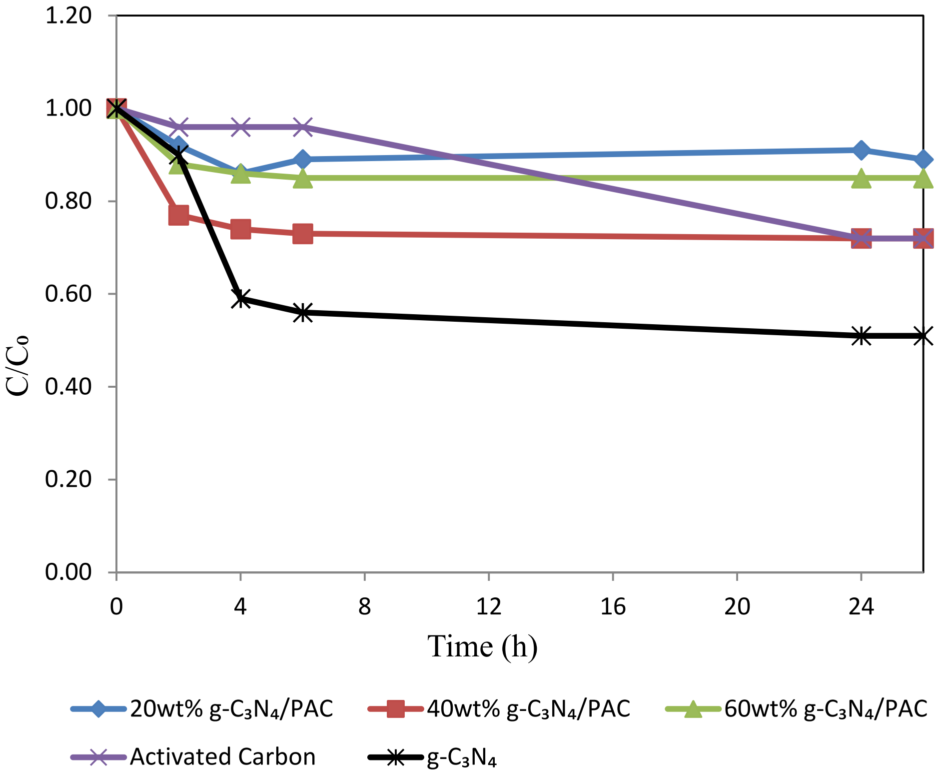

Figure 4.10: Orthophosphate Removal in the Dark Adsorption.

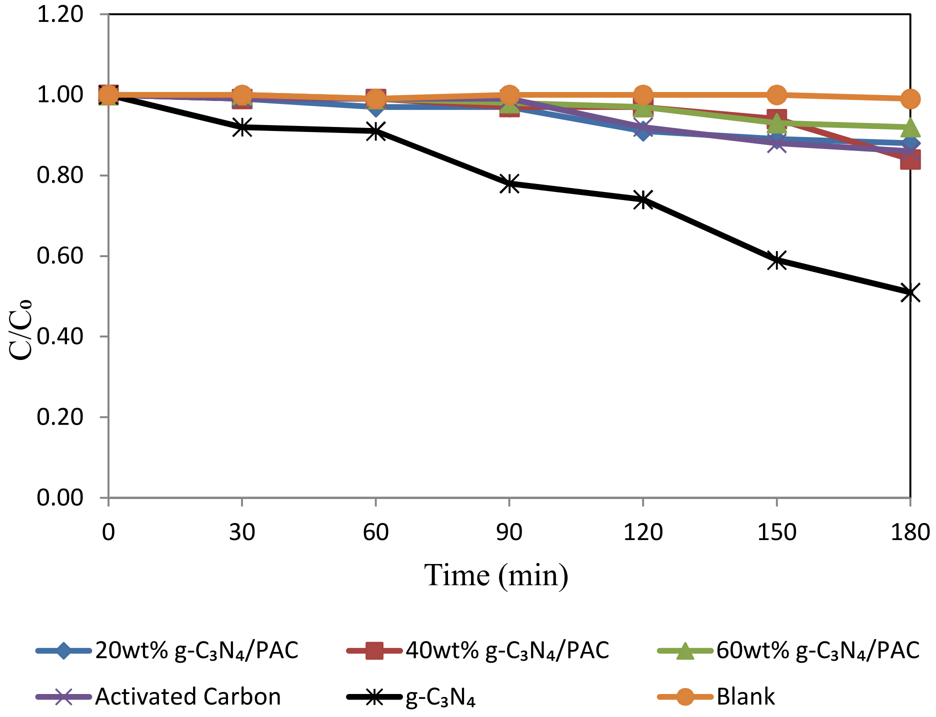

Figure 4.11: Orthophosphate Removal by Photocatalytic Degradation Under Irradiation of LED Light.

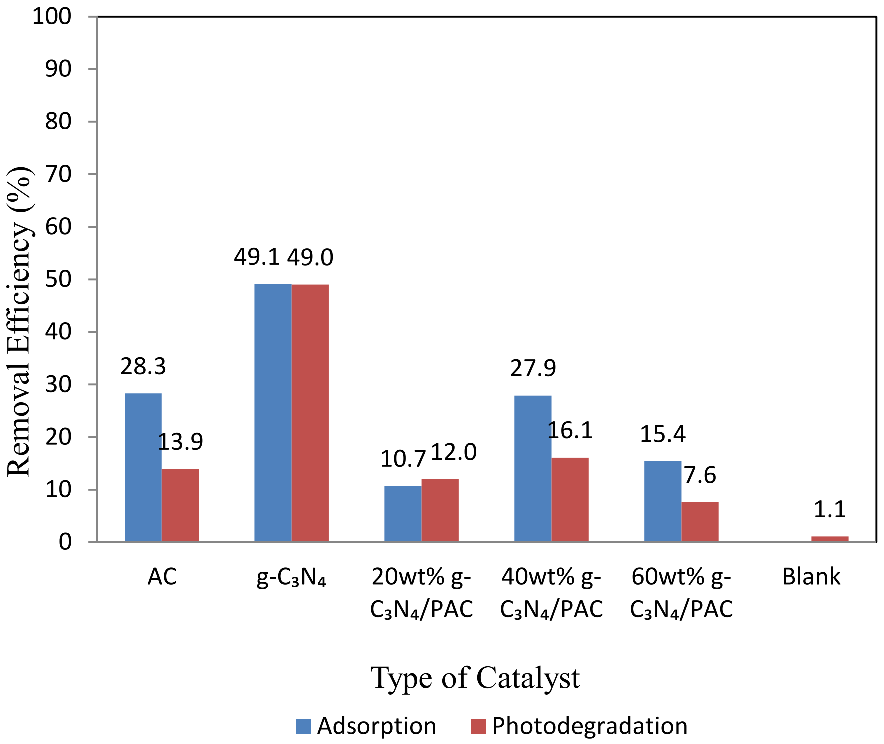

Figure 4.12: Comparison Chart of Orthophosphate Removal Efficiency by Adsorption and Photocatalytic Degradation.

4.6.3 Ammonia Nitrogen Removal

As shown in Figure 4.13 – Figure 4.15, the ammonia nitrogen removal efficiency by dark adsorption follows the sequence of pure g-C_3N_4 (100 %) > 40 wt% g-C_3N_4/PAC (60.00 %) > AC (50.00 %) > 20 wt% g-C_3N_4/PAC (34.60 %) > 60 wt% g-C_3N_4/PAC (29.20 %). Table 4.3 shows that the pure g-C_3N_4 can remove up to 100 % of ammonia nitrogen in the dark adsorption. This was attributed to the electrostatic attraction between the positively ammonium ions (NH_4^+) and the negatively charged C=O and C-O functional group that were detected in FTIR spectrum (Figure 4.3).

Meanwhile, AC can only remove 50.00 % of ammonia nitrogen in the dark adsorption because of it had a smaller D_{pore} (1.9831 nm) which the ammonia nitrogen was found in difficulty to be adsorbed onto its microporous structure.

Among all the synthesized catalysts, 40 wt% g-C_3N_4/PAC composite showed the highest ammonia nitrogen removal efficiency (60.00 %) in the dark adsorption. This was attributed to the highest electronegative oxygen surface group (8.29 %) as shown in the EDX analysis (Table 4.2) was found due to oxidation during pyrolysis process and therefore, electrostatic attraction was occurred between the positively ammonium ions (NH_4^+) and the electronegative oxygen surface group. In other words, the ammonia nitrogen removal efficiency can be improved with increasing of the electronegative oxygen surface group.

For the photocatalytic degradation results (Figure 4.14), 60 wt% g-C_3N_4/PAC composite showed the highest ammonia nitrogen removal efficiency (52.90 %), followed by AC (40.00 %), 20 wt% g-C_3N_4/PAC (34.00 %), 40 wt% g-C_3N_4/PAC (12.50 %) and blank sample (5.30 %). Furthermore, the mechanism of photodegradation had been discussed in Chapter 2 which a chain of oxidative and reductive reactions occurred on the surface of the synthesized catalysts at same instant. Thus, the higher weight percentage of g-C_3N_4, the better the photodegradation performance as more ammonia nitrogen compound was attracted to the active sites of g-C_3N_4 which will be further degraded by photocatalysis.

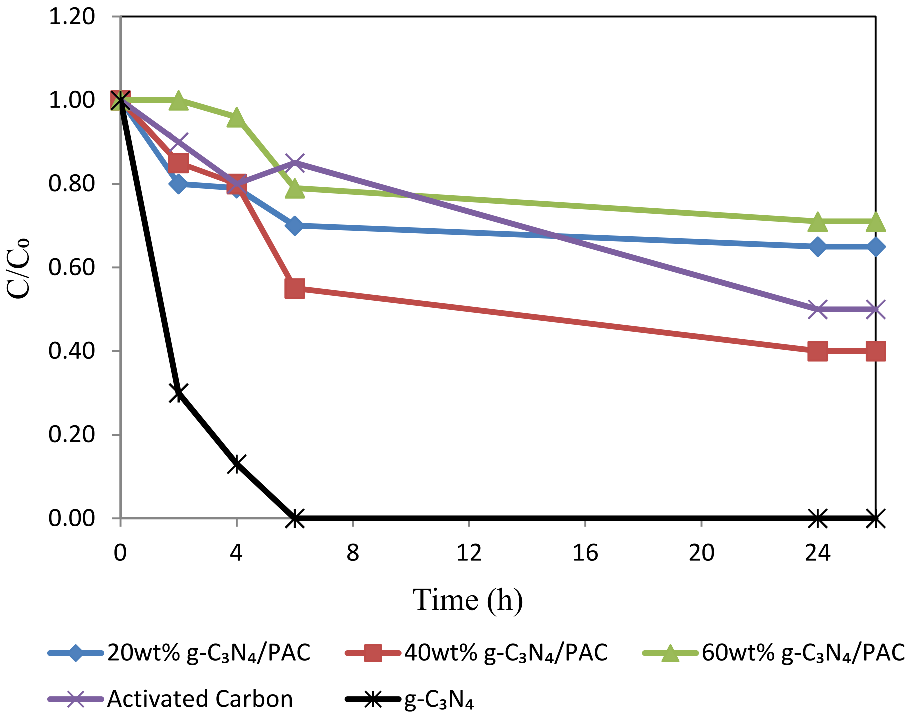

Figure 4.13: Ammonia Nitrogen Removal in the Dark Adsorption.

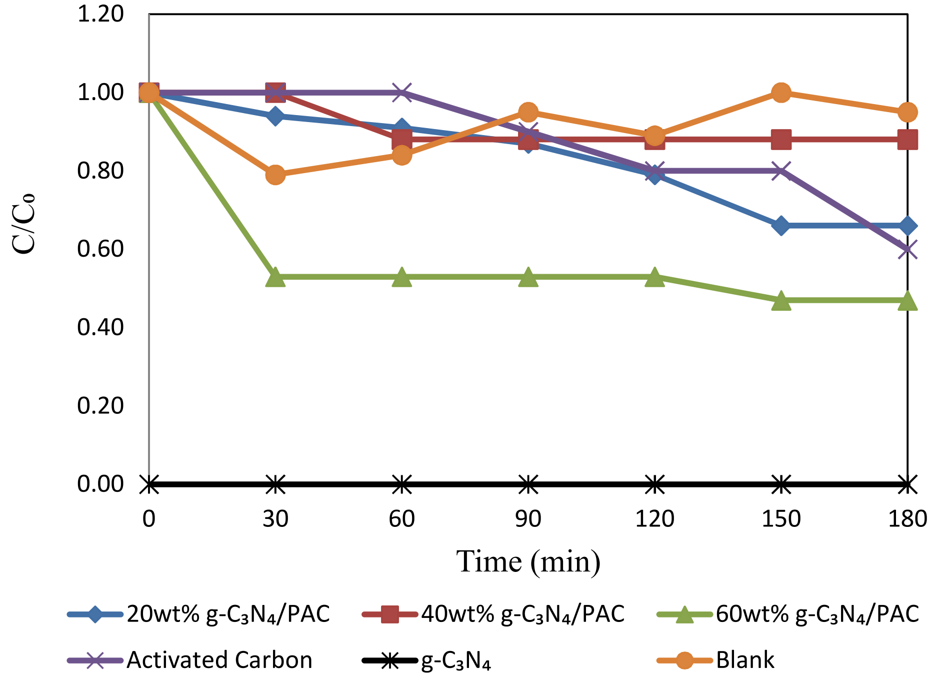

Figure 4.14: Ammonia Nitrogen Removal by Photocatalytic Degradation Under Irradiation of LED Light.

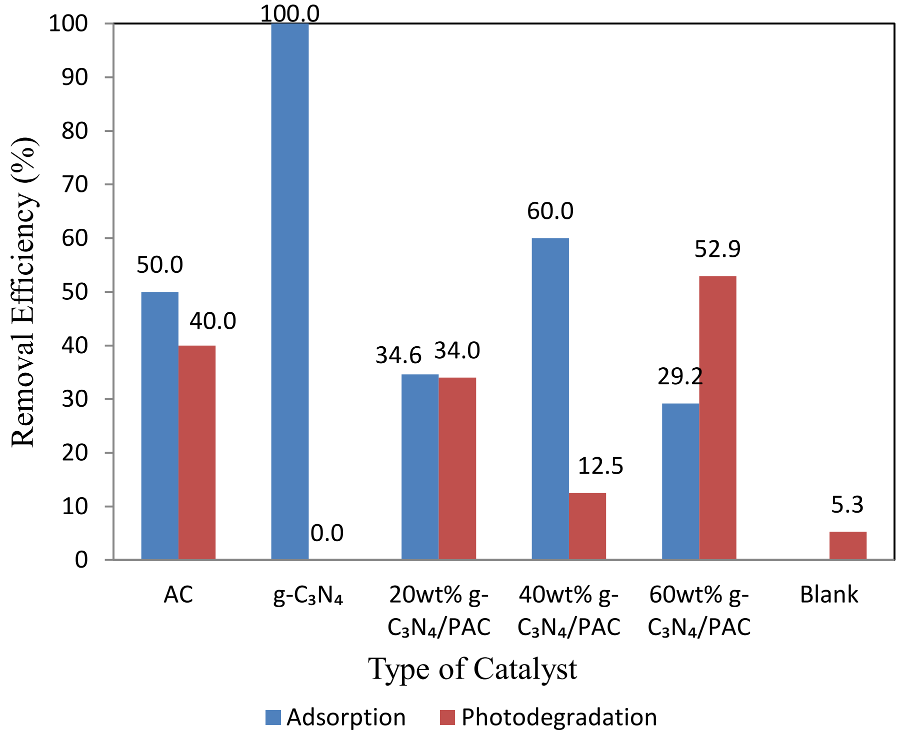

Figure 4.15: Comparison Chart of Ammonia Nitrogen Removal Efficiency by Adsorption and Photocatalytic Degradation.

CHAPTER 5

CONCLUSIONS AND RECOMMENDATIONS

5.1 Conclusions

The g-C_3N_4 was successfully supported on the AC surface by pyrolyzing the urea and activated carbon mixture. This is proven with the presence of N element which was analyzed by EDX. However, the O element presents in the EDX analysis indicated that the synthesized catalysts were oxidized. The BET analysis showed that the incorporation of AC into the 20 wt% g-C_3N_4/PAC, 40 wt% g-C_3N_4/PAC and 60 wt% g-C_3N_4/PAC composites had enhanced the S_{BET} of the g-C_3N_4 (from 74.7993 m^2/g to 1124.4379 m^2/g, 995.1877 m^2/g and 996.4360 m^2/g respectively). The SEM image of all g-C_3N_4/PAC composites showed that the AC had reduced the agglomeration of g-C_3N_4 by providing a larger surface area and thus, more active sites were triggered.

The adsorption performance of the synthesized catalysts was evaluated and the AC showed the highest COD removal efficiency (79.00 %) in the dark adsorption; whereas, the pure g-C_3N_4 showed the highest removal efficiency for orthophosphate (49.10 %) and ammonia nitrogen (100 %) in the dark adsorption. This proves that the AC was not suitable to remove orthophosphate and ammonia nitrogen due to its microporous structure.

The photocatalytic degradation of chicken processing wastewater was carried out once the adsorption-desorption equilibrium was reached after 26 h in dark condition. Among the synthesized catalysts, 20 wt% g-C_3N_4/PAC showed the highest COD removal efficiency (47.00 %) by photocatalytic reaction under irradiation of LED light. Meanwhile, the pure g-C_3N_4 achieved the highest orthophosphate removal efficiency (49.00 %) by photocatalytic reaction. 60 wt% g-C_3N_4/PAC showed the highest photocatalytic degradation efficiency (52.90 %) towards the removal of ammonia nitrogen. Overall, the supported of g-C_3N_4 onto the AC surface successfully improved the photocatalytic performance for COD and ammonia nitrogen removal.

5.2 Recommendations for future work

The entire project was conducted in such a way of following the scope of study. Nevertheless, the exploration of the project was limited due to the time constraint. To enhance the future works, the recommendations are given as following:

(i) Different manipulated variables such as temperature, stirred rate, pH, dosage of catalyst and the energy supplied should be varied in order to find out the optimum condition for the adsorption and photocatalytic degradation of chicken processing wastewater.

(ii) The synthesized composites can be prepared at a higher weight percentage of g-C_3N_4 in order to achieve a better photocatalytic performance.

(iii) Different types of model pollutant can be used to test the adsorption-photocatalytic degradation efficiency of the synthesized composites.

(iv) The synthesized composites can be characterized using high-resolution transmission electron microscopy (HRTEM) for a better understanding on its atomic structure.

REFERENCES

Anandan, S., Ikuma, Y. and Niwa, K., 2010. An overview of semi-conductor photocatalysis: modification of TiO_2 nanaomaterials. *Solid State Phenomena*, 162, pp. 239-260.

Artioli, Y., 2008. Adsorption. *Reference Module in Earth Systems and Environmental Sciences*, pp. 60-65.

Asha, R.C. and Kumar, M., 2014. Photocatalytic degradation of poultry wastewater using activated carbon-supported titanium dioxide. *Desalination and Water Treatment*, pp. 3279-3290.

Aurian-Blajeni, B.; Halmann, M. and Manassen, J., 1980. Photoreduction of carbon dioxide and water into formaldehyde and methanol on semiconductor materials. *Solar Energy*, 25, pp. 165–170.

Bai, X., Yan, S., Wang, J., Wang, L., Jiang,W., Wu, S., Sun, C. and Zhu, Y., 2014. A simple and efficient strategy for the synthesis of a chemically tailored g-C_3N_4 material. *Journal of Materials Chemistry*, 2, pp. 17521-17529.

Bansal, R.C., Donnet, J.B. and Stoeckli, H.F., 1988. *Activated Carbon*. Marcel Dekker, New York.

Bayarri, B., Giménez, J., Curcó, D. and Esplugas, S., 2005. Photocatalytic degradation of 2,4-dichlorophenol by TiO_2/UV: Kinetics, actinometries and models. *Catalysis Today*, 101(3–4), pp.227–236.

Benesi, H.A., 1957. Acidity of Catalyst Surfaces. II. Amine Titration Using Hammett Indicators. *Journal of Physical Chemistry*, 61(7), pp. 973-973.

Bensebaa, F., 2012. Nanoparticle Technologies: Chapter 5 – Clean Energy. *Interface Science and Technology*.

Berenguer, R. and Morallon, E., 2019. Oxidation of Different Microporous Carbons by Chemical and Electrochemical Methods. *Frontiers in Materials*.

Boer, K.W., 1990. *Survey of semiconductor physics*. Van Nostrand R., New York, USA.

Brandao, Y.B., de Oliveira, J.G.C. and Benachour, M., 2016. *Phenolic Wastewaters: Definition, Sources and Treatment Processes*. DOI: 10.5772/66366.

Cao, H.B., Xie, Y.B., Lee, Y.P., Xiao, J.D. and Sheng, Y.X., 2015. Graphitic-phase carbon nitride (g-C_3N_4) material and preparation method and application thereof. *Google Patent*. [online] Available through: <https://patents.google.com/patent/CN105126893A/en> [Accessed 26 July 2019]

Cao, S.W. and Yu, J.G., 2014. g-C_3N_4-based photocatalysts for hydrogen generation. *The Journal of Physical Chemistry Letters*, 5(12), pp. 2101-2107.

Chen, X.Y., Kuo, D.H. and Lu, D.F., 2016. Nanonization of g-C_3N_4 with the assistance of activated carbon for improved visible light photocatalysis. *RSC Advances*, 71.

Chen, Y.L., Li, J.H., Hong, Z.H., Shen, B., Lin, B.Z. and Gao, B.F., 2014. Origin of the enhanced visible-light photocatalytic activity of CNT modified g-C_3N_4 for H_2 production. *Physical Chemistry Chemical Physics*, 17.

Chong, M.N., Jin, B., Chow, C.W.K. and Saint, C., 2010. Recent developments in photocatalytic water treatment technology: A review. *Water Research*, 44, pp. 2997-3027.

Chou, H.L., Hwang, B.J. and Sun, C.L., 2013. Catalysis in fuel cells and hydrogen production. *New and Future Developments in Catalysis*, pp. 217-270.

Ciminello, R., 2005. *Activated carbon*. [online] Available through: <https://www.wqpmag.com/activated-carbon> [Accessed 15 August 2019]

Colmenares, J.C. and Luque, R., 2013. Heterogeneous photocatalytic nanomaterials: prospects and challenges in selective transformations of biomass-derived compounds. *Chemical Society Reviews*, 43, pp. 765-778.

Dabrowski, A., 2001. Adsorption – from theory to practice. *Advances in Colloid and Interface Science*, 93, pp. 135-224.

Daud, W.M.A.W., Ali, W.S.W. and Sulaiman, M.Z., 2000. The effects of carbonization temperature on pore development in palm-shell-based activated carbon. *Journal of Carbon*, 38, pp. 1925-1932.

Deng, L., Jiang, L., Tang, Q.W. and Li, H.X., 2018. g-C_3N_4 photocatalysis technology application in water treatment. *IOP Conf. Series: Materials Science and Engineering*, 392.

Deng, Y. and Zhao, R.Z., 2015. Advanced oxidation processes (AOPs) in wastewater treatment. *Current Pollution Reports*, 1(3), pp.167-176.

Deng, Y., 2009. Advanced oxidation processes (AOPs) for reduction of organic pollutants in landfill leachate: a review. *Internation Journal of Environment and Waste Management*, 4(3), pp.84-336.

Diarmand-Khalilabad, H., Habibi-Yangjeh, A., Seifzadeh, D., Asadzadeh-Khaneghah, S. and Vesali-Kermani, E., 2019. g-C_3N_4 nanosheets decorated with carbon dots and CdS nanoparticles: Novel nanocomposites with excellent nitrogen photofixation ability under simulated solar irradiation. *Ceramics International*, 45(2), pp. 2542-2555.

Dorland, 2020. *Dorland's Illustrated Medical Dictionary E-book.*

Dong, F., Sun, Y., Wu, L., Fu, M. and Wu, Z., 2012. Facile transformation of low cost thiourea into nitrogen-rich graphitic carbon nitride nanocatalyst with high visible light photocatalytic performance. *Catalysis Science and Technology*, 2(7), pp. 1332-1335.

Dong, F., Wang, Z., Sun, Y., Ho, W.K. and Zhang, H., 2013. Engineering the nanoarchitecture and texture of polymeric carbon nitride semiconductors for enhanced visible light photocatalytic activity. *Journal of Colloid and Interface Science*, 401, pp. 70-79.

Dong, H., Guo, X.T., Yang, C., Ouyang, Z.Z., 2017. Synthesis of g-C_3N_4 by different precursors under burning explosion effect and its photocatalytic degradation for tylosin. *Applied Catalysis B: Environmental.*

Dong, S.Y., Feng, J.L., Fan, M.H., Pi, Y.Q., Hu, L.I., Han, X., Liu, M.L., Sun, J.Y. and Sun, J.H., 2015. Recent developments in heterogeneous photocatalytic water treatment using visible light responsive photocatalysis: a review. *RSC Advances*, 5.

Donohue, M.D. and Aranovich, G.L., 1998. Classification of gibbs adsorption isotherms. *Advances in Colloid and Interface Science*, 76-77, pp. 137-152.

Dunlop, P.S.M., Byrne, J.A., Manga, N. and Eggins, B.R., 2002. The photocatalytic removal of bacterial pollutants from drinking water. *Journal of Photochemistry and Photobiology A: Chemistry*, 148, pp. 355-363.

Fang, S., Xia, Y., Lv, K.L., Li, Q., Sun, J. and Li, M., 2015. Effect of carbon-dots modification on the structure and photocatalytic activity of g-C_3N_4. *Applied Catalysis B: Environmental*, 185, pp. 225-232.

Foo, K.Y. and Hameed, B.H., 2011. Preparation of oil palm (Elaeis) empty fruit brunch activated carbon by microwave-assisted KOH activation for the adsorption of methylene blue. *Desalination*, 275, pp. 302-305.

Fox, M.A. and Dulay, M.T., 1993. Heterogeneous photocatalysis. *Chemical Reviews*, 93(1), pp. 341-357.

Foy, D., Demazeau, G., Florian, P., Massiot, D., Labrugere, C. and Goglio, G., 2009. Modulation of the crystallinity of hydrogenated nitrogen-rich graphitic carbon nitrides. *Journal of Solid State Chemistry*, 182(1), pp. 165-171.

Fujishima, A.; Zhang, X. and Tryk, D.A., 2008. TiO_2 photocatalysis and related surface phenomena. *Surface Science Report*, 63(12), pp. 515–582.

Gago, R., Jimenez, I, Caceres, D., Agullo-Rueda, F., Sajavaara, T., Albella, J.M., Climent-Font, A., Vergara, I., Raisanen, J. and Rauhala, E., 2001. Hardening mechanisms in graphitic carbon nitride films grown with N_2/Ar ion assistance, *Chemistry of Materials*, 13(1), pp. 129-135.

Ge, L., Han, C., Liu, J. and Li, Y., 2011. Enhanced visible light photocatalytic activity of novel polymeric g-C_3N_4 loaded with Ag nanoparticles. *Applied Catalysis A: General*, 409-410, pp. 215-222.

Guo, J. and Lua, A.C., 2002. Microporous activated carbon prepared from palm shell by thermal activation and their application to sulphur dioxide adsorption. *Journal of Colloid and Interface Science*, 251, pp. 242-247.

Guo, Q.X., Xie, Y., Wang, X.J., Lv, S.C., Hou, T. and Liu, X.M., 2003. Characterization of well-crystallized graphitic carbon nitride nanocrystallites via benzene-thermal route at low temperatures. *Chemical Physics Letters*, 380(1), pp. 84-87.

Gurel, L. and Buyukgungor, H., 2011. Treatment of slaughterhouse plant wastewater by using a membrane bioreactor. *Water Science and Technology*, 64(1), pp.214-220.

Ha, K.S. and Suzuki, M., 1984. Model calculation of chemical regeneration of spent clinoptilolite from ammonium treatment. *Journal of Chemical Engineering of Japan*, 17(3), pp. 294-303.

HACH, 2014. *Oxygen Demand, Chemical*. DOC316.53.01099.

HACH, 2015. *Nitrogen, Ammonia*. DOC316.53.01077.

HACH, 2017. *Phosphorus, Reactive (Orthophosphate)*. DOC316.53.01119.

Hakobyan, K., Gegenhuber, T., McErlean, C.S.P. and Müllner, M., 2019. Visible-light-driven MADIX polymerisation via a reusable, low-cost, and non-toxic bismuth oxide photocatalyst. *Angewandte Chemie International Edition in English*, 58(6), pp. 1828-1832.

Hameed, B.H., Tan, I.A.W. and Ahmad, A.L., 2009. Preparation of oil palm empty fruit bunch-based activated carbon for removal of 2,4,6-trichlorophenol: optimization using response surface methodology. *Journal of Hazardous Materials*, 164, pp. 1316-1324.

He, Z.Q., Chen, J.P., Chen, Y., Makwarimba, C.P., Huang, X.W., Zhang, S.H., Chen, J.M. and Song, S., 2018. An activated carbon fiber-supported graphite carbon nitride for effective electro-Fenton process. *Electrochimica Acta*, 276, pp. 377-388.

Herrmann, J.M., 1999. Heterogeneous photocatalysis: fundamentals and applications to the removal of various types of aqueous pollutants. *Catalysis Today*, 53, pp. 115-129.

Holladay, J.D.; Hu, J.; King, D.L. and Wang, Y., 2009. An overview of hydrogen production technologies. *Catalysis Today*, 139, pp. 244–260.

Hu, S.Z., Jin, R.R., Lu, G., Liu, D. and Gui, J.Z., 2014. The properties and photocatalytic performance comparison of Fe^{3+} doped g-C_3N_4 and Fe_2O_3/g-C_3N_4 composite catalysts. *RSC Advances*, 4(47).

Ibhadon, A.O. and Fitzpatrick, P., 2013. Heterogeneous Photocatalysis: Recent Advances and Applications. *Catalysts*, 3, pp. 189-218.

Ibhadon, A.O., 2018. Multifunctional TiO_2 Catalysis and Applications. *In Proceedings of Green Chemistry and Engineering International Conference*, Washington, DC, USA, pp. 24–26.

Imam M.A.M., 1984. *Poultry Wastewater Treatment in Sudan*. DOI: 10.13140/RG.2.1.3641.6485.

Inagaki, M., Tsumura, T., Kinumoto, T. and Toyoda, M., 2019. Graphitic carbon nitride (g-C_3N_4) with comparative discussion to carbon materials. *Carbon*, 141, pp. 580-607.

Ioannidou, O. and Zabaniotou, A., 2007. Agricultural residue as precursors for activated carbon production: a review. *Renewable and sustainable energy reviews*, 11(9), pp. 1966-2005.

Jaramillo-Páez, C.A., Navío, J.A., Hidalgo, M.C. and Macías, M., 2018. ZnO and Pt-ZnO photocatalysts: characterization and photocatalytic activity assessing by means of three substrates. *Catalysis Today*, 313, pp. 12-19.

Jestin, Y., 2013. Down-shifting of the incident light for photovoltaic applications. *Comprehensive Renewable Energy*, 1, pp. 563-585.

Ji, Z., 2017. Electrochemical degradation of diclofenac for pharmaceutical wastewater treatment. *International Journal of Electrochemical Science*, pp.7807-7816.

Jover-Smet, M., Martin-Pascual, J. and Trapote, A., 2017. *Model of Suspended Solids Removal in the Primary Sedimentation Tanks for the Treatment of Urban Wastewater.*

Kanakaraju, D., Glass, B.D. and Oelgemoller, M., 2014. Titanium oxide photocatalysis for pharmaceutical wastewater treatment. *Environmental Chemistry Letters*, 12(1), pp.27-47.

Kang, Y., Yang, Y., Yin, L.C., Kang ,X., Liu, G. and Cheng, H.M., 2015. An amorphous carbon nitride photocatalyst with greatly extended visible-light responsive range for photocatalytic hydrogen generation. *Advanced Materials*, 27, pp. 4572-4577.

Karoly, K. and Suzuki, M., 1992. Attachment and growth of biomass on surface modified activated carbon fibers. *Water Science and Technology*, 26, pp. 665-671.

Katsumata, H., Sakai, T., Suzuki, T. and Kaneco, S., 2014. Highly efficient photocatalytic activity of g-C_3N_4/Ag_3PO_4 hybrid photocatalysts through Z-scheme photocatalytic mechanism under visible light. *Ind. Eng. Chem. Research*, 53, pp. 8018-8025.

Kim, D.W., Kil, H.S., Nakabayashi, K., Yoon, S.H. and Miyawaki, J., 2017. Structural elucidation of physical and chemical activation mechanisms based on the microdomain structure model. *Carbon*, 114, pp. 98-105.

Kim, M., Hwang, S. and Yu, J.S., 2007. Novel ordered nanoporous graphitic C_3N_4 as a support for Pt-Ru anode catalyst in direct methanol fuel cell. *Journal of Materials Chemistry*, 17, pp. 1656-1659.

Koehlert, K., 2017. Activated carbon: fundamentals and new applications. *Chemical Engineering*. [online] Available through: <www.chemengonline.com> [Accessed 27 August 2019]

Kumar, P.S., Korving, L., Keesman, K.J., Loosdrecht, M.C.M.V. and Witkamp, G.J., 2019. Effect of pore size distribution and particle size of porous metal oxides on phosphate adsorption capacity and kinetics. *Chemical Engineering Journal*, 358, pp. 160-169.

Kumar, S., Karthikeyan, S. and Lee, A.F., 2018. g-C_3N_4-based nanomaterials for visible light-driven photocatalysis. *Catalysts*, 8(2).

Kumar, V., 2012. *Adsorption/ Desorption and Regeneration*. [online] Available through: <https://www.slideshare.net/VivekKumar36/adsorption-regenerationvivek-kumarneeri> [Accessed 14 August 2019]

Kwiatkowski, M., Kalderis, D. and Diamadopoulos, E., 2017. Numerical analysis of the influence of the impregnation ratio on the microporous structure formation of activated carbons, prepared by chemical activation of waste biomass with phosphoric (V) acid. *Journal of Physics and Chemistry of Solids*, 105, pp. 81-85.

Laysandra, L., Sari, M.W.M.K., Soedaredjo, F.E., Foe, K., Putro, J.N., Kurniawan, A., Ju, Y.H. and Ismadji, S., 2017. Adsorption and photocatalytic performance of bentonite-titanium oxide composites for methylene blue and rhodamine B decoloration. *Heliyon*, 3(12).

Lewis, L.N., 1993. Chemical catalysis by colloids and clusters. *Chemical Reviews*, 93, pp.2693-2730.

Li, G., Lv, L., Fan, H., Ma, J, Li, Y., Wan, Y. and Zhao, X.S., 2010. Effect of the agglomeration of TiO_2 nanoparticles on their photocatalytic performance in the aqueous phase. *Journal of Colloid and Interface Science*, 348(2), pp. 342-347.

Li, X., Hartley, G., Ward, A.J., Young, P.A., Masters, A.F. and Maschmeyer, T., 2015. Hydrogenated defects in graphitic carbon nitride nanosheets for improved photocatalytic hydrogen evolution. *The Journal of Physical Chemistry*, 119, pp. 14938-14946.

Li, X., Zhang, J., Shen, L., Ma, Y., Lei, W., Cui, Q. and Zou, G., 2009. Preparation and characterization of graphitic carbon nitride through pyrolysis of melamine. *Applied Physics A*, 94(2), pp. 387-392.

Liang, Q., Li, Z., Huang, Z.H., Kang, F. and Yang, Q.H., 2015. Holey graphitic carbon nitride nanosheets with carbon vacancies for higly improved photocatalytic hydrogen production. *Advanced Functional Materials*, 25(44), pp. 6885-6892.

Limousin, G., Gaudet, J.P., Charlet, L., Szenknect, S., Barthes, V. and Krimissa, M., 2007. Sorption isotherms: a review on physical bases, modelling and measurement. *Applied Geochemistry*, 22, pp. 249-275.

Lin, J.Q., Yang, S.E., Duan, J.M., Wu, J.J., Jin, L.Y., Lin, J.M. and Deng, Q.L., 2016. The Adsorption Mechanism of Modified Activated Carbon on Phenol. *MATEC Web of Conferences*, 67.

Liu, J., Zhang, T., Wang, Z., Dawson, G. and Chen, W., 2011. Simple pyrolysis of urea into graphitic carbon nitride with recyclable adsorption and photocatalytic activity. *Journal of Materials Chemistry*, 21(38), pp. 14398-14401.

Liu, P.X., Zhang, H.M., Feng, Y.J., Yang, F.L. and Zhang, J.P., 2014. Removal of trace antibiotics from wastewater: A systematic study of nanofiltration combined with ozone-based advanced oxidation processes. *Chemical Engineering Journal*, 240, pp.211-220.

Liu, Z., Kanjo, Y. and Mizutani, S., 2009. Removal mechanisms for endocrine disrupting compounds (EDCs) in wastewater treatment — physical means, biodegradation, and chemical advanced oxidation: A review. *Science of the Total Environment*, 407(2), pp.731–748.

Low, J., Yu, J., Jaroniec, M., Wageh, S. and Al-Ghamdi, A.A., 2017. Heterojunction photocatalysts. *Advanced Materials*.

Lu, D., Fang, P., Wu, W., Ding, J., Jiang, L., Zhao, X., Li, C., Yang, M., Li, Y. and Wang, D., 2017. Solvothermal-assisted synthesis of self-assembling TiO_2 nanorods on large graphitic carbon nitride sheets with their anti-recombination in the photocatalytic removal of Cr (VI) and rhodamine B under visible light irradiation. *Nanoscale*, 9(9), pp. 3231-3245.

Lv, S., Li, Y., Zhang, K., Lin, Z. and Tang, D., 2017. Carbon Dots/g-C_3N_4 Nanoheterostructures-Based Signal-Generation Tags for Photoelectrochemical Immunoassay of Cancer Biomarkers Coupling with Copper Nanoclusters. *ACS Applied Materials & Interfaces*, 9(44), pp. 38336-38343.

Ma, X.J., Yang, H.M., Yu, L.L., Chen, Y. and Li, Y., 2014. Preparation, Surface and Pore Structure of High Surface Area Activated Carbon Fibers from Bamboo by Steam Activation. *Materials*, 7, pp. 4431-4441.

Malato, S., Maldonado, M.I., Fernández-Ibáñez, P., Oller, I., Polo, I. and Sánchez-Moreno, R., 2016. Decontamination and disinfection of water by solar photocatalysis: The pilot plants of the Plataforma Solar de Almeria. *Materials Science in Semiconductor Processing*, 42, pp. 15-23.

Martin, D.J., Qiu, K., Shevlin, S.A., Handoko, A.D., Chen, X., Guo, Z. and Tang, J., 2014. Highly efficient photocatalytic H_2 evolution from water using visible light and structure-controlled graphitic carbon nitride. *Angewandte Chemie International Edition*, 53(35), pp. 9240-9245.

Martin-Ramos, P., Dante, R.C., Correa-Guimaraes, A. and Martin-Gil, J., 2011. Synthesis of graphitic carbon nitride by reaction of melamine and uric acid. *Materials Chemistry and Physics*, 130, pp. 1094-1102.

Martin-Ramos, P., Martin-Gil, J., Dante, R.C., Vaquero, F., Navarro, R.M. and Fierro, J.L.G., 2015. A simple approach to synthesize g-C_3N_4 with high visible light photoactivity for hydrogen production. *Journal of Materials Chemistry*.

McEvoy, J.G., 2014. *Carbon-enhanced photocatalysts for visible light induced detoxification and disinfection*.

Mittal, A., 2011. Biological wastewater treatment. *Water Today*.

Mo, Z., She, X.J., Li, Y.P., Liu, L., Huang, L.Y., Chen, Z.G., Zhang, Q., Xu, H. and Li, H.M., 2015. Synthesis of g-C_3N_4 at different temperatures for superior visible/UV photocatalytic performance and photoelectrochemical sensing of MB solution. *RSC Advanced*, 5.

Nardi, I.R., Fuzi, T.P. and Del Nervy, V., 2008. Performance evaluation and operating strategies of dissolved air flotation system treating poultry slaughterhouse wastewater. *Resources, Conservation and Recycling*, 52(3), pp.533-544.

Nash, R., 2013. The oceans and their challenge to conserve marine biodiversity. *Living with Water: Targeting Quality in a dynamic world*.

National Water Services Commission, 2019. *Malaysian Sewerage Industry Guidelines*. [online] Available through: <https://www.span.gov.my/article/view/malaysian-sewerage-industry-guidelines-msig> [Accessed 31 July 2019]

Nayak, A., Bhushan, B., Gupta, V. and Sharma, P., 2017. Chemically activated carbon from lignocellulosic wastes for heavy metal wastewater remediation: effect of activation conditions. *Journal of Colloid and Interface Science*, 493, pp. 228-240.

New World Encyclopedia, 2018. *Activated Carbon*. [online] Available through: <https://www.newworldencyclopedia.org/entry/Activated_carbon> [Accessed 10 August 2019]

Niu, P., Yin, L.C., Yang, Y.Q., Liu, G. and Cheng, H.M., 2014. Increasing the visible light absorption of graphitic carbon nitride (melon) photocatalysts by homogeneous self-modification with nitrogen vacancies. *Advanced Materials*, 26(47), pp. 8046-8052.

Ollis, D.F., 2000. Photocatalytic purification and remediation of contaminated air and water. *Comptes Rendus de l'Académie des Sciences – Series IIC – Chemistry*, 3(6), pp. 405-411.

Omri, A. and Benzina, M., 2012. Characterization of activated carbon prepared from a new raw lignocellulosic material: ziziphus spina-christi seeds. *Journal de la Societe Chimique de Tunisie*, 14, pp. 175-183.

Ong, W.J., Tan, L.L., Chai, S.P. and Yong, S.T., 2015. Graphene oxide as a structure-directing agent for the two-dimensional interface engineering of sandwich-like graphene-g-C_3N_4 hybrid nanostructures with enhanced visible-light photoreduction of CO_2 to methane. *Chemical Communications*, 51, pp. 858-861.

Pelaez, M., Nolan, N.T., Pillai, S.C., Seery, M.K., Falaras, P., Kontos, A.G., Dunlop, P.S.M., Hamilton, J.W.J., Byrne, J.A., Shea, K.O'., Entezari, M.H. and Dionysion, D.D., 2012. A review on the visible light active titanium dioxide photocatalysts for environmental applications. *Applied Catalysis B Environmental*, 125, pp. 331-349.

Putra, E.K., Pranowo R., Sunarso, J., Indraswati, N. and Ismadji, S., 2009. Performance of activated carbon and bentonite for adsorption of amoxicillin from wastewater: Mechanisms, isotherms and kinetics. *Water Research*, 43(9), pp.2419-2430.

Rajakumar, R., Meenambal, T., Banu, J.R. and Yeom, I.T., 2011. *Treatment of Poultry Slaughterhouse Wastewater in Upflow Anaerobic Filter under Low Upflow Velocity*. Int. J. Environ. Sci. Tech., 8(1), 149-158.

Rajasulochana, P. and Preethy, V., 2016. Comparison on efficiency of various techniques in treatment of waste and sewage water – A comprehensive review. Resource. *Efficient Technologies*. [online] Available through: <https://www.sciencedirect.com/science/article/pii/S2405653716301683> [Accessed 26 June 2019]

Rajendran, A. B., Manivannan, G., Jothivenkatachalam, K. and Karthikeyan, S., 2015. Characterization studies of activated carbon from low cost agricultural waste: leucaena leucocephala seed shell. *Journal of Chemistry*, 8(3), pp. 330-338.

Reimerink, W.M.T.M., 1999. The use of activated carbon as catalyst and catalyst carrier in industrial applications. *Studies in Surface Science and Catalysis*, 120, pp. 751-769.

Rice, J.M., Caldwell, D.F. and Humenik, F.J., 2006. *Animal agriculture and the environment: National center for manure and animal waste management white papers*, pp.609-666.

Rouquerol, F., Rouquerol, J. and Sing, K., 1999. *Adsorption by Powders and Porous Solids, Principles, Methodology and Applications*. Academic Press:London, UK.

Sakka, S., 2013. *Handbook of Advanced Ceramics*.

Sakoda, A., Kawazoem K. and Suzuki, M., 1987. Adsorption of tri- and tetrachloroethylene from aqueous solutions on activated carbon fibers. *Water Research*, 21(6), pp. 717-722.

Sakoda, A., Kawazoem K. and Suzuki, M., 1987. Correlation of adsorption equilibrium data of volatile chlorinated hydrocarbons from aqueous solution to activated carbon fibers by the Dubinin Astakhov Equation. *Journal of Chemical Engineering of Japan*, 20(2), pp. 199-200.

Sammer, M., 2014. Biological and chemical wastewater treatment process. *Wastewater Treatment Engineering.*

Sanou, Y., Pare, S., Baba, G., Segbeaya, N.K. and Bonzi-Coulibaly, L.Y., 2015. Removal of COD in Wastewaters by Activated Charcoal from Rice Husk. *Revue Des Sciences De L'Eau*, 29(3), pp. 265-277.

Santosh, K., Surendar, T., Bharat, K., Arabinda, B. and Vishnu, S., 2013. Synthesis of magnetically separable and recyclable g-C_3N_4-Fe_3O_4 hybrid nanocomposites with enhanced photocatalytic performance under visible light irradiation. *The Journal of Physical Chemistry C*.

Segura, Y., Martinez, F. and Melero, J.A., 2013. Effective pharmaceutical wastewater degradation by Fenton oxidation with zero-valent ion. *Applied Catalysis B: Environmental*, 136-137, pp.64-69.

Sena, R.F., Moreira, R.F. and Jose, H.J., 2008. Comparison of coagulants and coagulation aids for treatment of meat processing wastewater by column flotation. *Bioresource Technology*, 99(17), pp.8221-8225.

Serpone, N. and Pelizzetti, E., 1989. *Photocatalysis, Fundamentals and Applications*, Wiley, New York.

Sing, K.S.W., Rouquerol, J., Rouquerol, F., 1998. *Adsorption by powders and porous solids*. San Diego, USA: Academic Press.

Singh, S.K. and Tang, W.Z., 2013. Statistical analysis of optimum Fenton oxidation conditions for landfill leachate treatment. *Waste Management*, 33(1), pp.8-81.

Srikanth, B., Goutham, R., Narayan, R.B., Ramprasath, A., Gopinath, K.P. and Sankaranarayanan, A.R., 2017. Recent advancements in supporting materials for immobilised photocatalytic applications in waste water treatment. *Journal Environmental Management*, 200, pp. 60-78.

Sun, Y., Xiong, T., Ni, Z., Liu, J., Dong, F., Zhang, W. and Ho, W.K., 2015. Improving g-C_3N_4 photocatalysis for NO_x removal by Ag nanoparticles decoration. *Applied Surface Science*, 358, pp. 356-362.

Suzuki, M. and Ha, S., 1984. Equilibrium and rate of ammonium ion exchange by clinoptilolite. *Journal of Chemical Engineering of Japan*, 17(2), pp. 139-145.

Tay, Q., Kanhera, P., Ng, C.F., Chen, S., Chakraborty, S., Huan, A.C.H., Sum, T.C., Ahuja, R. and Chen, Z., 2015. Defect engineered g-C_3N_4 for efficient visible light photocatalytic hydrogen production. *Chemistry of Materials*, 27, pp. 4930-4933.

The Department of Health, 2010. *Environmental Health Practitioner Manual: A Resource Manual for Environmental Health Practitioners Working with Aboriginal and Torres Strait Islander Communities*. [online] Available through:<https://www.health.gov.au/internet/publications/publishing.nsf/Content/ohp-enhealth-manual-atsi-cnt-l~ohp-enhealth-manual-atsi-cnt-l-ch6~ohp-enhealth-manual-atsi-cnt-l-ch6.1> [Accessed 25 June 2019]

Thommes, M., Kaneko, K., Neimark, A. V., Olivier, J. P., Rodriguez-Reinoso, F., Rouquerol, J. and Sing, K. S. W., 2015. Physisorption of gases, with special reference to the evaluation of surface area and pore size distribution (IUPAC Technical Report). *Pure and Applied Chemistry*, 87(9), pp. 1052-1069.

Tiryaki, B., Yagmur, E., Banford, A. and Aktas, Z., 2014. Comparison of activated carbon produced from natural biomass and equivalent chemical compositions. *Journal of Analytical and Applied Pyrolysis*, 105, pp. 276-283.

Umar, M. and Aziz, H.A., 2006. Photocatalytic degradation of organic pollutants in water. *Organic Pollutants: Monitory Risk Treatment*, 8, pp. 195-208.

Wang, A.W., Wang, C.D., Fu, L., Ng, W.W. and Lan, Y.C., 2017. Recent advances of graphitic carbon nitride-based structures and applications in catalyst, sensing, imaging, and LEDs. *Nano-Mirco Letters*.

Wang, X., Maeda, K., Chen, X., Takanabe, K., Domen, K., Hou, Y., Fu, X. and Antonietti, M., 2009. Polymer semiconductors for artificial photosynthesis:

hydrogen evolution by mesoporous graphitic carbon nitride with visible light. *Journal of the American Chemical Society*, 131, pp. 1680-1681.

Wang, X., Maedam K., Thomas, A., Takanabe, K., Xin, G., Carlssonm J.M., Domen, K. and Antonietti, M., 2009. A metal-free polymeric photocatalyst for hydrogen production from water under visible light. *Nature Materials*, 8, pp. 76-80.

Wang, Y., Wang, F., Zuo, Y., Zhang, X. and Cui, L.F., 2014. Simple synthesis of ordered cubic mesoporous graphitic carbon nitride by chemical vapor deposition method using melamine. *Materials Letters*, 136, pp. 271-273.

Warhurst, A.M., Fowler, G.D., McConnachie, G.L. and Pollard, S.J.T, 1997. Pore structure and adsorption characteristics of steam pyrolysis carbons from Moringa oleifera. *Carbon*, 35(8), pp. 1039-1045.

Wong, S., Ngadi, N, Inuwa, I.M. and Hassan, O., 2017. Recent advances in applications of activated carbon from biowaste for wastewater treatment: a short review. *Journal of Cleaner Production*, 175, pp. 361-375.

Xian, T., Yang, H., Di, L.J. and Dai, J.F., 2015. Enhanced photocatalytic activity of $BaTiO_3$@g-C_3N_4 for the degradation of methyl orange under simulated sunlight irradiation. *Journal of Alloys and Compounds*, 622, pp. 1098-1104.

Xiang, Q.J., Yu, J.G. and Jaroniec, M., 2011. Preparation and Enhanced Visible-Light Photocatalytic H_2 Production Activity of Graphene/C_3N_4 Composites. *Journal of Physical Chemistry*, 115(15), pp. 7355-7363.

Xu, J., Brenner, T.J.K., Chen, Z., Neher, D., Antonietti, M. and Shalom, M., 2014. Upconversion-agent induced improvement of g-C_3N_4 photocatalyst under visible light. *ACS Applied Materials and Interfaces*, 6, pp. 16481-16486.

Yan, H., Chen, Y. and Xu, S., 2012. Synthesis of graphitic carbon nitride by directly heating sulfuric acid treated melamine for enhanced photocatalytic H_2 production from water under visible light. *International Journal of Hydrogen Energy*, 37(1), pp. 125-133.

Yan, S.C., Li, Z.S. and Zou, Z.G., 2009. Photodegradation performance of g-C_3N_4 fabricated by directly heating melamine. *Langmuir*, 25, pp. 10397-10401.

Yan, S.C., Li, Z.S. and Zou, Z.G., 2009. Photodegradation Performance of g-C_3N_4 Fabricated by Directly Heating Melamine. *Langmuir*, 25(17), pp. 10397-10401.

Yang, J., Chen, H., Gao, J., Yan, T., Zhou, F., Cui, S. and Bi, W., 2016. Synthesis of Fe_3O_4/g-C_3N_4 nanocomposites and their application in the photodegradation of 2,4,6-trichlorophenol under visible light. *Materials Letters*, 164, pp. 183-189.

Young, W.K., 2014. “Biological Treatment of Turkey Processing with Sand Filtration”. *Food Agricultural and Biological Engineering Graduate Program*. Ohio State University. Thesis PhD. 2-16.

Yu, Q., Guo, S., Li, X. and Zhang, M., 2014. One-step fabrication and high photocatalytic activity of porous graphitic carbon nitride/graphene oxide hybrid by direct polymerization of cyanamide without templates. *Russian Journal of Physical Chemistry A*, 88(10), pp. 1643-1649.

Yu, Q., Li, X. and Zhang, M., 2014. One-step fabrication and high photocatalytic activity of porous graphitic carbon nitride synthesized via direct polymerisation of dicyandiamide without templates. *Micro and Nano Letters*, 9(1), pp. 1-5.

Zawadzki, P., Kudlek, E. and Dudziak, M., 2018. Kinetic of the Photocatalytic Decomposition of Bisphenol A on Modified Photocatalysts. *Ecological Engineering*, 19(4), pp. 260–268.

Zhan, Y., Liu, Z.M., Liu, Q.Q., Huang, D., Wei, Y., Hu, Y.C., Lian, X.J. and Hu, C.F., 2017. A facile and one-pot synthesis of fluorescent graphitic carbon nitride quantum dots for bio-imaging applications. *New Journal of Chemistry*, 41(10), pp. 3930-3938.

Zhang, B., Ma, Z., Yang, F., Liu, Y. and Guo, M., 2017. Adsorption properties of ion recognition rice straw lignin on PdCl 4 2-: equilibrium, kinetics and mechanism. *Colloids and Surfaces A: Physicochemical and Engineering Aspects*, 514, pp. 260-268.

Zhang, G.G., Zhang, J.S., Zhang, M.W. and Wang, X.C., 2012. Polycondensation of thiourea into carbon nitride semiconductors as visible light photocatalysts. *Journal of Materials Chemistry*, 22, pp. 8083-8091.

Zhang, L.H., 2019. Well Production Performance Analysis for Shale Gas Reservoirs. *Developments in Petroleum Science*.

Zhang, S.J., Yu, H.Q. and Feng, H.M., 2006. PVA-based activated carbon fibres with lotus root-like axially porous structure. *Carbon*, 44(10), pp. 2059-2068.

Zhang, X., Xie, X., Wang, H., Zhang, J., Pan, B. and Xie, Y., 2013. Enhanced photoresponsive ultrathin graphitic-phase C_3N_4 nanosheets for bioimaging. *Journal of the American Chemical Society*, 135(1), pp. 18-21.

Zhang, Y., Liu, J., Wu, G. and Chen, W., 2012. Porous graphitic carbon nitride synthesized via direct polymerization of urea for efficient sunlight-driven photocatalytic hydrogen production. *Nanoscale*, 4, pp. 5300-5303.

Zhang, Y.H., Pan, Q.W., Chai, G.Q., Liang, M.R., Dong, G.P., Zhang, Q.Y. and Qiu, J.R., 2013. Synthesis and luminescence mechanism of multicolouremitting g-C_3N_4 nanopowders by low temperature thermal condensation of melamine. *Scientific Reports*, 3.

APPENDICES

APPENDIX A: BET Report

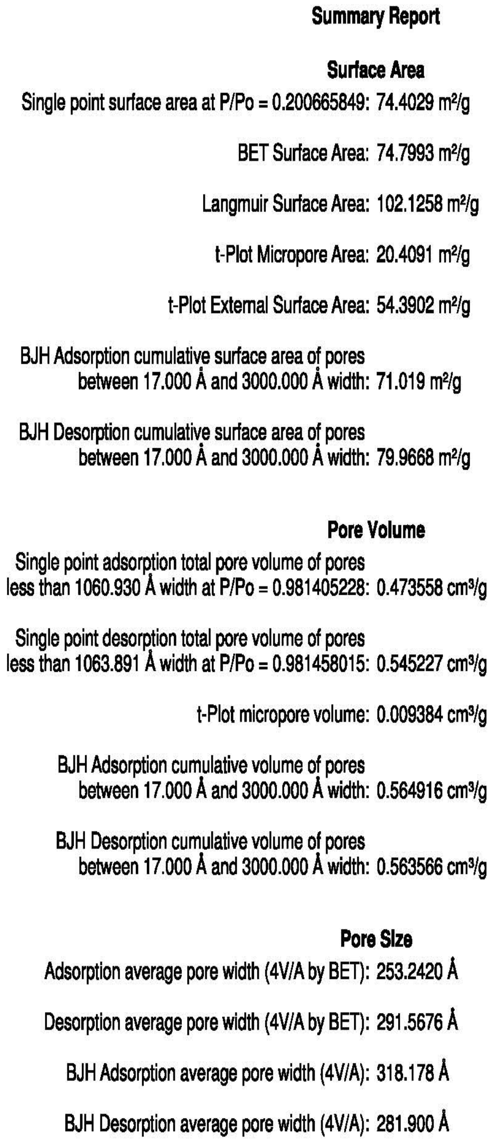

Summary Report

Surface Area

Single point surface area at P/Po = 0.200665849: 74.4029 m²/g

BET Surface Area: 74.7993 m²/g

Langmuir Surface Area: 102.1258 m²/g

t-Plot Micropore Area: 20.4091 m²/g

t-Plot External Surface Area: 54.3902 m²/g

BJH Adsorption cumulative surface area of pores between 17.000 Å and 3000.000 Å width: 71.019 m²/g

BJH Desorption cumulative surface area of pores between 17.000 Å and 3000.000 Å width: 79.9668 m²/g

Pore Volume

Single point adsorption total pore volume of pores less than 1060.930 Å width at P/Po = 0.981405228: 0.473558 cm³/g

Single point desorption total pore volume of pores less than 1063.891 Å width at P/Po = 0.981458015: 0.545227 cm³/g

t-Plot micropore volume: 0.009384 cm³/g

BJH Adsorption cumulative volume of pores between 17.000 Å and 3000.000 Å width: 0.564916 cm³/g

BJH Desorption cumulative volume of pores between 17.000 Å and 3000.000 Å width: 0.563566 cm³/g

Pore Size

Adsorption average pore width (4V/A by BET): 253.2420 Å

Desorption average pore width (4V/A by BET): 291.5676 Å

BJH Adsorption average pore width (4V/A): 318.178 Å

BJH Desorption average pore width (4V/A): 281.900 Å

Figure A-1: BET Summary Report of Pure g-C_3N_4.

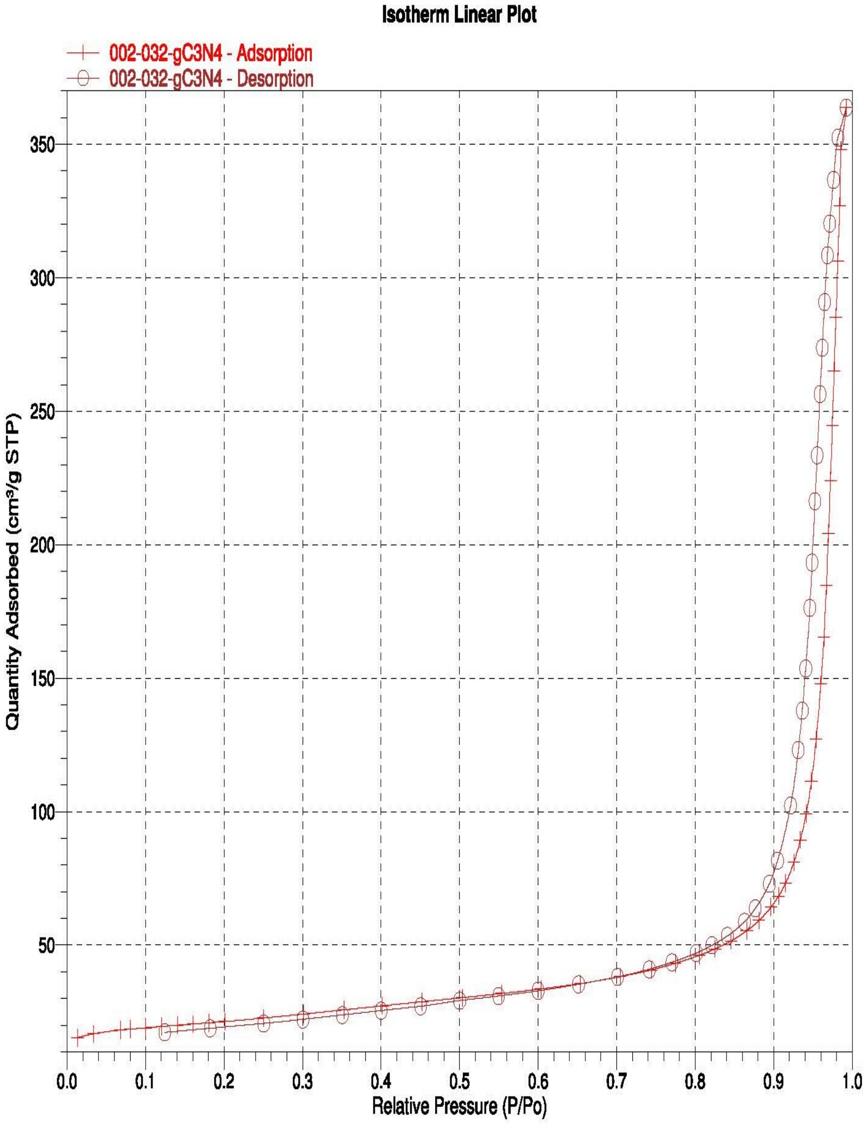

Figure A-2: N_2 Adsorption Isotherm of Pure g-C_3N_4.

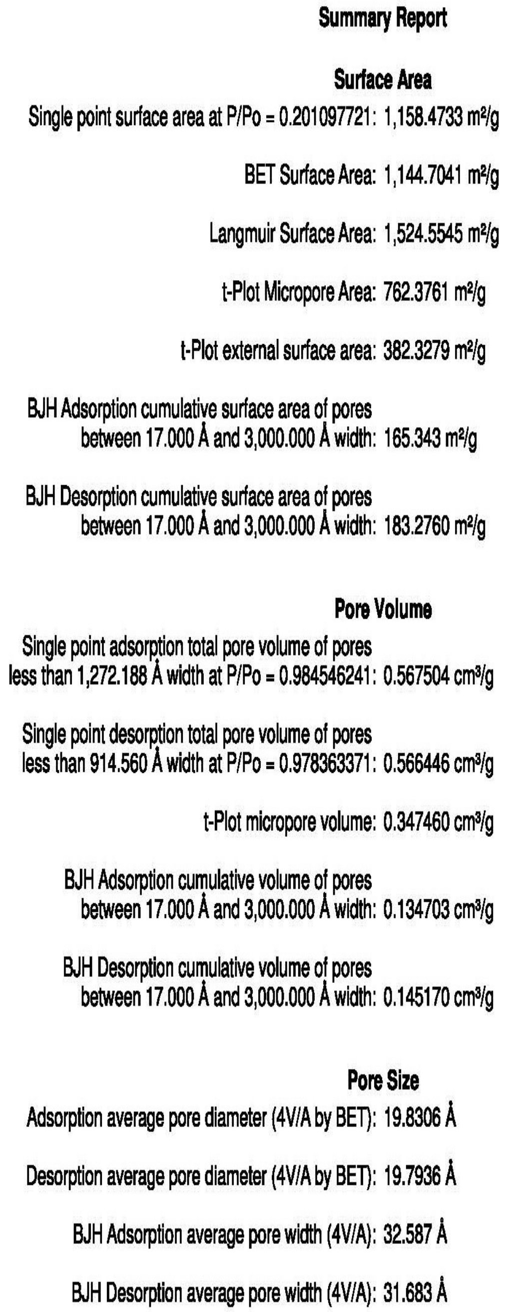

Summary Report

Surface Area

Single point surface area at P/Po = 0.201097721: 1,158.4733 m²/g

BET Surface Area: 1,144.7041 m²/g

Langmuir Surface Area: 1,524.5545 m²/g

t-Plot Micropore Area: 762.3761 m²/g

t-Plot external surface area: 382.3279 m²/g

BJH Adsorption cumulative surface area of pores between 17.000 Å and 3,000.000 Å width: 165.343 m²/g

BJH Desorption cumulative surface area of pores between 17.000 Å and 3,000.000 Å width: 183.2760 m²/g

Pore Volume

Single point adsorption total pore volume of pores less than 1,272.188 Å width at P/Po = 0.984546241: 0.567504 cm³/g

Single point desorption total pore volume of pores less than 914.560 Å width at P/Po = 0.978363371: 0.566446 cm³/g

t-Plot micropore volume: 0.347460 cm³/g

BJH Adsorption cumulative volume of pores between 17.000 Å and 3,000.000 Å width: 0.134703 cm³/g

BJH Desorption cumulative volume of pores between 17.000 Å and 3,000.000 Å width: 0.145170 cm³/g

Pore Size

Adsorption average pore diameter (4V/A by BET): 19.8306 Å

Desorption average pore diameter (4V/A by BET): 19.7936 Å

BJH Adsorption average pore width (4V/A): 32.587 Å

BJH Desorption average pore width (4V/A): 31.683 Å

Figure A-3: BET Summary Report of AC.

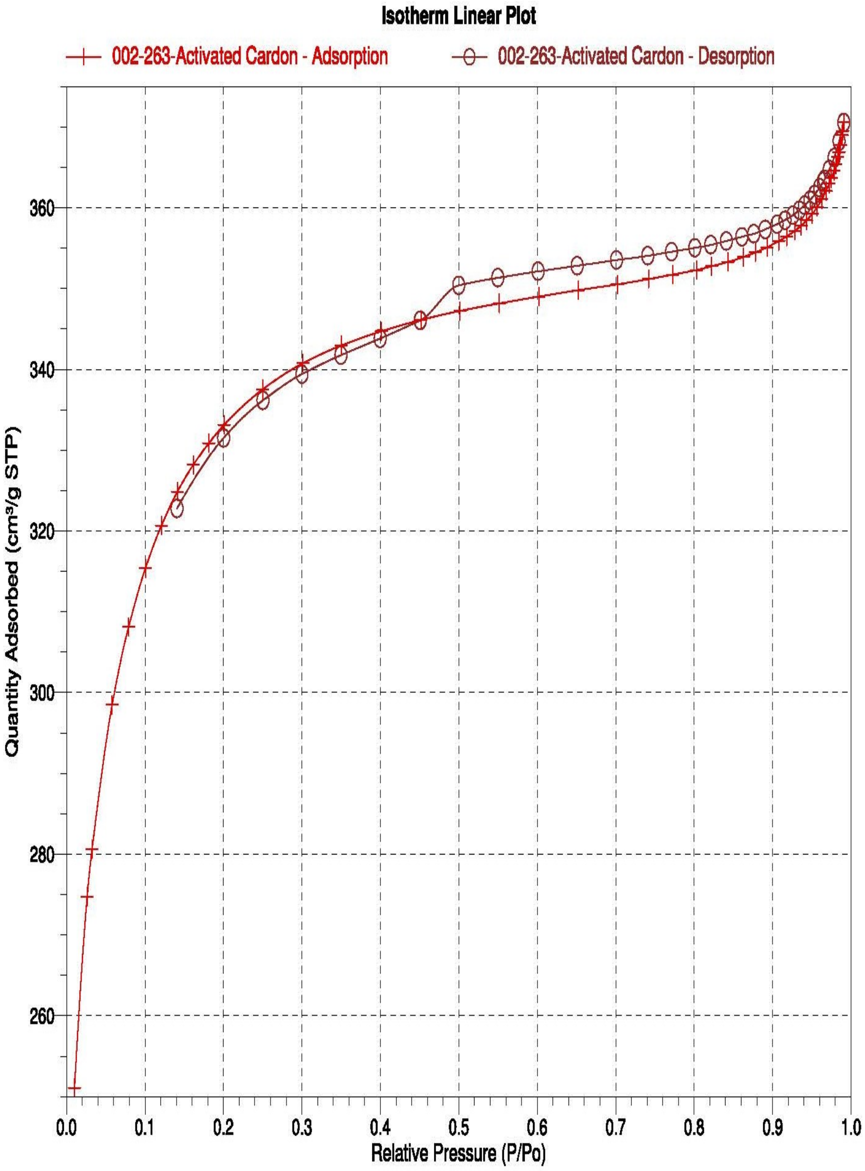

Figure A-4: N_2 Adsorption Isotherm of AC.

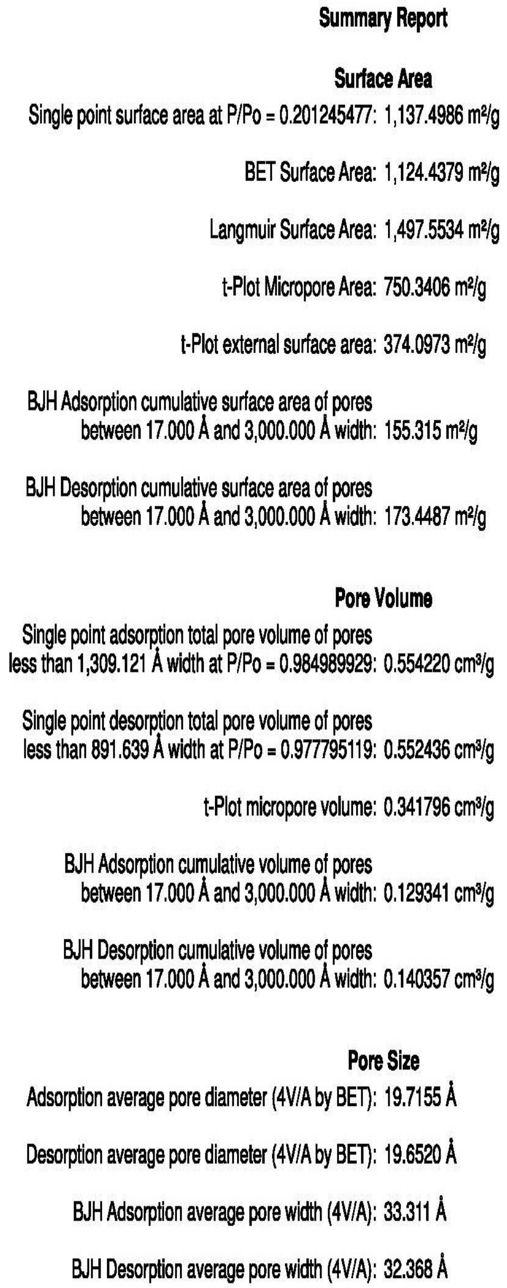

Summary Report

Surface Area

Single point surface area at P/Po = 0.201245477: 1,137.4986 m²/g

BET Surface Area: 1,124.4379 m²/g

Langmuir Surface Area: 1,497.5534 m²/g

t-Plot Micropore Area: 750.3406 m²/g

t-Plot external surface area: 374.0973 m²/g

BJH Adsorption cumulative surface area of pores
between 17.000 Å and 3,000.000 Å width: 155.315 m²/g

BJH Desorption cumulative surface area of pores
between 17.000 Å and 3,000.000 Å width: 173.4487 m²/g

Pore Volume

Single point adsorption total pore volume of pores
less than 1,309.121 Å width at P/Po = 0.984989929: 0.554220 cm³/g

Single point desorption total pore volume of pores
less than 891.639 Å width at P/Po = 0.977795119: 0.552436 cm³/g

t-Plot micropore volume: 0.341796 cm³/g

BJH Adsorption cumulative volume of pores
between 17.000 Å and 3,000.000 Å width: 0.129341 cm³/g

BJH Desorption cumulative volume of pores
between 17.000 Å and 3,000.000 Å width: 0.140357 cm³/g

Pore Size

Adsorption average pore diameter (4V/A by BET): 19.7155 Å

Desorption average pore diameter (4V/A by BET): 19.6520 Å

BJH Adsorption average pore width (4V/A): 33.311 Å

BJH Desorption average pore width (4V/A): 32.368 Å

Figure A-5: BET Summary Report of 20 wt% g-C_3N_4/PAC Composite.

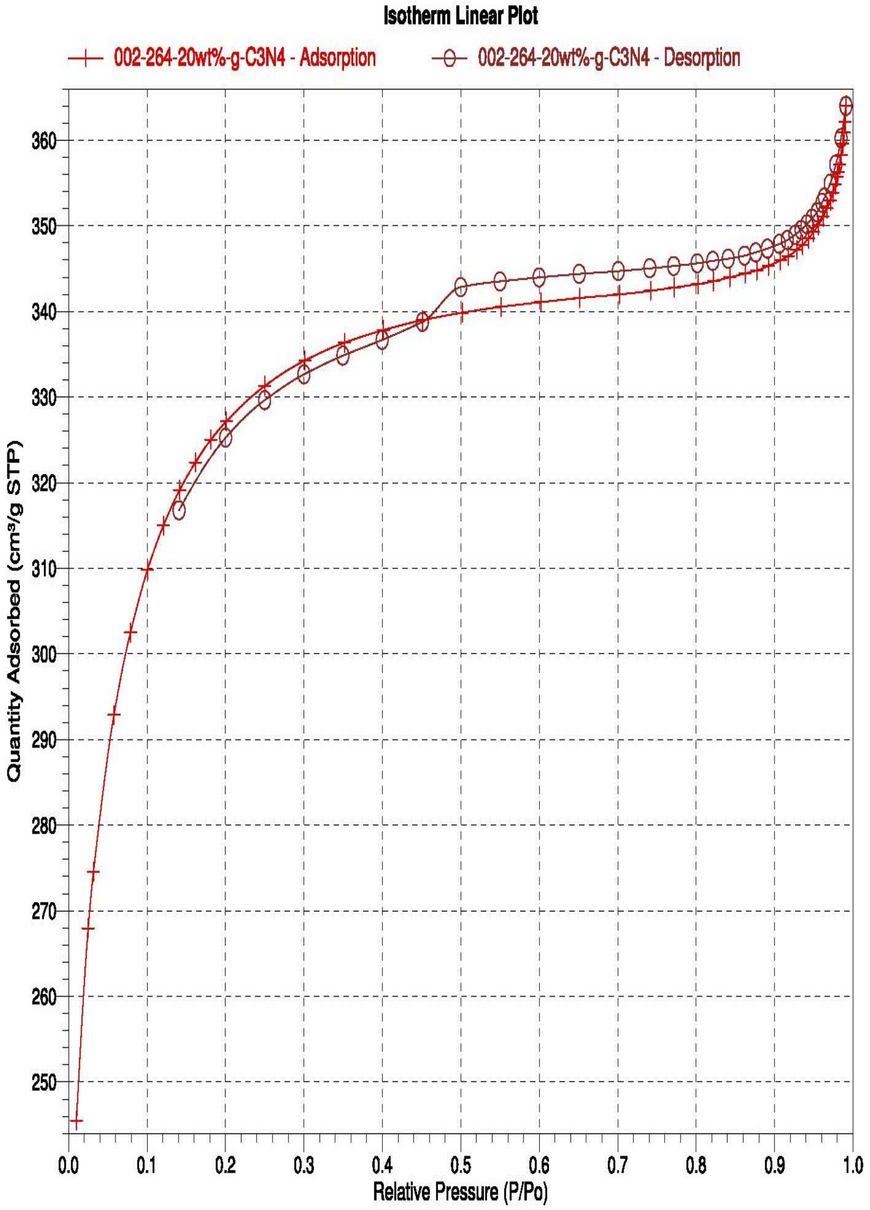

Figure A-6: N_2 Adsorption Isotherm of 20 wt% g-C_3N_4/PAC Composite.

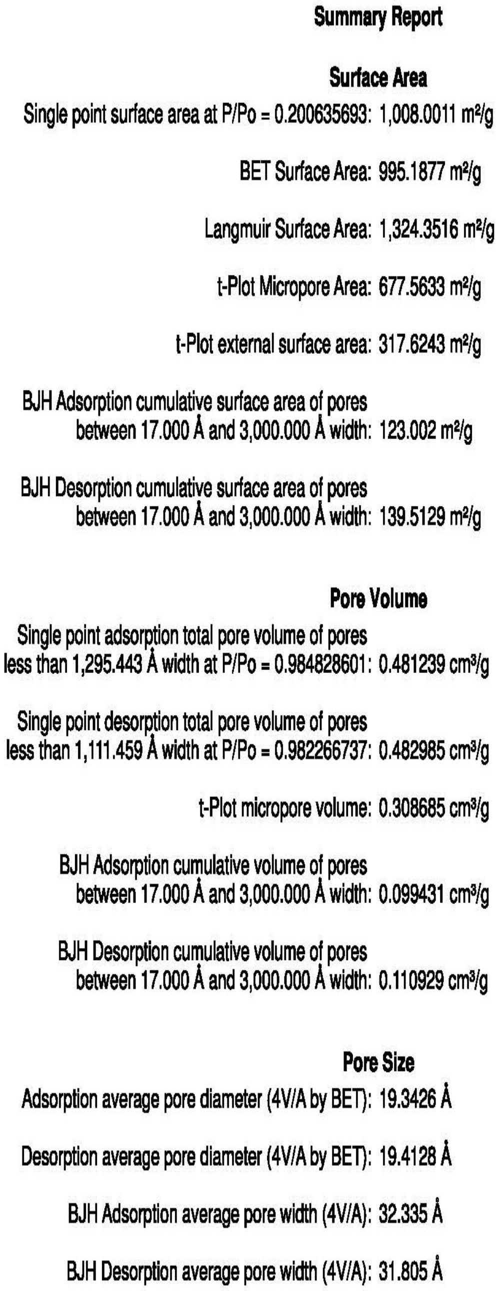

Summary Report

Surface Area

Single point surface area at P/Po = 0.200635693: 1,008.0011 m²/g

BET Surface Area: 995.1877 m²/g

Langmuir Surface Area: 1,324.3516 m²/g

t-Plot Micropore Area: 677.5633 m²/g

t-Plot external surface area: 317.6243 m²/g

BJH Adsorption cumulative surface area of pores
between 17.000 Å and 3,000.000 Å width: 123.002 m²/g

BJH Desorption cumulative surface area of pores
between 17.000 Å and 3,000.000 Å width: 139.5129 m²/g

Pore Volume

Single point adsorption total pore volume of pores
less than 1,295.443 Å width at P/Po = 0.984828601: 0.481239 cm³/g

Single point desorption total pore volume of pores
less than 1,111.459 Å width at P/Po = 0.982266737: 0.482985 cm³/g

t-Plot micropore volume: 0.308685 cm³/g

BJH Adsorption cumulative volume of pores
between 17.000 Å and 3,000.000 Å width: 0.099431 cm³/g

BJH Desorption cumulative volume of pores
between 17.000 Å and 3,000.000 Å width: 0.110929 cm³/g

Pore Size

Adsorption average pore diameter (4V/A by BET): 19.3426 Å

Desorption average pore diameter (4V/A by BET): 19.4128 Å

BJH Adsorption average pore width (4V/A): 32.335 Å

BJH Desorption average pore width (4V/A): 31.805 Å

Figure A-7: BET Summary Report of 40 wt% g-C_3N_4/PAC Composite.

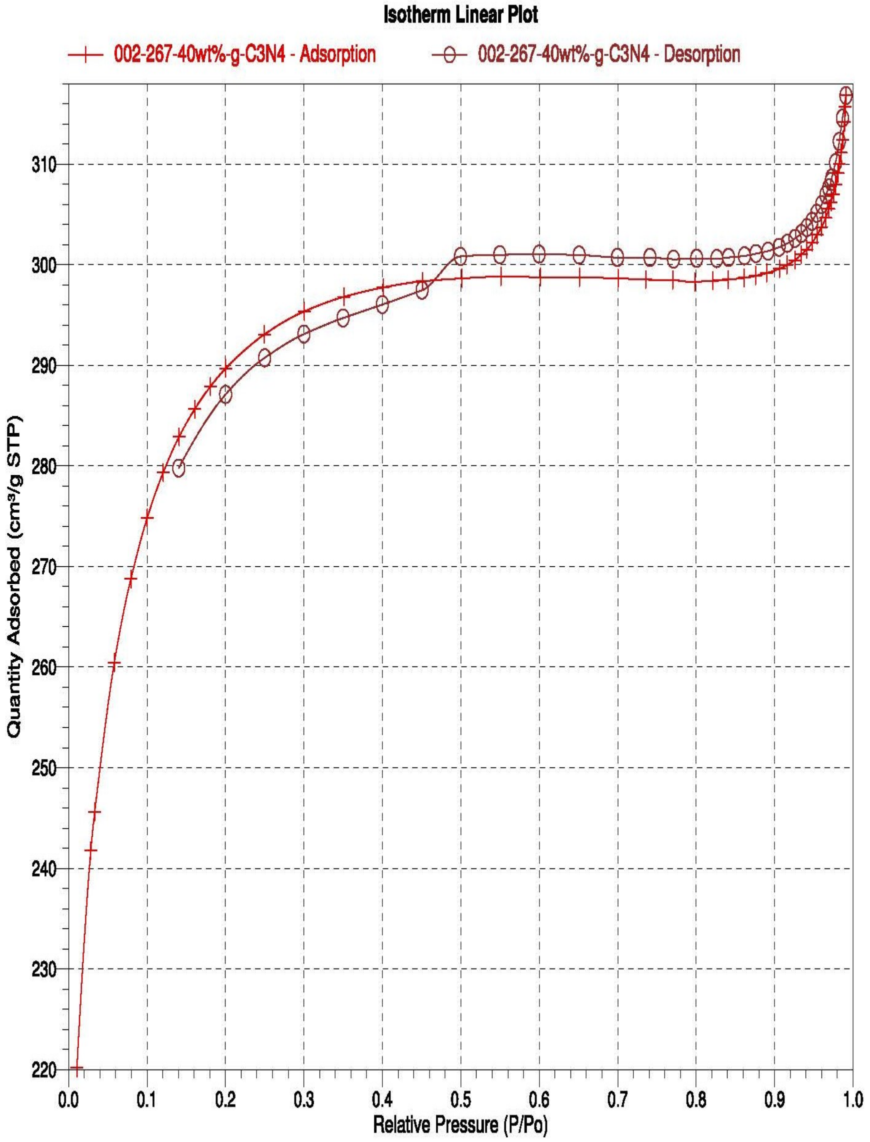

Figure A-8: N_2 Adsorption Isotherm of 40 wt% g-C_3N_4/PAC Composite.

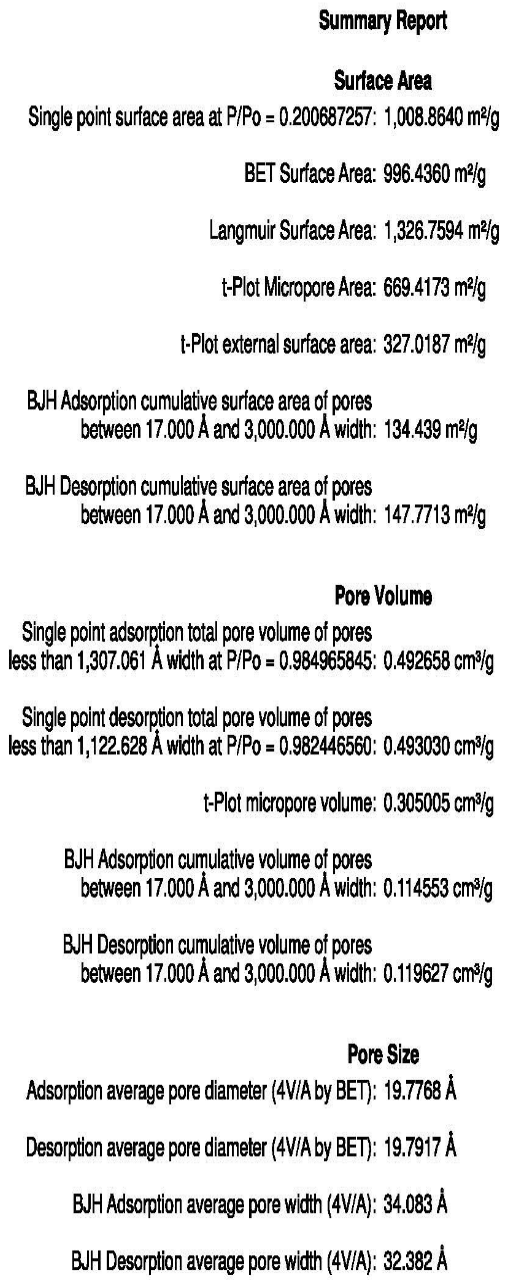

Summary Report

Surface Area

Single point surface area at P/Po = 0.200687257: 1,008.8640 m^2/g

BET Surface Area: 996.4360 m^2/g

Langmuir Surface Area: 1,326.7594 m^2/g

t-Plot Micropore Area: 669.4173 m^2/g

t-Plot external surface area: 327.0187 m^2/g

BJH Adsorption cumulative surface area of pores
between 17.000 Å and 3,000.000 Å width: 134.439 m^2/g

BJH Desorption cumulative surface area of pores
between 17.000 Å and 3,000.000 Å width: 147.7713 m^2/g

Pore Volume

Single point adsorption total pore volume of pores
less than 1,307.061 Å width at P/Po = 0.984965845: 0.492658 cm^3/g

Single point desorption total pore volume of pores
less than 1,122.628 Å width at P/Po = 0.982446560: 0.493030 cm^3/g

t-Plot micropore volume: 0.305005 cm^3/g

BJH Adsorption cumulative volume of pores
between 17.000 Å and 3,000.000 Å width: 0.114553 cm^3/g

BJH Desorption cumulative volume of pores
between 17.000 Å and 3,000.000 Å width: 0.119627 cm^3/g

Pore Size

Adsorption average pore diameter (4V/A by BET): 19.7768 Å

Desorption average pore diameter (4V/A by BET): 19.7917 Å

BJH Adsorption average pore width (4V/A): 34.083 Å

BJH Desorption average pore width (4V/A): 32.382 Å

Figure A-9: BET Summary Report of 60 wt% g-C_3N_4/PAC Composite.

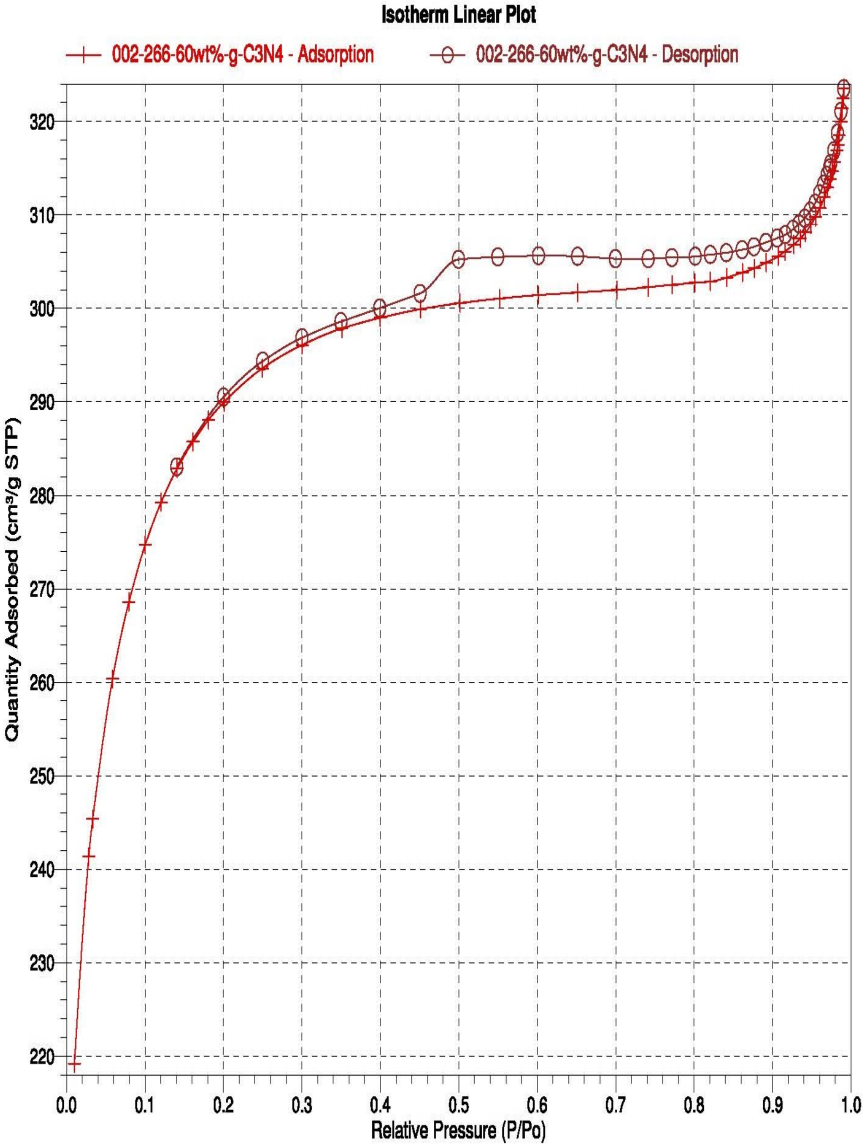

Figure A-10: N_2 Adsorption Isotherm of 60 wt% g-C_3N_4/PAC Composite.

APPENDIX B: FTIR Report

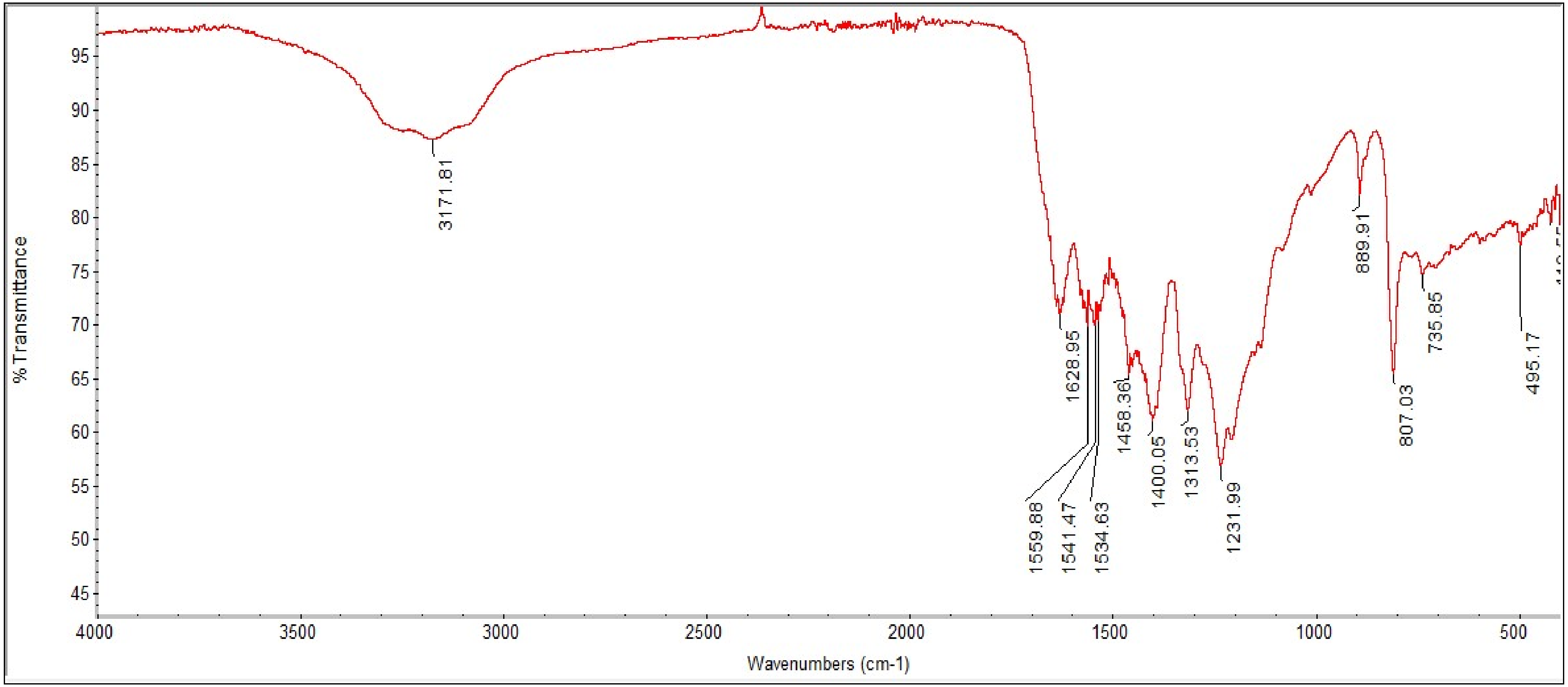

Figure B-1: FTIR Spectrum of Pure g-C_3N_4.

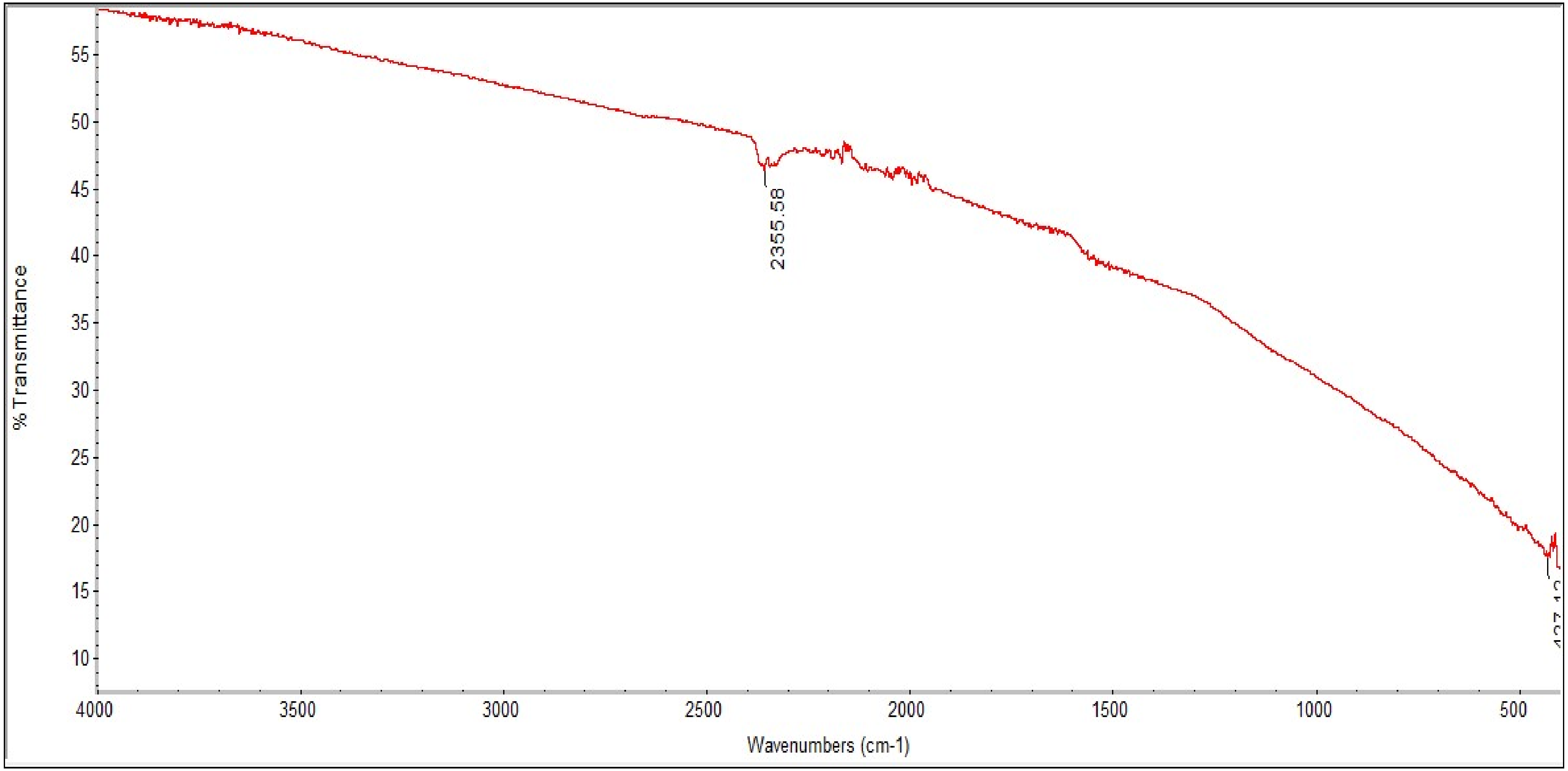

Figure B-2: FTIR Spectrum of AC.

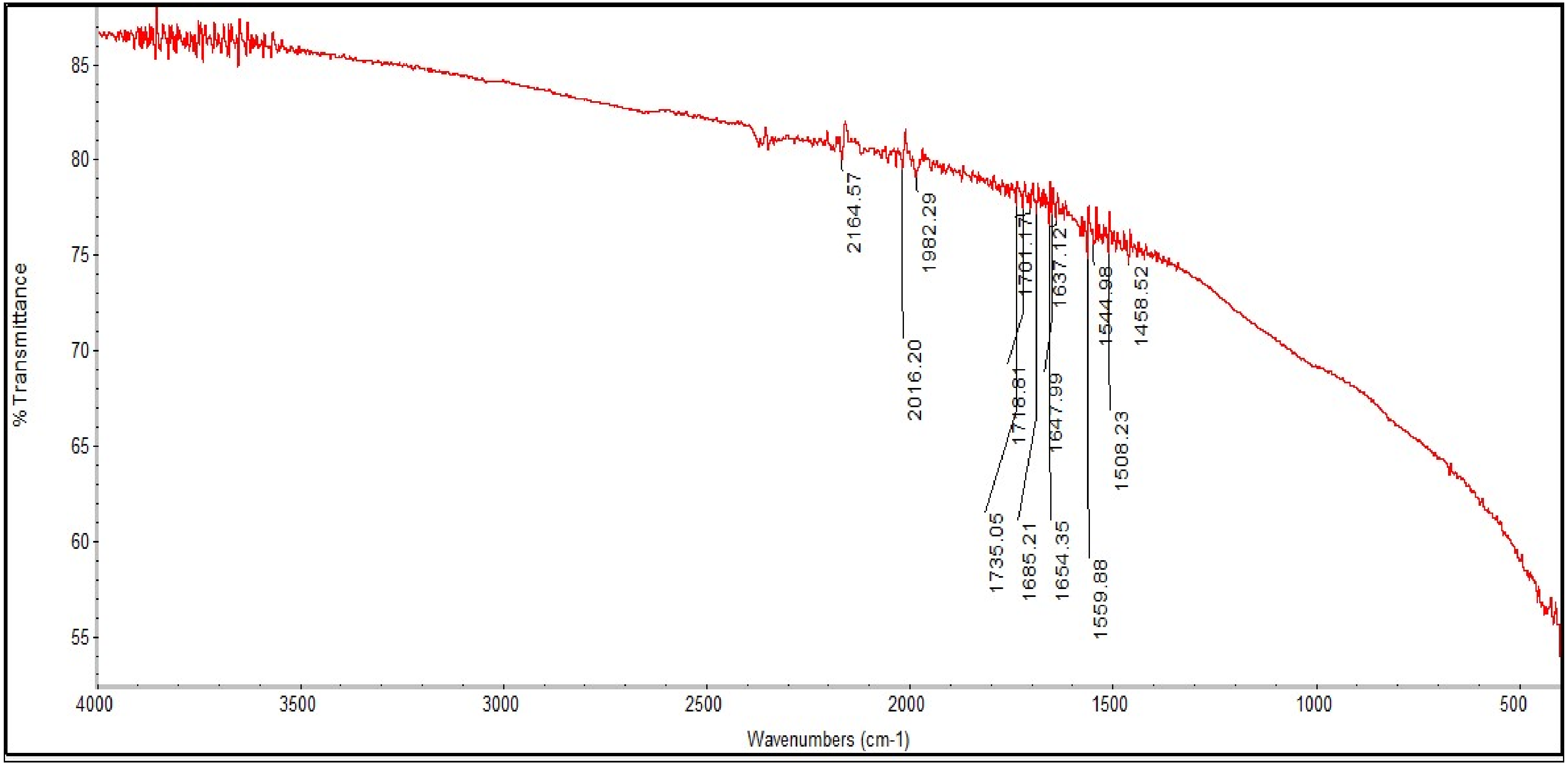

Figure B-3: FTIR Spectrum of 20 wt% g-C_3N_4/PAC Composite.

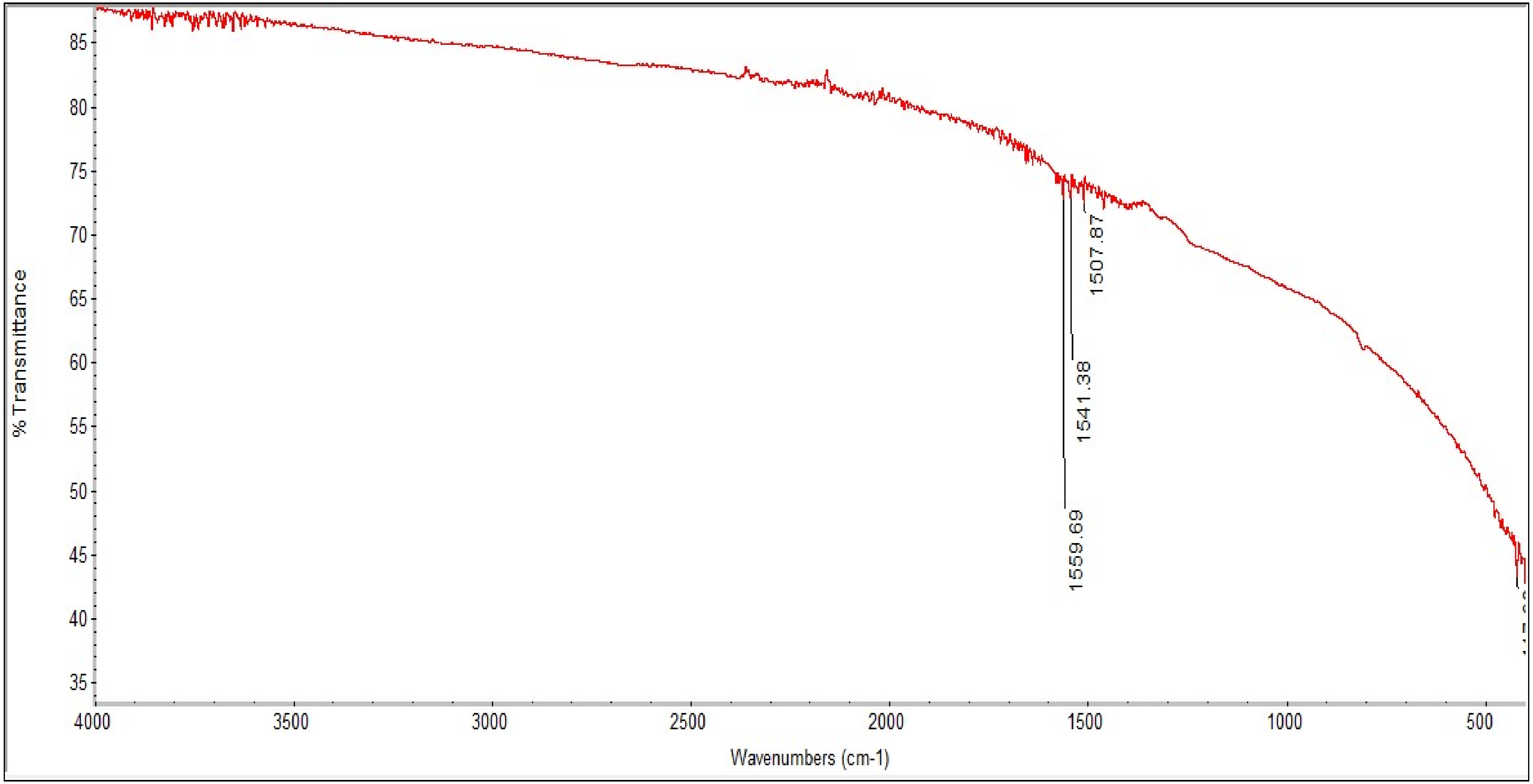

Figure B-4: FTIR Spectrum of 40 wt% g-C_3N_4/PAC Composite.

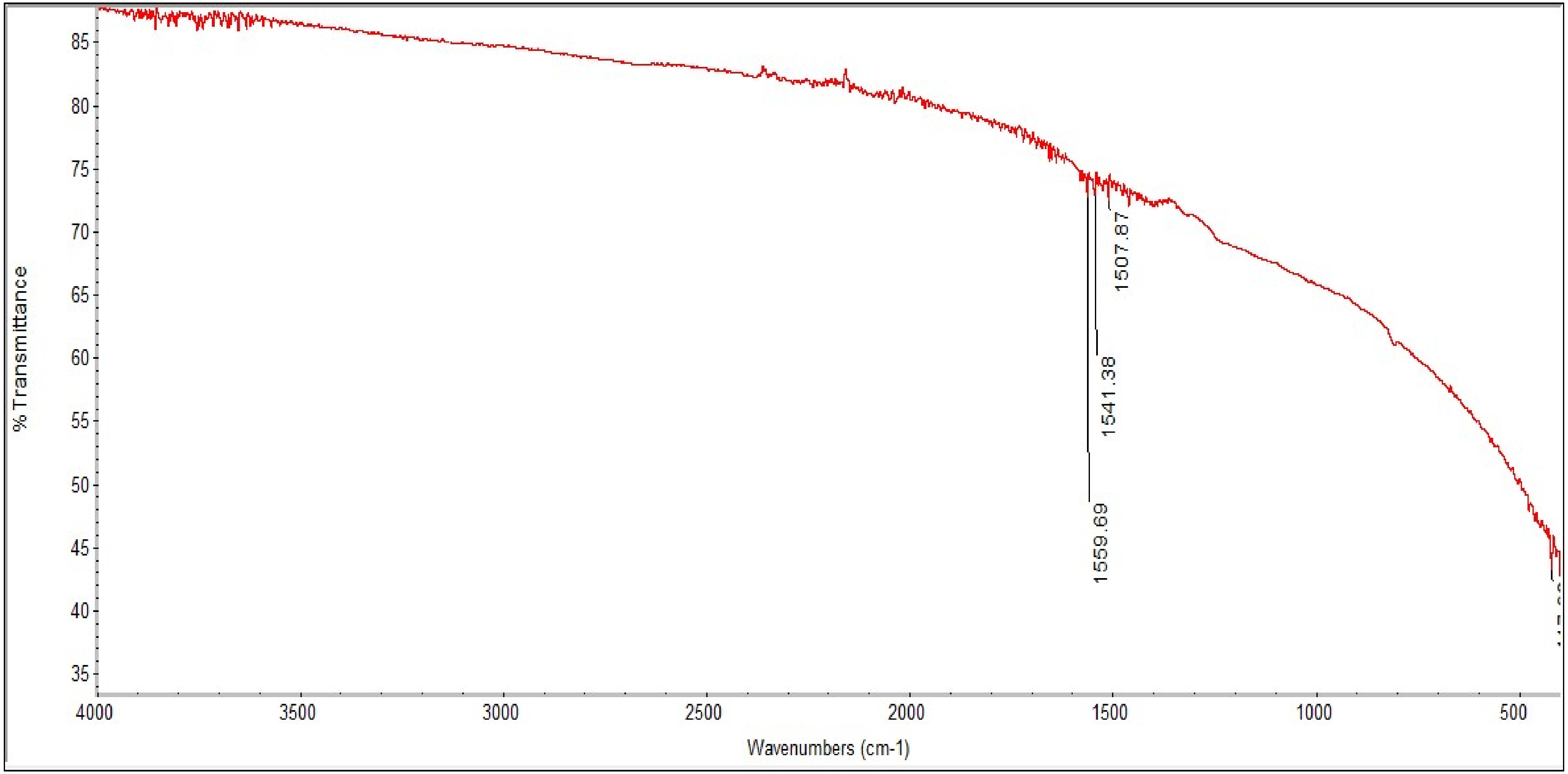

Figure B-5: FTIR Spectrum of 60 wt% g-C_3N_4/PAC Composite.

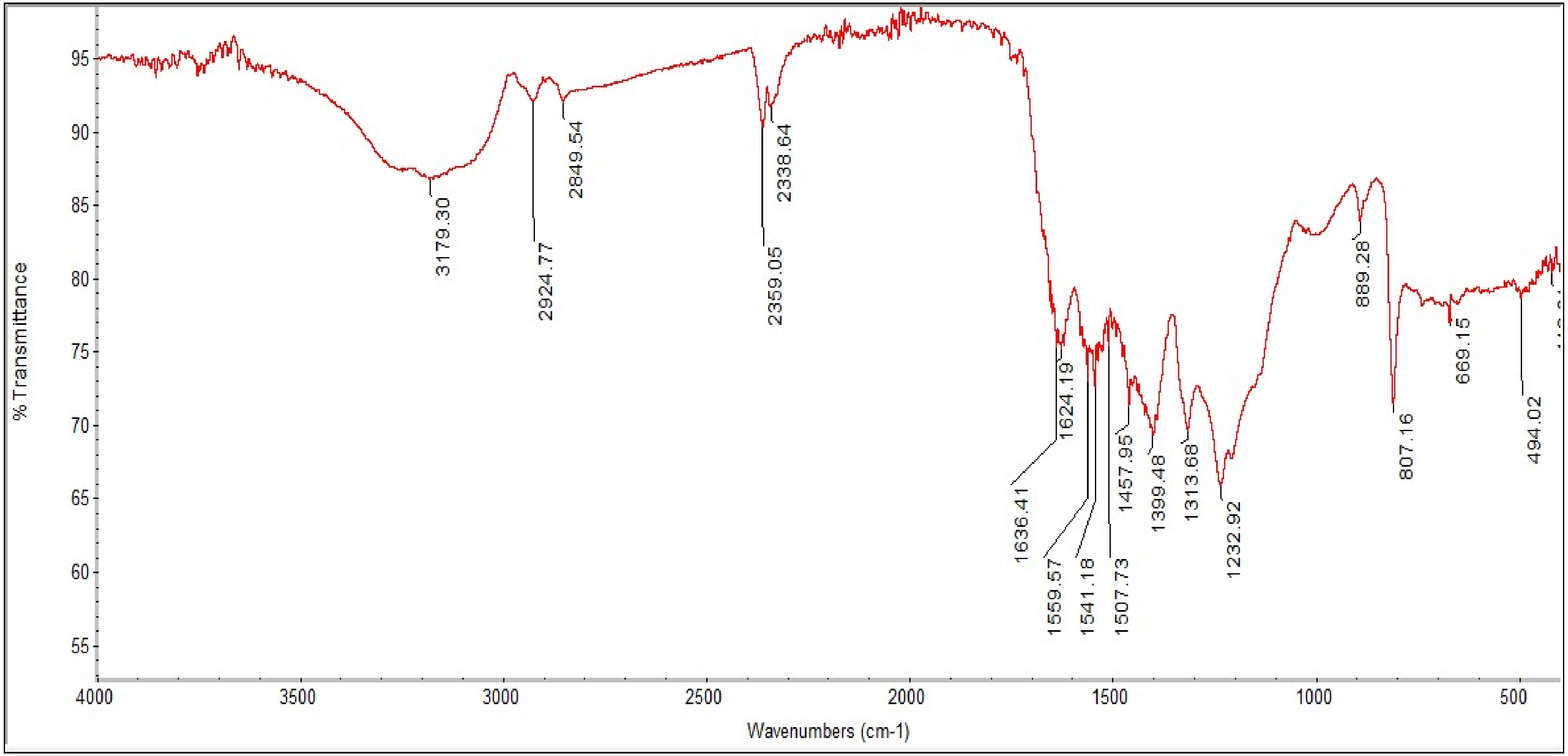

Figure B-6: FTIR Spectrum of Spent g-C_3N_4.

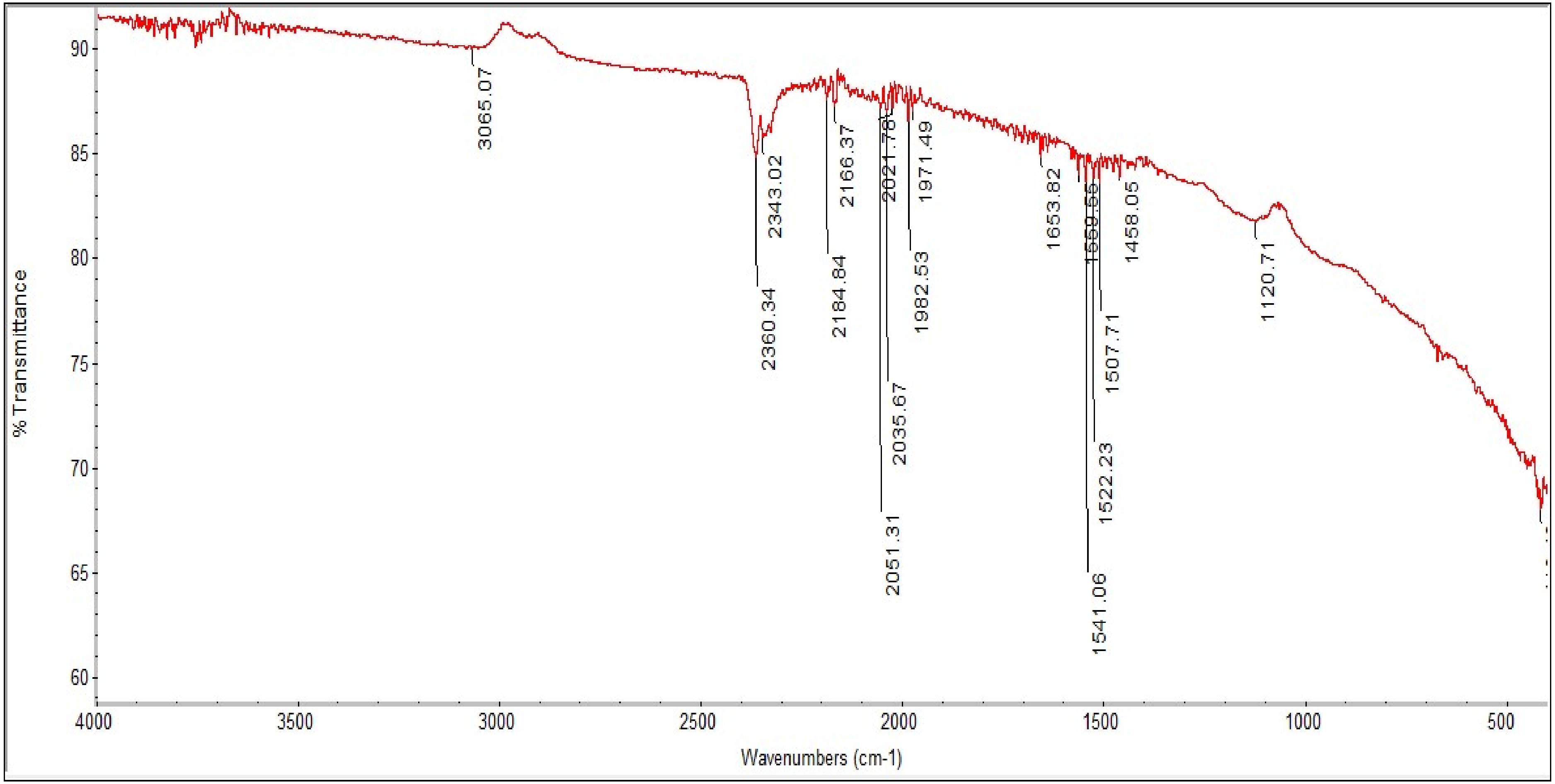

Figure B-7: FTIR Spectrum of Spent AC.

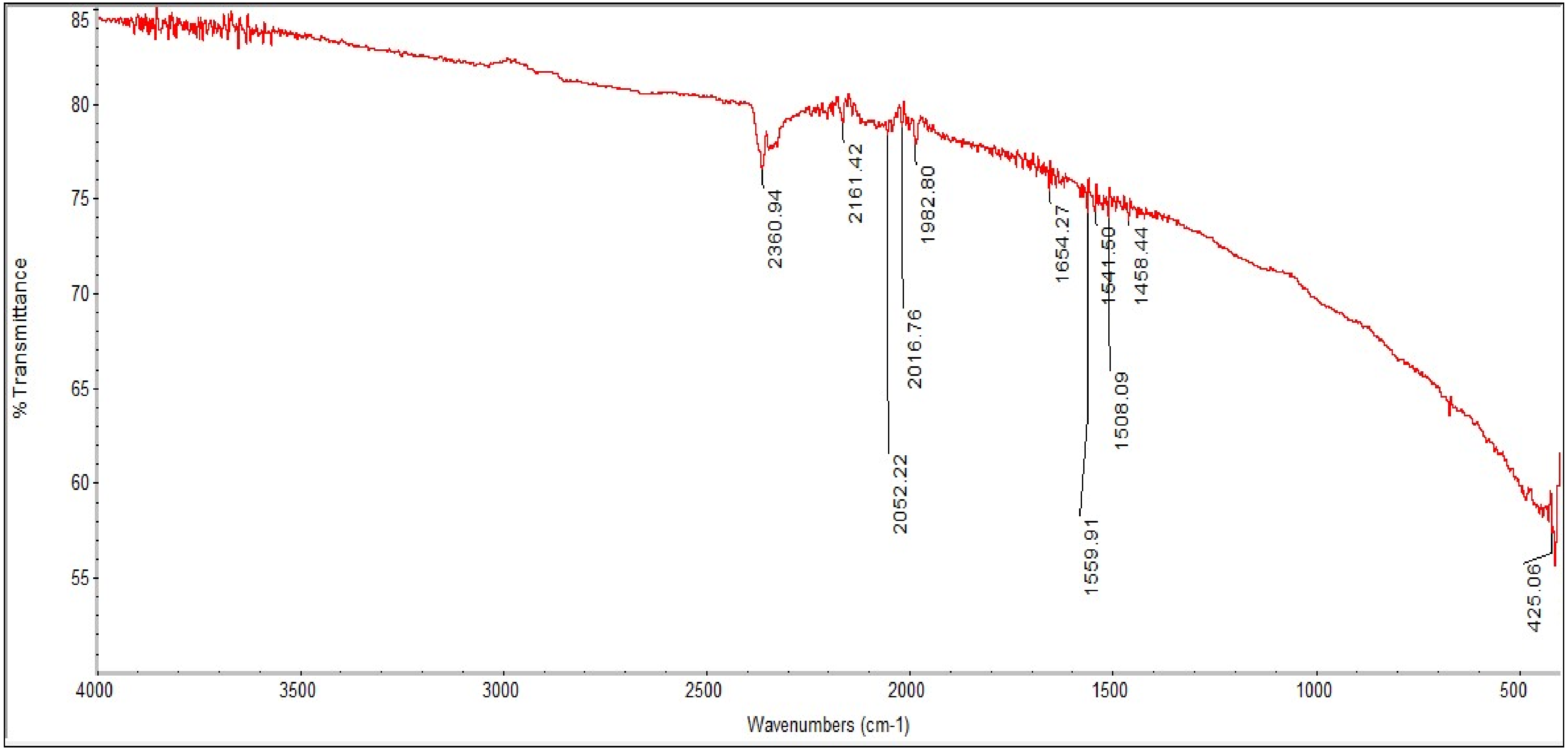

Figure B-8: FTIR Spectrum of Spent 20 wt% g-C_3N_4/PAC Composite.

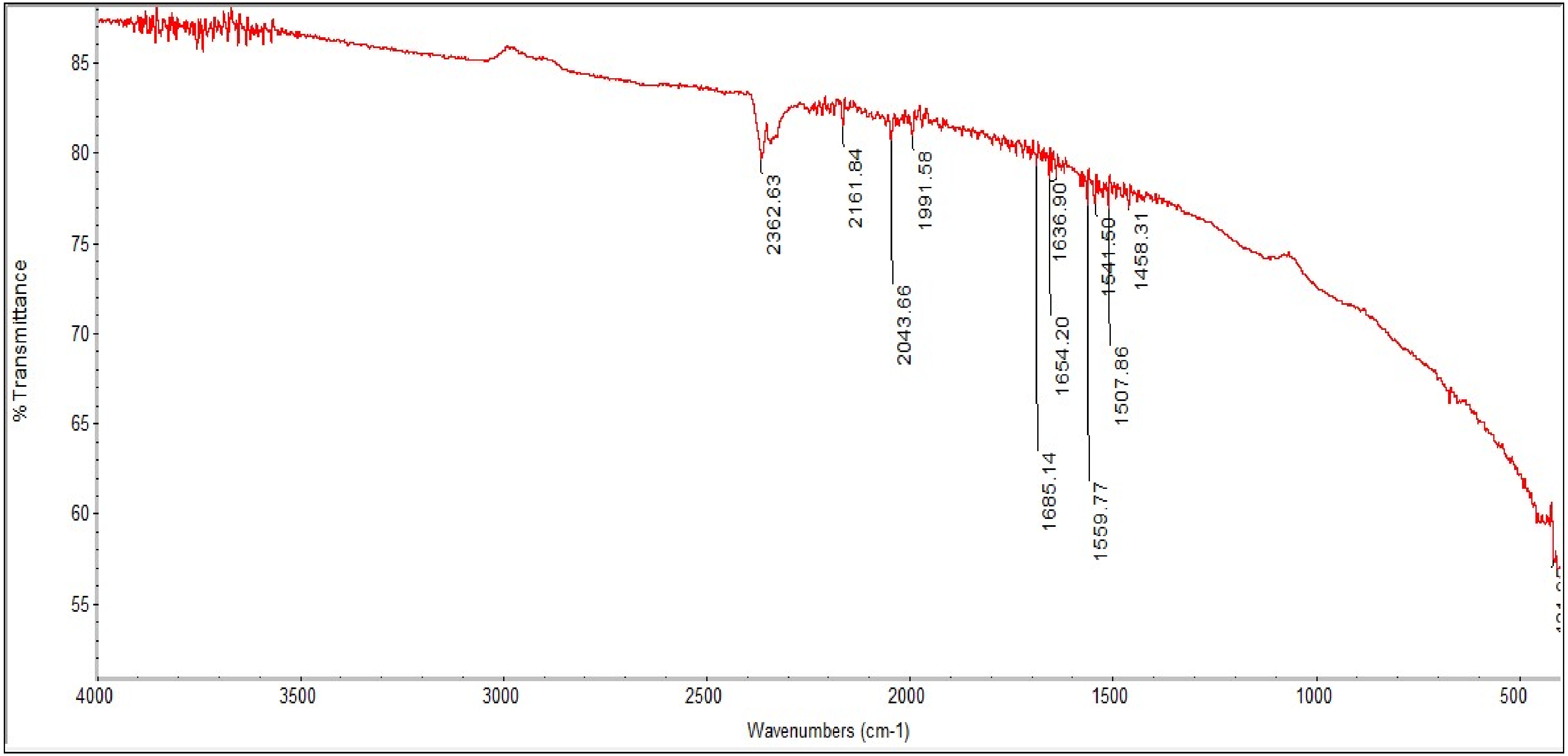

Figure B-9: FTIR Spectrum of Spent 40 wt% g-C_3N_4/PAC Composite.

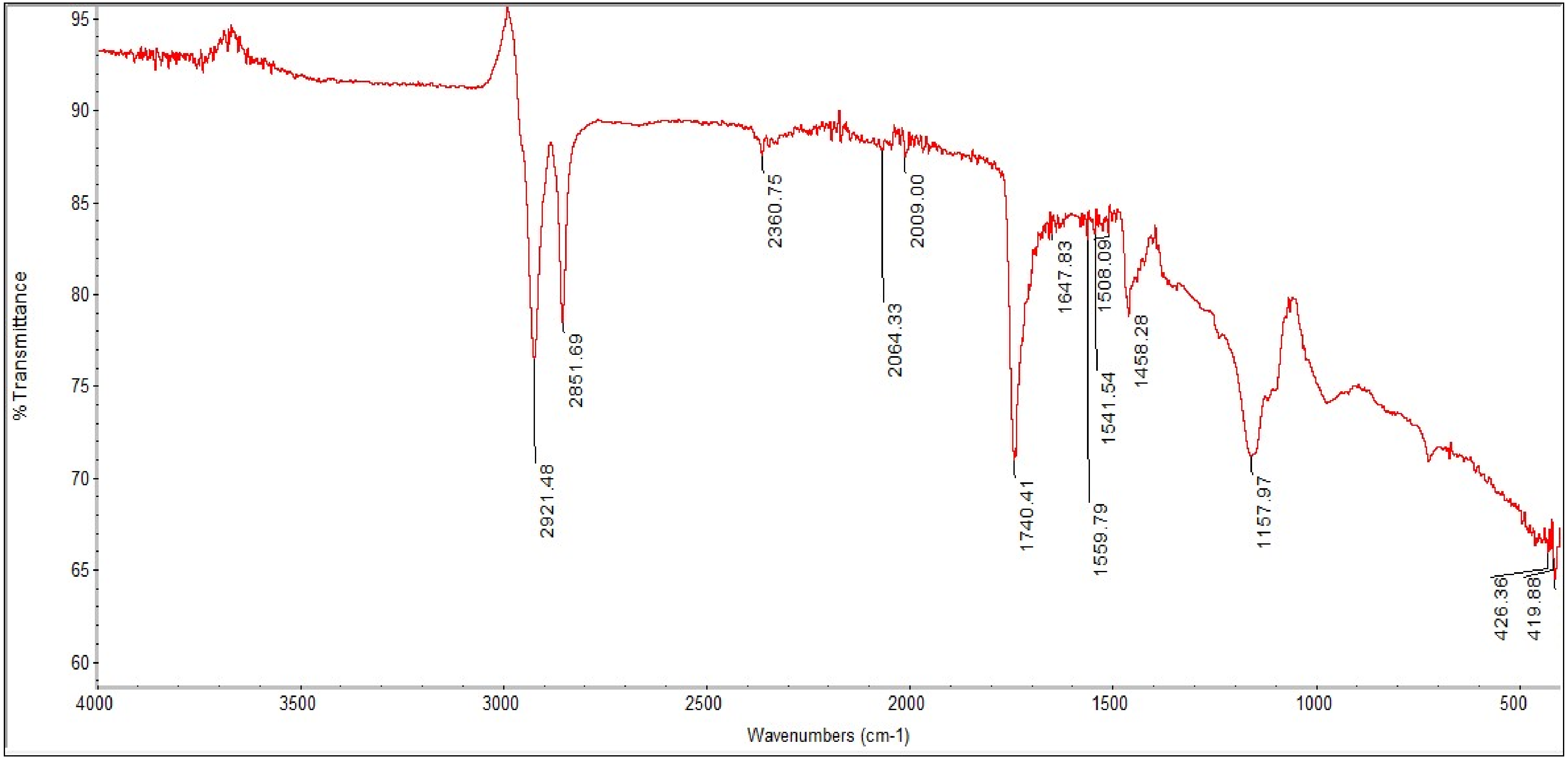

Figure B-10: FTIR Spectrum of Spent 60 wt% g-C_3N_4/PAC Composite.

APPENDIX C: EDX Report

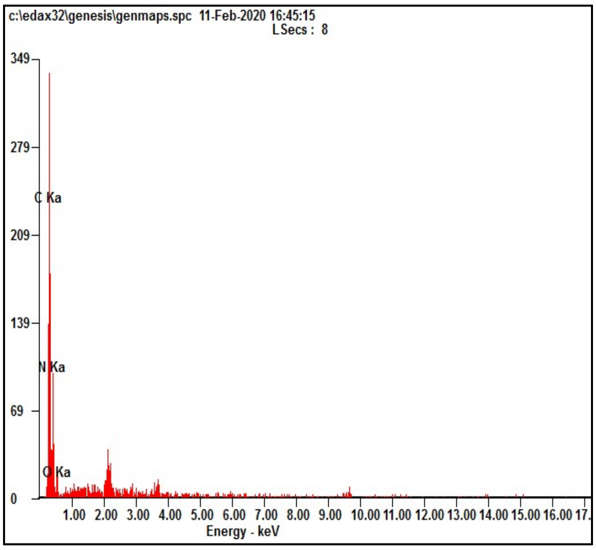

Element	***Wt%***	***At%***
CK	58.08	62.21
NK	35.60	32.70
OK	06.32	05.09
Matrix	Correction	MThin

Figure C-1: EDX Analysis of Pure g-C_3N_4.

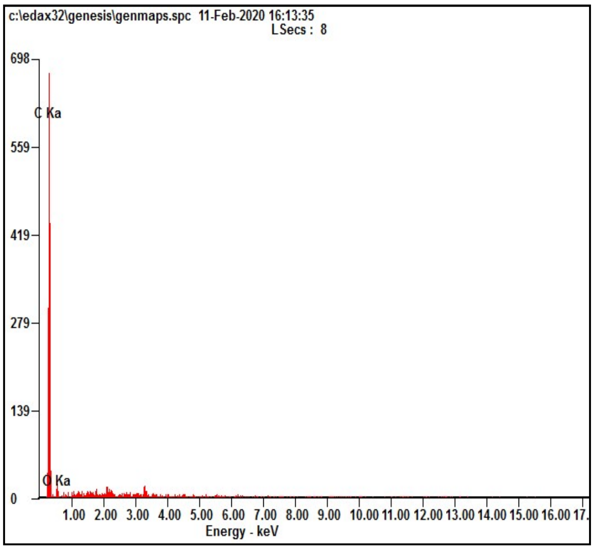

Element	***Wt%***	***At%***
CK	95.68	96.72
OK	04.32	03.28
Matrix	Correction	MThin

Figure C-2: EDX Analysis of AC.

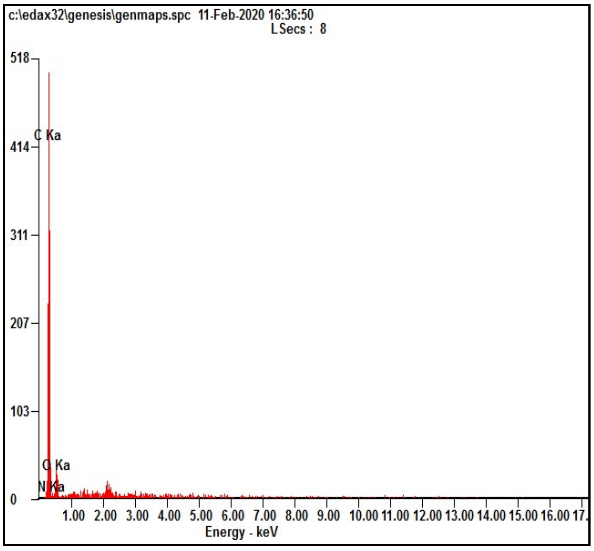

Element	***Wt%***	***At%***
CK	88.72	91.17
NK	01.15	01.01
OK	10.13	07.81
Matrix	Correction	MThin

Figure C-3: EDX Analysis of 20 wt% g-C_3N_4/PAC Composite.

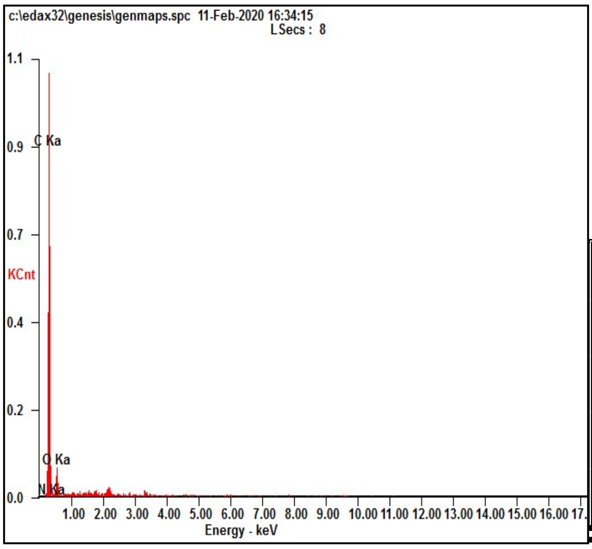

Element	***Wt%***	***At%***
CK	87.87	90.47
NK	01.41	01.25
OK	10.72	08.29
Matrix	Correction	MThin

Figure C-4: EDX Analysis of 40 wt% g-C_3N_4/PAC Composite.

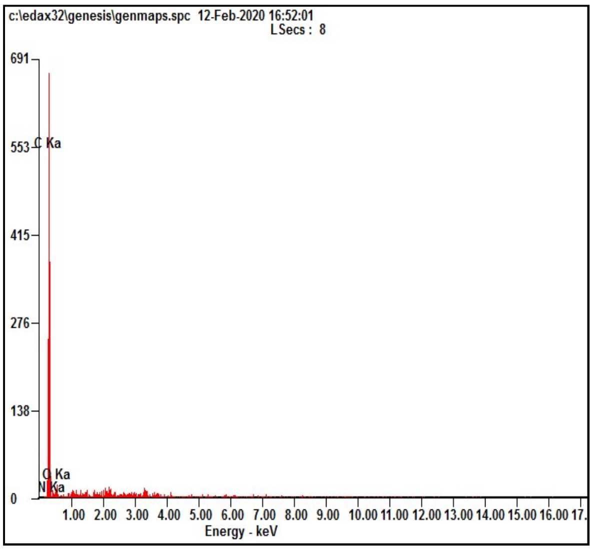

Element	***Wt%***	***At%***
CK	93.84	95.02
NK	02.70	02.35
OK	03.46	02.63
Matrix	Correction	MThin

Figure C-5: EDX Analysis of 60 wt% g-C_3N_4/PAC Composite.